AD_____

Award Number DAMD17-96-1-6023

TITLE: Fluorescence Lifetime Imaging For Breast Cancer Detection
       and Diagnosis

PRINCIPAL INVESTIGATOR: Eva N. Sevick Muraca, Ph.D.

CONTRACTING ORGANIZATION: Purdue Research Foundation
                          West Lafayette, Indiana 47907

REPORT DATE: July 1999

TYPE OF REPORT: Final

PREPARED FOR: U.S. Army Medical Research and Materiel Command
              Fort Detrick, Maryland 21702-5012

DISTRIBUTION STATEMENT: Approved for public release; distribution
                        unlimited.

The views, opinions and/or findings contained in this report are
those of the author(s) and should not be construed as an official
Department of the Army position, policy or decision unless so
designated by other documentation.

DTIC QUALITY INSPECTED 4

20001019 119

REPORT DOCUMENTATION PAGE		Form Approved OMB No. 0704-0188

Public reporting burden for this collection of information is estimated to average 1 hour per response, including the time for reviewing instructions, searching existing data sources, gathering and maintaining the data needed, and completing and reviewing the collection of information. Send comments regarding this burden estimate or any other aspect of this collection of information, including suggestions for reducing this burden, to Washington Headquarters Services, Directorate for Information Operations and Reports, 1215 Jefferson Davis Highway, Suite 1204, Arlington, VA 22202-4302, and to the Office of Management and Budget, Paperwork Reduction Project (0704-0188), Washington, DC 20503.

1. AGENCY USE ONLY *(Leave blank)*	2. REPORT DATE July 1999	3. REPORT TYPE AND DATES COVERED Final (1 Jul 96 - 30 June 99)	
4. TITLE AND SUBTITLE Fluorescence Lifetime Imaging for Breast Cancer Detection and Diagnosis			**5. FUNDING NUMBERS** DAMD17-96-1-6023
6. AUTHOR(S) Eva N. Sevick Muraca, Ph.D.			
7. PERFORMING ORGANIZATION NAME(S) AND ADDRESS(ES) Purdue Research Foundation West Lafayette, Indiana 47907			**8. PERFORMING ORGANIZATION REPORT NUMBER**
9. SPONSORING / MONITORING AGENCY NAME(S) AND ADDRESS(ES) U.S. Army Material Research and Material Command Fort Detrick, Maryland 21702-5012			**10. SPONSORING / MONITORING AGENCY REPORT NUMBER**
11. SUPPLEMENTARY NOTES			
12a. DISTRIBUTION / AVAILABILITY STATEMENT Approved for Public Release; Distribution Unlimited			**12b. DISTRIBUTION CODE**

The development of non-invasive, biomedical optical imaging from frequency-domain photon migration (FDPM) measurements of near-infrared (NIR) light propagation depends upon (i) the measurements of optical signals on the boundary of tissues and (ii) the numerical techniques enabling the reconstruction of interior optical properties from such measurements. From the mapping of interior optical properties, it is envisioned that diseased tissues can be identified and diagnosed based upon the differences in absorption and scattering properties. Briefly, FDPM consists of launching intensity-modulated light at the air-tissue interface and detecting the phase-delay and amplitude attenuation at another point distant from the incident point source. In the Purdue Photon Migration Laboratory (PPML), we have developed rapid multi-pixel methods for acquiring large data sets of phase-delay and amplitude attenuation across a tissue surface for use in an inversion algorithm in order to perform image reconstruction. In addition, since we have found that the endogenous contrast offered by absorption and scattering may be insufficient for biomedical imaging, we have invented a method for inducing contrast using fluorescent contrast agents. Algorithm development for biomedical fluorescence lifetime imaging was conducted under USAMRMC support. Using fluorescent agents, we have shown that the inverse problem may be better posed and that biodiagnostic information can be obtained from assessing the fluorescent decay kinetics within the tissue.

14. SUBJECT TERMS			15. NUMBER OF PAGES
Biomedical optical imaging, Fluorescent contrast agents, Frequency-domain photon migration			91
			16. PRICE CODE

17. SECURITY CLASSIFICATION OF REPORT Unclassified	18. SECURITY CLASSIFICATION OF THIS PAGE Unclassified	19. SECURITY CLASSIFICATION OF ABSTRACT Unclassified	20. LIMITATION OF ABSTRACT Unlimited

FOREWORD

Opinions, interpretations, conclusions and recommendations are those of the author and are not necessarily endorsed by the U.S. Army.

_____ Where copyrighted material is quoted, permission has been obtained to use such material.

_____ Where material from documents designated for limited distribution is quoted, permission has been obtained to use the material.

_____ Citations of commercial organizations and trade names in this report do not constitute an official Department of Army endorsement or approval of the products or services of these organizations.

_____ In conducting research using animals, the investigator(s) adhered to the "Guide for the Care and Use of Laboratory Animals," prepared by the Committee on Care and use of Laboratory Animals of the Institute of Laboratory Resources, national Research Council (NIH Publication No. 86-23, Revised 1985).

_____ For the protection of human subjects, the investigator(s) adhered to policies of applicable Federal Law 45 CFR 46.

_____ In conducting research utilizing recombinant DNA technology, the investigator(s) adhered to current guidelines promulgated by the National Institutes of Health.

_____ In the conduct of research utilizing recombinant DNA, the investigator(s) adhered to the NIH Guidelines for Research Involving Recombinant DNA Molecules.

_____ In the conduct of research involving hazardous organisms, the investigator(s) adhered to the CDC-NIH Guide for Biosafety in Microbiological and Biomedical Laboratories.

Eva M Sarot   7/29/99
PI - Signature   Date

TABLE OF CONTENTS

Paithankar, D.Y. Chen, A.U., Pogue, B.W., Patterson, M.S., and E.M. Sevick-Muraca, "Imaging of fluorescent yield and lifetime from multiply scattered light re-emitted from tissues and other random media," Appl. Optics, 36: 2260-2272, 1997.

Sevick-Muraca, E.M., Heintzelman, D.L., Lee, J., Troy, T.L., and D.Y. Paithankar, "The role of higher order scattering in solutions to the forward and inverse optical imaging problems in random media," Appl. Optics, 36: 9058-9067, 1997.

Lee, J. and E.M. Sevick-Muraca, "Fluorescence-enhanced absorption and lifetime imaging," Biomedical Imaging: Reporters, Dyes, annd Instrumentation," D.J. Bornhop, C.H. Contag, and E.M. Sevick (eds)., Proc. Soc. Photo-Opt. Instrum. Eng., 3600:246-254, 1999.

Eppstein, M.J., Dougherty, D.E., Troy, T.L., and E.M. Sevick-Muraca, "Biomedical Optical tomography using dynamic parameterization and Bayesian conditioning on photon migration measurements," Appl. Optics, 38: 2138-2150, 1999 *(cover of issue)*. With NSF and NIH support resulting from USMRMC supported successes.

Roy, R. and E.M. Sevick-Muraca, "Truncated Newton's optimization scheme for absorption and fluorescence optical tomography: Part I Theory and Formulation," Optics Express, 4: 353-371, 1999.

Roy, R. and E.M. Sevick-Muraca, "Truncated Newton's optimization scheme for absorption and fluorescence optical tomography: Part II Reconstructions from synthetic measurements" Optics Express, 4: 372-382, 1999.

INTRODUCTION

The development of non-invasive, biomedical optical imaging from frequency-domain photon migration (FDPM) measurements of near-infrared (NIR) light propagation depends upon (i) the measurements of optical signals on the boundary of tissues and (ii) the numerical techniques enabling the reconstruction of interior optical properties from such measurements. From the mapping of interior optical properties, it is envisioned that diseased tissues can be identified and diagnosed based upon the differences in absorption and scattering properties. Under prior NIH support, we have developed instrumentation for rapid acquisition of FDPM data. Briefly, FDPM consists of launching intensity-modulated light at the air-tissue interface and detecting the phase-delay and amplitude attenuation at another point distant from the incident point source. In the Purdue Photon Migration Laboratory (PPML), we have developed rapid multi-pixel methods for acquiring large data sets of phase-delay and amplitude attenuation across a tissue surface for use in an inversion algorithm in order to perform image reconstruction. In addition, since we have found that the endogenous contrast offered by absorption and scattering may be insufficient for biomedical imaging, we have invented a method for inducing contrast using fluorescent contrast agents. By using fluorescent contrast agents, we have shown that the inverse problem may be better posed and that biodiagnostic information can be obtained from assessing the fluorescent decay kinetics within the tissue.

BODY

The inverse imaging problem is crucial to the development of biomedical optical imaging, the subject of USAMRMC support. To date we have developed an algorithm using efficient numerical techniques for the image reconstruction for imaging tissues. Our algorithm has been developed in two stages, consisting of the forward and inverse imaging problems. The forward problem involves solution of the optical diffusion equations for excitation and emission light using a uniform (and coarse) finite element and finite difference meshed. We have refined our forward solver to include graded meshing and three-dimensional geometries. To date we have formulated the inverse problem in a number of ways:

(1) As an optimization problem in which parameter updates of absorption and lifetime are separately determined through a linear Newton-Raphson approach (see attached manuscripts by Paithankar, *et al.*, 1998 and Troy and Sevick, 1999);

(2) As a non-linear optimization problem in which parameter updates of absorption and lifetime are separately determined through a Truncated Newton algorithm using efficient finite element formulation (see manuscripts by Roy and Sevick-Muraca, 1999a, 1999b);

(3) As a linear optimization problem in which parameter updates of absorption and lifetime are determined simultaneously and in which the forward problem is posed as Born scattering (see Lee and Sevick-Muraca, 1999);

(4) As a non-linear optimization using Bayesian conditioning and parameter zonation structure to obtain parameter estimates in three dimensional space (in conjunction with Univ. of Vermont and NSF, see Eppstein, et al., 1999); and

(5) As a simply bound constrained optimization for two and three-dimensional reconstruction (see manuscript by Roy and Sevick, 1999).

Manuscripts are included in the Appendix.

The accuracy and performance of these algorithms have been investigated using 2-D "synthetic" data. We currently are extending our formulation to 3-D experimental data using the multi-pixel imaging system developed under NIH support.

The USARMC research is significant to the biomedical engineering field in that it seeks to develop the mathematical basis to answer questions of optical imaging performance in realistic 3-D geometries. Since prior work on the inverse imaging problem has been largely confined to two dimensional systems, the opportunities to employ its solution using actual three-dimensional data has been limited. The development of a three-dimensional reconstruction algorithm in the PPML is significant since the experimental acquisition of FDPM data of model systems is readily available to test the algorithm in upcoming research.

KEY RESEARCH ACCOMPLISHMENTS:

(1)   Developed a forward predictor code for 2-D and 3-D frequency-domain photon migration based upon finite difference and finite element numerical techniques.

(2)   Developed an inversion code for 2-D and 3-D reconstruction of fluorescent optical properties using frequency-domain photon migration measurements.

(3)   Tested these algorithms successfully on synthetically generated data sets and have explored their success in the presence of experimental measurement noise.

The research has enabled us to move forward under different support to build a fast optical imaging device and to image mammary disease in vivo within a canine model. Under NSF and NIH support, we have tested these algorithms using experimental data. While this was a wildly successful exploratory grant, our proposal for clinical translational research for sentinel lymph node staging was not accepted for further funding at the white paper stage.

REPORTABLE OUTCOMES

Peer-reviewed papers:

Paithankar, D.Y. Chen, A.U., Pogue, B.W., Patterson, M.S., and E.M. Sevick-Muraca, "Imaging of fluorescent yield and lifetime from multiply scattered light re-emitted from tissues and other random media," Appl. Optics, 36: 2260-2272, 1997.

Sevick-Muraca, E.M., Lopez, G., Troy, T.L., Reynolds, J.S., and C.L. Hutchinson, "Fluorescence and absorption contrast mechanisms for biomedical optical imaging using frequency-domain techniques," Photochemistry and Photobiology, 66: 55-64, 1997.

Sevick-Muraca, E.M., Heintzelman, D.L., Lee, J., Troy, T.L., and D.Y. Paithankar, "The role of higher order scattering in solutions to the forward and inverse optical imaging problems in random media," Appl. Optics, 36: 9058-9067, 1997.

Eppstein, M.J., Dougherty, D.E., Troy, T.L., and E.M. Sevick-Muraca, "Biomedical Optical tomography using dynamic parameterization and Bayesian conditioning on photon migration measurements," Appl. Optics, 38: 2138-2150, 1999 *(cover of issue)*.

Roy, R. and E.M. Sevick-Muraca, "Truncated Newton's optimization scheme for absorption and fluorescence optical tomography: Part I Theory and Formulation," Optics Express, 4: 353-371, 1999.

Roy, R. and E.M. Sevick-Muraca, "Truncated Newton's optimization scheme for absorption and fluorescence optical tomography: Part II Reconstructions from synthetic measurements" Optics Express, 4: 372-382, 1999.

Mayer, R.H., Reynolds, J.S., and E.M. Sevick-Muraca, "Measurement of fluorescence lifetime in scattering media using frequency-domain photon migration," Appl. Optics, accepted.

Roy, R. and E.M. Sevick-Muraca, "An active constrained Truncated Newton method for optical tomography" submitted to Journal of the Optical Society of America A, submitted June 1999.

Proceedings papers

Sevick-Muraca, Eva M., Jiang, H., Hutchinson, C.L., and D.Y. Paithankar, "Fluorescence lifetime spectroscopy and imaging in scattering media with frequency-domain techniques," in <u>Applications of Optical Engineering to the Study of Cellular Pathology</u>, Ed. Kohen, 1997.

Sevick-Muraca, E.M., Reynolds, J.S., Troy, T.L., Lopez, G., and D.Y. Paithankar, "Fluorescence lifetime spectroscopic imaging with measurements of photon migration," in <u>Advances in Optical Biopsy and Optical Mammography</u>, Ed. R.R. Alfano, New York Academy of Sciences, Vol. 838, pp. 46-57, 1998.

Troy, T.L., and E.M. Sevick-Muraca, "Fluorescence lifetime imaging and spectroscopy in random media," in <u>Applied Fluorescence in Chemistry, Biology, and Medicine</u>, Rettig, Strehmel, Schrader, and Seifert eds., Springer Verlag, Berlin pp.3-39, 1999.

Sevick-Muraca, E.M. and D.Y. Paithankar, "Imaging of fluorescent yield and lifetime from multiply scaterred light re-emitted from random media," In <u>Advances in Fluorescence Sensing Technology in Chemical Diagnostics III</u>, eds. J.R. Lakowicz and R.B. Thompson, Proc. Soc. Photo-Opt. Instrum. Eng., 2980: 303-318, 1997.

Lopez, G., Troy, T.L., Reynolds, J.S., Hutchinson, C.L., and E.M. Sevick-Muraca, "Detection of fluorescent and light absorbing optical hetereogeneities in tissue-mimicking phantoms using frequency-domain techniques," In <u>Advances in Fluorescence Sensing Technology in Chemical Diagnostics III</u>, eds. J.R. Lakowicz and R.B. Thompson (eds), Proc. Soc. Photo-Opt. Instrum. Eng., 2980: 519-529, 1997.

Chen, A. and E.M. Sevick-Muraca, "On the use of phosphorescent and fluorescent dyes for lifetime-based imaging within tissues," Proc. Soc. Photo-Opt. Instrum. Eng., in <u>Optical Tomography and Spectroscopy of Tissue: Theory, Instrumentation, Model, and Human Studies II</u>, B. Chance and R.R. Alfano (eds), 2979: 129-138, 1997.

Troy, T.L., Reynolds, J.S., and E.M. Sevick-Muraca, "Reconstruction of fluorescence lifetime and quantum efficiency using frequency-domain photon migration measurements," ," <u>OSA Trends in Optics and Photonics, Vol. 22, Biomedical Optical Spectroscopy and Diagnostics/Therapeutic Laser Applications, ,</u>" E.M. Sevick-Muraca, J.A. Izatt, and M.N. Ediger, eds., Optical Society of America, Washington, DC., 76-83, 1998.

Eppstein, M.J., Dougherty, D.E., Troy, T.L., and E.M. Sevick-Muraca, "Stochastic optical tomography using beta-distributed parameters to model absorption, lifetime, and quantum efficiency," <u>Biomedical Imaging: Reporters, Dyes, annd Instrumentation</u>," D.J. Bornhop, C.H. Contag, and E.M. Sevick (eds)., Proc. Soc. Photo-Opt. Instrum. Eng., 3600: 230-236, 1999.

Eppstein, M.J., Dougherty, D.E., Hawrysz, D.J., and E.M. Sevick-Muraca, "Three-dimensional optical tomography," <u>Optical Tomography and Spectroscopy of Tissue III</u>, B. Chance, R.R. Alfano, and B.J. Tromberg (eds)., Proc. Soc. Photo-Opt. Instrum. Eng., 3597: 000-000, 1999.

Lee, J. and E.M. Sevick-Muraca, "Fluorescence-enhanced absorption and lifetime imaging," <u>Biomedical Imaging: Reporters, Dyes, annd Instrumentation</u>," D.J. Bornhop, C.H. Contag, and E.M. Sevick (eds)., Proc. Soc. Photo-Opt. Instrum. Eng., 3600:246-254, 1999.

Roy, R. and E.M. Sevick-Muraca, "Imaging of absorption coefficients and lifetime in scattering media with heterogeneous fluorophore distribution using simply bound constrained minimization," *in* <u>Biomedical Imaging: Reporters, Dyes, annd Instrumentation</u>," D.J. Bornhop, C.H. Contag, and E.M. Sevick (eds)., Proc. Soc. Photo-Opt. Instrum. Eng., 3600: 237-245, 1999.

Patents:

"Fluorescence imaging system and measurement," E.M. Sevick-Muraca and D.Y. Paithankar,U.S. patent #5,865,754, issued 2/2/99.

"Fluorescence and absorption contrast mechanisms for biomedical optical imaging using frequency-domain techniques," E.M. Sevick-Muraca, T.L. Troy, C.L. Hutchinson, and G. Lopez, Purdue patent application no. P-97001.00US, patent application number: 60/039,318.

Degrees Obtained:

Tamara L. Troy, "Biomedical optical imaging with frequency-domain photon migration measurements: experiments and numerical image reconstructions," Ph.D. Chemical Engineering, Purdue University, December 1997.

Alvin Chen, "Effects of fluorescence and phosphorescence lifetime on frequency-domain optical contrast for biomedical optical imaging" M.S. Chemical Engineering, Purdue University, December 1997.

Alan Thompson, "Multi-pixel assessment of fluorophore uptake and lifetime in the detection of heterogeneous tissue volumes," M.S. Chemical Engineering, Purdue University, December 1998.

Funding applied for based on the work supported by this award:

National Institutes of Health (F32 CA73107) "Frequency-domain lifetime imaging and spectroscopy," National Institutes of Health, March 1, 1997 - February 28, 1998 ($36.3K). *(sponsor for Dr. Huabei Jiang).*

National Science Foundation, (DBI-9870779) "Recursive Bayesian Optical Tomography for Biomedical Imaging," (P.I.: Dougherty and Eppstein), subcontract to Purdue University, September 1998 - September 2000, ($58K).

National Institutes of Health (CA R01-67176), "Fluorescence lifetime spectroscopy and imaging," September 1999-August 2003, ($1,460K) *percentile score: 2.7%.*

National Science Foundation, "Three dimensional biomedcial optical imaging: formulation and solution," January 1, 2000 – December 31, 2002, pending.

Employment opportunities and training supported by this award:

Huabei Jiang, (Ph.D. EE., Ph.D. Biomed. Eng., Dartmouth), 1996 - 1997. *winner of National Institutes of Health Individual Service Award in the Photon Migration Laboratory, 1996-1997. Dr. Jiang is currently a tenure track Assistant Professor of Physics and Astronomy at Clemson University.*

Tamara L. Troy, (Ph.D. ChE; Purdue) Research Associate, 1997 – 1998.

Ranadhir Roy, (Ph.D. Mathematics; Univ. Hertfordshire) Research Associate, 1998 - present

CONCLUSIONS:

The overall goal of this research is to apply recent advances in frequency-domain photon migration (FDPM) technologies within an in vivo imaging study to develop the basis for non-invasive, image-guided therapy and diagnosis. Over the past nine years, research to (i) engineer rapid measurement devices for clinical measurements; (ii) develop inversion algorithms for accurate image reconstruction and spectroscopy; and (iii) discover the use of fluorescent contrasting agents for enhancing image quality have resulted in an imaging system now ready for testing *in vivo.* In our laboratory, we have obtained *in vivo* FDPM images of phase and modulation of the detected intensity modulated wave at 100 MHz that was created from re-emitted ICG fluorescence from deep "leaky" vessels feeding reactive and involve inguinal canine lymph nodes. The results suggest the potential use of the near-infrared technology for diagnosis of lymph node involvement in melanoma and breast cancer patients. Other opportunities for FDPM spectroscopic imaging also exist. By employing intensity modulated light at the peak oxy- and deoxy- hemoglobin and isosbestic absorption wavelengths (820, 754, and 800 nm) the opportunities to provide low resolution oxygenation mapping during the course of radiation and chemo-therapies in order to guide staging is afforded. In addition, sentinel lymph node mapping could also be improved with NIR techniques, if our veterinary studies are translatable to the clinic. In conjunction with proposed Indiana University/Purdue University Institutional (IUPUI) studies of

sentinel lymph node mapping, which involves the injection of blue dye or a radionucleotide for regional lymph node status, we also propose to adapt fluorescence FDPM for non-invasive evaluation lymph node status at IUPUI. We propose to use approved contrast agents (ICG) in patients with metastatic breast disease for assessing the lymph node status and multi-focality of the disease. Clearly the junxtaposition of FDPM imaging, sentinel mapping, and axillary lymph node biopsies will provide comparative ROC's for assessing the potential impact of optical imaging in the management of breast cancer and melanoma. Finally, the development of fluorescent contrast agents with lifetimes sensitive to local biochemical environments (pO2, pH, etc.) may also provide function/structural imaging capabilities that can aid in the efficacious choice of therapy and its staging.

REFERENCES: See accompanying manuscripts in Appendix

APPENDICES:

Paithankar, D.Y. Chen, A.U., Pogue, B.W., Patterson, M.S., and E.M. Sevick-Muraca, "Imaging of fluorescent yield and lifetime from multiply scattered light re-emitted from tissues and other random media," Appl. Optics, 36: 2260-2272, 1997.

Sevick-Muraca, E.M., Heintzelman, D.L., Lee, J., Troy, T.L., and D.Y. Paithankar, "The role of higher order scattering in solutions to the forward and inverse optical imaging problems in random media," Appl. Optics, 36: 9058-9067, 1997.

Lee, J. and E.M. Sevick-Muraca, "Fluorescence-enhanced absorption and lifetime imaging," Biomedical Imaging: Reporters, Dyes, annd Instrumentation," D.J. Bornhop, C.H. Contag, and E.M. Sevick (eds)., Proc. Soc. Photo-Opt. Instrum. Eng., 3600:246-254, 1999.

Eppstein, M.J., Dougherty, D.E., Troy, T.L., and E.M. Sevick-Muraca, "Biomedical Optical tomography using dynamic parameterization and Bayesian conditioning on photon migration measurements," Appl. Optics, 38: 2138-2150, 1999 (cover of issue). With NSF and NIH support resulting from USMRMC supported successes.

Roy, R. and E.M. Sevick-Muraca, "Truncated Newton's optimization scheme for absorption and fluorescence optical tomography: Part I Theory and Formulation," Optics Express, 4: 353-371, 1999.

Roy, R. and E.M. Sevick-Muraca, "Truncated Newton's optimization scheme for absorption and fluorescence optical tomography: Part II Reconstructions from synthetic measurements" Optics Express, 4: 372-382, 1999.

LIST OF PERSONNEL RECEIVING SALARY SUPPORT:

Dr. Dilip Y. Paithankar
Dr. Huabei Jiang
Dr. Ranadhir Roy

Imaging of fluorescent yield and lifetime from multiply scattered light reemitted from random media

D. Y. Paithankar, A. U. Chen, B. W. Pogue, M. S. Patterson, and E. M. Sevick-Muraca

The feasibility of employing fluorescent contrast agents to perform optical imaging in tissues and other scattering media has been examined through computational studies. Fluorescence lifetime and yield can give crucial information about local metabolite concentrations or environmental conditions within tissues. This information can be employed toward disease detection, diagnosis, and treatment if non-invasively quantitated from reemitted optical signals. However, the problem of inverse image reconstruction of fluorescence yield and lifetime is complicated because of the highly scattering nature of the tissue. Here a light propagation model employing the diffusion equation is used to account for the scattering of both the excitation and fluorescent light. Simulated measurements of frequency-domain parameters of fluorescent modulated ac amplitude and phase lag are used as inputs to an inverse image-reconstruction algorithm, which employs the diffusion model to predict frequency-domain measurements resulting from a modulated input at the phantom periphery. In the inverse image-reconstruction algorithm, a Newton–Raphson technique combined with a Marquardt algorithm is employed to converge on the fluorescent properties within the medium. The successful reconstruction of both the fluorescence yield and lifetime in the case of a heterogeneous fluorophore distribution within a scattering medium has been demonstrated without *a priori* information or without the necessity of obtaining absence images. © 1997 Optical Society of America

Key words: Fluorescence imaging, biomedical optics, image reconstruction, fluorescence lifetime, fluorescence yield.

1. Introduction

Over the past decade, several investigators have explored the use of exogenous fluorescent dyes as contrast agents to differentiate diseased and normal tissues from noninvasive or endoscopic optical measurements. The diagnosis of burn depth following Indocyanine Green dye administration[1] and the demarcation of neoplastic tissues following intravascular porphyrin dye administration[2-4] are possible because of their leakage from vessels corrupted by insult or disease. The concomitant increase in fluorescence from the dye can be detected at the tissue surface and permits the detection of disease. With the development of dyes and photodynamic agents that excite and reemit in the near-infrared red wavelength regime, the noninvasive detection of diseased tissues located deep within tissues may also be possible because red excitation and reemission light can travel significant distances to and from the tissue–air interface.[5] However, a long-standing problem has been the low uptake or leakage into neoplastic tissues, providing insufficient contrast for the detection of diseased tissues. Although targeted delivery may improve uptake ratios and contrast imparted by these otherwise therapeutic agents, these approaches have been elusive even in conventional imaging modalities such as magnetic resonance imaging (MRI) and x-ray computed tomography. Investigators have sought to alleviate the optical contrast uptake problem by employing dyes that fluoresce differently in diseased tissues than in normal tissues. The use of agents whose reemission characteristics vary with tissue pH[6,7] and pO_2[8] may not only provide detection of diseased tissues by the nature of differing fluores-

cent properties but may also contain diagnostic information. The difficulty lies in measuring the multiply scattered reemitted light and reconstructing an image that differentiates tissues on the basis of fluorescent properties, such as fluorescent yield and lifetime.

In this study we investigate the combination of photon migration imaging techniques with fluorescence spectroscopy to examine the feasibility of fluorescence lifetime imaging (FLI).[9] FLI may be considered an optical analog to MRI. Whereas MRI depends on monitoring the spatial variation in the relaxation time of spin–spin states to provide high-resolution imaging in tissues, FLI depends on monitoring the spatial variation in the fluorophore lifetime and yield. The complication with FLI in tissues arises from the excitation and fluorescent photon times of flight, which are similar in magnitude to the fluorescence lifetime. Herein we combine inverse imaging techniques (as developed previously by Pogue et al.[10]) and fluorescence lifetime spectroscopy to demonstrate the feasibility of FLI by using computational studies. We separately introduce the concepts of photon migration imaging and fluorescence spectroscopy in Section 2 and then describe the combination of techniques in our computational approach to FLI. Our reconstructed images show the ability to image both fluorescence lifetime and fluorescence yield independent of any *a priori* information and point to the development of fluorescent dyes whose reemission characteristics are environmentally sensitive and provide contrast for the optical detection of diseased tissues.

2. Background: Photon Migration Imaging and Fluorescence Spectroscopy

The ability to reconstruct an internal map of absorption optical properties from continuous wave[11] and absorption and scattering properties from frequency-domain[10,12,13] measurements has been successfully demonstrated by using multiply scattered light from random media. Continuous wave measurements consist of noninvasively monitoring the attenuation of light as a function of position around the periphery of a heterogeneous tissue phantom model in response to a constant intensity source, whereas frequency-domain measurements consist of monitoring the phase and amplitude modulation of multiply scattered light at various peripheral positions in response to an incident modulated light source. Both approaches employ a perturbation analysis whereby the absorption and scattering properties at each pixel position within the tissue phantom are individually and independently adjusted until the measurements of reemitted light at the periphery of the tissue phantom match those predicted by a model for diffusive light propagation in random media. These studies show the potential for image reconstruction of hidden tissue heterogeneities when the contrast caused by either absorption or scattering coefficients is as low as 2:1.[13] However, Troy et al.[14] conducted *in vitro* measurements of normal and diseased breast tissues and showed that the endogenous optical contrast between 120 normal and diseased breast tissues is not significantly different for consistent detection with optical techniques. These measurements were conducted *ex vivo* and consequently may underestimate the contrast available *in vivo* caused by increased tumor vasculature and absorption caused by hemoglobin. Nonetheless, these results suggest the need for optical contrast agents.

Previously, we experimentally demonstrated the increased sensitivity for detecting heterogeneities on the basis of fluorescence as opposed to absorption when time-dependent measurements are employed.[15] Indeed, the augmentation of optical contrast that is due to the lifetime of a fluorophore or phosphorescent probe has been recognized by Wu et al.[16] in tissue phantom studies. The localization of a fluorescing body has been performed by various researchers.[17–19] Upon activation into a higher electronic state by the absorption of light, an activated fluorophore may undergo nonradiative decay or radiative decay; the latter results in the reemission of a fluorescent photon. The yield is defined by the fractional number of fluorescent photons reemitted for each excitation photon absorbed or the fraction of decay events that results in the emission of a fluorescent photon. The lifetime is defined as the mean survival time of the activated fluorophore or the mean time between the absorption of an excitation photon and the reemission of a fluorescent photon. Because the stability of the activated fluorophore depends on its environment, both yield and lifetime are also dependent on the (bio) chemical environment in which the fluorophore resides. Consequently, the lifetime can provide contrast based on the differences in biochemical environments of normal and diseased tissues, similar to the contrast provided by relaxation times in nuclear magnetic resonance imaging.

The use of lifetime for contrast in optical imaging in tissues is not new. In studies demonstrating the noninvasive differentiation of hematoporphyrin-laden tumors from normal tissue, Cubeddu et al.[20] employed the comparatively long lifetime (>15 ns) of reemitted fluorescence caused by increased porphyrin uptake in tumors over the lifetime of endogenous compounds (>7 ns) in normal tissues in order to provide discrimination of the two tissue types. These microscopy studies involved unscattered light that provided correct reemission kinetics of measured fluorescence. In this computational study, we employ contrast that is due to increased uptake as well as lifetime in order to differentiate diseased tissue by using multiply scattered light reemitted from tissues that involve deeply seated tissue volumes. The reemission kinetics of phosphorescent probes do not permit an interrogation deep into tissue with time-domain approaches.[21] Our preliminary frequency-domain computations (unpublished) suggest that the simultaneous determination of location and lifetime is difficult when long-lived phosphorescent probes are used. In Section 3 we underscore the magnitude of the problem by describing the forward imaging prob-

lem (i.e., prediction of the frequency-domain measurements given the location, optical properties, and fluorescent properties of the random media) as well as our adapted approach for solving the inverse problem (i.e., prediction of the location, optical properties, and fluorescent properties of the medium from measurements of frequency-domain light propagation).

3. Forward Problem and the Solution Methodology

The spatial and temporal transport of light in tissues or multiply scattering media can be accurately described by the diffusion approximation to the radiative transport equation. A coupled frequency-domain diffusion equation can be used to predict the excitation and emission fluence rates, $\Phi_x(r, \omega)$ and $\Phi_m(r, \omega)$, at any location r within a tissue phantom by Eqs. (1) and (2), respectively.[22-24]

$$\nabla \cdot [D_x(r)\nabla\Phi_x(r, \omega)] - [\mu_{a_x}(r) + i\omega/c_n]$$
$$\times \Phi_x(r, \omega) + S_x(r, \omega) = 0, \quad (1)$$

$$\nabla \cdot [D_m(r)\nabla\Phi_m(r, \omega)] - [\mu_{a_m}(r) + i\omega/c_n]$$
$$\times \Phi_m(r, \omega) + S_m(r, \omega) = 0. \quad (2)$$

The source term for excitation light $S_x(r, \omega)$ is due to the sinusoidally modulated light at frequency $\omega = 2\pi f$, where f is usually in the megahertz range. The first term in both equations represents the diffusive or random-walk transport of light where $D_{x,m}$ is the optical diffusion coefficient, i.e.,

$$D_{x,m} = [3(\mu_{a_{x,m}} + \mu_{s_{x,m}}')]^{-1}, \quad (3)$$

and μ_a and μ_s' are the absorption and isotropic scattering coefficients, respectively. The optical properties are dependent on the wavelength of light and thus are different for the excitation (subscript x) and fluorescent (subscript m) light. The total absorption coefficient at the excitation wavelength, μ_{a_x}, is due to contributions from nonfluorescing chromophores as well as from fluorescent dye. The total absorption coefficient is given by the sum of absorption coefficients that are due to nonfluorescing chromophores, $\mu_{a_{x_-}}$, and fluorophores, $\mu_{a_{x-m}}$. We assume that the absorption experienced at the fluorescent wavelength primarily is due to nonfluorescing chromophores. The velocity of light in tissue is $c_n = c/n$, where n is the average index of refraction. The source term for the fluorescent light is dependent on the excitation light fluence, $\Phi_x(r, \omega)$, and is given by

$$S_m(r, \omega) = \eta\mu_{a_{x-m}}(r)\Phi_x(r, \omega)\frac{1 - i\omega\tau(r)}{1 + \omega^2\tau(r)^2}. \quad (4)$$

This term arises from the Fourier transform of the single-exponential fluorescence decay term $(1/\tau)\exp(-t/\tau)$ in the time domain following an incident pulse of excitation light where τ is the fluorophore lifetime. Here η is the quantum yield and the absorption coefficient, $\mu_{a_{x-m}}$, is the product of the extinction coefficient, $\log_e 10$, and the concentration of the fluorophore in the ground state. For the purposes of

this study, the combined product, $\eta\mu_{a_{x-m}}$, is termed the fluorescent yield and is proportional to the generated fluorescence fluence. Note that multiexponential time decay can also be handled with this procedure by a simple extension.

In the source term for fluorescent light given in Eq. (4), $\mu_{a_{x-m}}$ changes as the relative fractions of the fluorophore in the ground and excited states change. The saturation effects would have to be handled by taking into account the relative amounts of fluorophore in the ground and excited states. We neglect the saturation effects and assume single-exponential decay kinetics in this initial study.

Furthermore, μ_{a_x} in Eq. (1) is the sum of $\mu_{a_{x-}}$ and $\mu_{a_{x-m}}$. In what follows, images of lifetime, τ, and images of $\eta\mu_{a_{x-m}}$ are obtained. There is a difficulty in the estimation of μ_{a_x} that is given by $\mu_{a_x} = \mu_{a_{x-}} + \mu_{a_{x-m}}$, because the explicit values of $\mu_{a_{x-m}}$ are not known (the values of the product of η and $\mu_{a_{x-m}}$ are known). Because the major contribution to μ_{a_x} is from $\mu_{a_{x-}}$ and not $\mu_{a_{x-m}}$, we have used an approximate expression for μ_{a_x}, $\mu_{a_x} = \mu_{a_{x-}} + \eta\mu_{a_{x-m}}$ and have chosen η as 1 only for the purposes of calculation of μ_{a_x}. Our approach can be extended to permit imaging of η, $\mu_{a_{x-m}}$, $\mu_{a_{x-}}$, and τ from measurements conducted at both excitation and fluorescent wavelengths. Although reconstruction from fluorescent measurements provides $\eta\mu_{a_{x-m}}$, excitation measurements can provide $\mu_{a_{x-}}$ (in the absence of a fluorophore) and $\mu_{a_{x-m}} + \mu_{a_{x-}}$ (in the presence of a fluorophore). From these images, maps of η and $\mu_{a_{x-m}}$ can be obtained in principle.

Both Eqs. (1) and (2) are linear complex elliptic equations that can be solved as boundary value problems for complex quantities $\Phi_x(r, \omega)$ and $\Phi_m(r, \omega)$. We employ the method of finite differences in which we place a grid over the space domain and obtain an approximation to the solution at each grid point, j. One of the fastest methods to solve these linear elliptic boundary value problems is the multigrid solution (see the review by Fulton et al.[25]). In the procedure for the multigrid solution, an initial solution is obtained quickly for coarse grids that is then further refined for a better solution for finer grids. This is an involved procedure in which we have elected to use MUDPACK routines.[26] MUDPACK routines are flexible and allow placement of sources either at the surface or inside the phantom. For the equations to be solved, it is assumed that $\Phi_{m,x}(r, \omega) = 0$ on the tissue surface, which is known as the zero-fluence boundary condition. This is implemented by assigning the absorption coefficient for both excitation and fluorescent light at all the grid points in the square grid lying outside the circular tissue phantom to a large value. The source was simulated by setting the value of Φ_x to an arbitrary complex number at a grid point on the surface where the source is located. The solution of Eqs. (1) and (2) yields a complex number for Φ_m at each grid point, j. The detected signal at the surface is proportional to the normal component of the gradi-
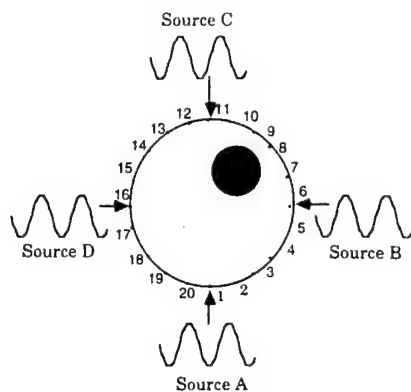
Fig. 1. Schematic of the circular simulated tissue phantom interrogated by four sources, one source at a time. Twenty detectors are located on the periphery with uniform separation. A circular object that mimics a hidden diseased tissue volume, located within the tissue phantom, is also shown.
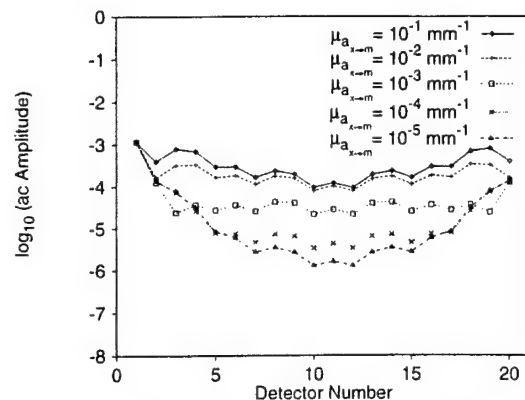

Fig. 2. Log plot of fluorescent light ac amplitude at 150 MHz at various detectors for a heterogeneous tissue phantom with a 30-mm-diameter object located at the center of the phantom for various object $\eta\mu_{a_{x\rightarrow m}}$ values. Absorption coefficient $\eta\mu_{a_{x\rightarrow m}}$ is 1×10^{-5} mm^{-1} for the background; lifetimes τ for both the object and the background are 1 ns.

ent. In this study, for evaluation of the signal at detector i located on the surface, we used the value of Φ_m at an internal grid point closest to the detector. This is reasonable in our initial approach because the normal component of the gradient is proportional to Φ_m just inside the surface.[10] The phase lag, θ_M, and the log of the ac amplitude, M_m, at the detectors were calculated with respect to the phase and the ac amplitude of the source. The computational time required to solve for the fluorescent fluence on a SunSparc 10 for a 17×17 grid is 0.04 s, and that for a 33×33 grid is 0.165 s. Different grid sizes were used in the testing phase of the solution of the equations, and the solutions were in agreement within the numerical error caused by the finite grid size.

Before attempting to solve the inverse problem for the simulated phantom illustrated in Fig. 1, we must first understand the effects of changing the fluorescent optical properties of the tissue on θ_m and M_m measured at a detector or series of detectors located on its surface. Solutions to Eqs. (1) and (2) were obtained in two dimensions for a 65×65 grid covering a 100-mm-diameter circular tissue phantom with a circular embedded heterogeneity of 30 mm diameter and located at the center of the tissue phantom. The simulated measurements of fluorescent phase shift and ac amplitude are reported for 20, equally spaced, circumferentially located detectors. The modulation frequency, f, was set equal to 150 MHz. The optical properties of the heterogeneity and the background are shown in Table 1.

A. Effect of $\eta\mu_{a_{x\rightarrow m}}$ on θ_m and M_m

In order to evaluate the influence of $\eta\mu_{a_{x\rightarrow m}}$, θ_m and M_m were computed at each detector as the value of $\eta\mu_{a_{x\rightarrow m}}$ in the heterogeneity increased from 10^{-4} mm^{-1} to 10^{-1} mm^{-1} and as $\eta\mu_{a_{x\rightarrow m}}$ in the background was maintained constant. The modulation frequency was chosen as 150 MHz. The lifetime, τ, was set equal to 1 ns for both the object and the background causing contrast resulting solely from differences in $\eta\mu_{a_{x\rightarrow m}}$. The plots of θ_m and M_m are shown in Figs. 2 and 3, respectively, for one source located at position A. The curves for M_m are not smooth because the circular surface is approximated by joining discrete grid points closest to the circumference by straight lines. Furthermore, the curves for both θ_m and M_m are symmetric for detectors 2 and 20, 3 and 19, 4 and 18, and so on because these detector pairs are symmetric with respect to the source. The detectors near the source are unaffected by the presence of an object because the photon sampling volume does not include the region occupied by the heterogeneity. At the other detector locations, the fluorescent ac amplitude increases as $\eta\mu_{a_{x\rightarrow m}}$ of the heterogeneity increases. As $\eta\mu_{a_{x\rightarrow m}}$ of the heterogeneity increases to high values, the ac amplitude approaches an upper limit that is due to high absorption coefficient μ_{a_x}, which is a sum of $\mu_{a_{x\rightarrow m}}$ and $\mu_{a_{x\rightarrow}}$. This is similar to the inner-filter effect in which the high absorption in the heterogeneity shields the interior of the heterogeneity from excitation photons.[27] Figure 3 illustrates changes in fluorescent phase shift, θ_m, as a

Table 1. Optical Properties and Experimental Parameters for the Forward Problem

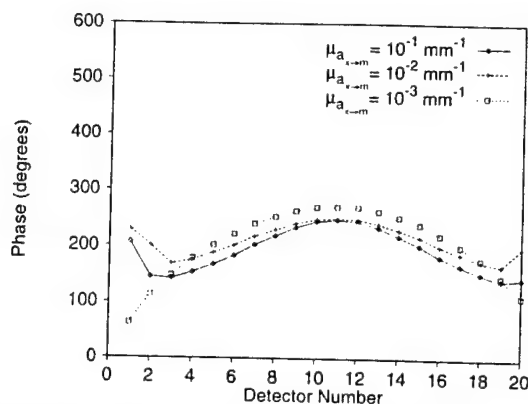| μ_{a_x} (mm^{-1})	μ_{a_m} (mm^{-1})	μ_{s_x}' or μ_{s_m}' (mm^{-1})	$\mu_{a_{x\rightarrow}}$ (mm^{-1})	$\eta\mu_{a_{x\rightarrow m}}$ Background (mm^{-1})	τ Background (ns)	Frequency (MHz)
$\mu_{a_{x\rightarrow}} + \mu_{a_{x\rightarrow m}}$	0.0	1.0	0.0	1.0×10^{-5}	1.0	150.0

Fig. 3. Plot of fluorescent light phase shift at 150 MHz at various detectors for a heterogeneous tissue phantom with a 30-mm-diameter object located at the center of the phantom for various object $\eta\mu_{a_{x \to m}}$ values. Absorption coefficients and lifetimes are the same as in Fig. 2.
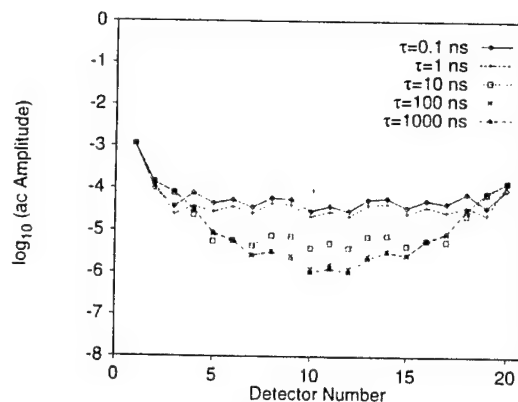

Fig. 4. Log plot of fluorescent light ac amplitude at 150 MHz at various detectors for a heterogeneous tissue phantom with a 30-mm-diameter object located at the center of the phantom for various object τ values. Background lifetime τ is 1 ns and absorption coefficients $\eta\mu_{a_{x \to m}}$ are 1×10^{-5} mm^{-1} for the background and 1×10^{-3} mm^{-1} for the object.

function of the fluorescent yield that is due to the fluorophore, $\eta\mu_{a_{x \to m}}$. As $\eta\mu_{a_{x \to m}}$ is increased from 10^{-3} mm^{-1} to 10^{-1} mm^{-1} (when the background value is 10^{-5} mm^{-1}), little change in phase shift occurs. Because the phase shift of reemitted fluorescence in dilute, nonscattering solutions is a function of lifetime and is not dependent on concentration [$\theta \sim \tan^{-1}(\omega\tau)$], one might expect similar trends in scattering media. Indeed, as shown in Fig. 3, phase-shift changes caused by fluorophore concentration differences are small. Consequently, the changes in phase shift with increasing $\eta\mu_{a_{x \to m}}$ of the heterogeneity can be attributed to the alteration in photon migration as a result of the presence of heterogeneities with a high absorption of excitation light.[28] The presence of heterogeneities with high absorption reduces the effective path length of photon migration and reduces the phase shift, though this reduction is small in magnitude. In summary, M_m is directly and strongly dependent on changes in $\eta\mu_{a_{x \to m}}$ of a simulated tissue heterogeneity, whereas θ_m is indirectly and weakly dependent on $\eta\mu_{a_{x \to m}}$ because of changes in photon migration.

B. Effect of τ on M_m and θ_m

In order to evaluate the influence of τ, M_m and θ_m were calculated at each detector as the values of τ in the heterogeneity varied from 10^{-1} ns to 10^3 ns and the value of τ in the background was held at 1 ns. The modulation frequency was at 150 MHz. Background $\eta\mu_{a_{x \to m}}$ was set to 10^{-5} mm^{-1}, and $\eta\mu_{a_{x \to m}}$ for the object was set to 10^{-3} mm^{-1}. As shown in Fig. 4, the detected ac amplitude increases as τ decreases. Because M_m of reemitted fluorescence in a dilute, nonscattering solution is a function of lifetime (and also fluorophore concentration), one would expect that in the presence of scatter, similar trends would be observed. Figure 5 illustrates the values of the fluorescent phase shift at each detector as the lifetime of the heterogeneity is changed from 0.1 ns to 1000 ns. At the given modulation frequency (150

MHz in this calculation), θ_m first increases, reaches a maximum, and then subsequently decreases as τ is increased from 0.1 ns to 1000 ns. There is a complex interplay of the signal coming from the object for which we are changing the lifetime and the signal from the background that leads to the behavior described. In summary, both M_m and θ_m at each detector are directly and strongly influenced by the value of lifetime in the heterogeneity.

Detailed analytical expressions for fluorescence amplitude and phase shift for infinite and semi-infinite media with spherical heterogeneities have been provided by Li et al.[29] Our numerical computational methods provide a simulation of finite media and arbitrary shaped hidden objects. Our numerical results agree with the general predictions provided by Li et al.[29]

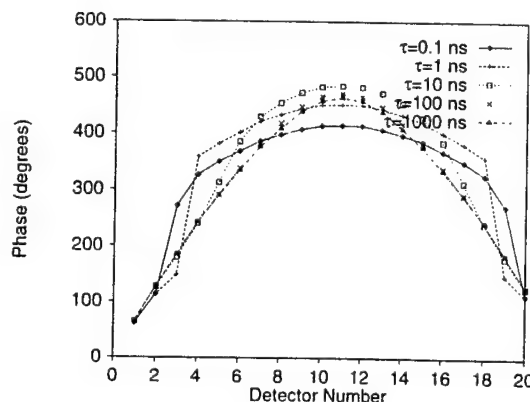The solution of the forward problem was used as inputs to the solution of the inverse problem de-

Fig. 5. Plot of fluorescent light phase shift at 150 MHz at various detectors for a heterogeneous tissue phantom with a 30-mm-diameter object located at the center of the phantom for various object τ values. Background lifetime τ is 1 ns and absorption coefficients $\eta\mu_{a_{x \to m}}$ are 1×10^{-5} mm^{-1} for the background and 1×10^{-3} mm^{-1} for the object.

Table 2. Optical Properties Used to Generate the Simulated Experimental Data as Inputs to the Inverse Image-Reconstruction Algorithm

Case	μ_{a_x} (mm^{-1})	μ_{a_m} (mm^{-1})	μ_{s_x}' or μ_{s_m}' (mm^{-1})	τ Background (ns)	$\eta\mu_{a_{x\rightarrow m}}$ Background (mm^{-1})	σ_M Gaussian Noise in Log of ac Amplitude	σ_θ Gaussian Noise in Phase (deg)
5.A	0.0	0.0	1.0	10.0	1.0×10^{-5}	0.01	0.1
5.B	1.0×10^{-3}	1.0×10^{-3}	1.0	10.0	1.0×10^{-5}	0.01	0.1
5.C	0.0	0.0	1.0	10.0	1.0×10^{-5}	0.01	1.0
5.D	1.0×10^{-3}	1.0×10^{-3}	1.0	10.0	1.0×10^{-5}	0.01	0.1

scribed in Section 4. Forward solutions in two dimensions were computed for the three cases outlined in Tables 2 and 3 for the source and detector geometry in a 100-mm-diameter simulated tissue phantom (Fig. 1). Values of θ_m and M_m were computed at each detector in response to four sources of excitation light located at the periphery modulated at a single frequency of 150 MHz. Consequently, the forward solution predicted 80 values of θ_m and M_m, each at detector i ($i = 1, 20$) in response to source k ($k = 1, 4$). Gaussian noise with a standard deviation of 0.1° (or a liberal 1°) in θ_m and 1% in M_m was superimposed on the solution of the forward problem. These obtained data sets are used as the simulated experiments as input to the reconstruction algorithm described below.

4. Inverse Problem and the Solution Methodology

We begin our inverse calculations from a uniform starting guess of a fluorescence yield, $(\eta\mu_{a_{x\rightarrow m}})_j$, and lifetime, $(\tau)_j$, at all the grid points within the tissue phantom. With the initial guess of an optical property map, one can evaluate the complex fluence at the various detector locations. There are two approaches that one can follow: one involves minimizing the difference between the complex number that is calculated from the ac magnitude and phase, and the other uses the ac magnitude and phase information itself. The two approaches are equivalent, and we have chosen the second approach of using the ac magnitude and phase. With the starting guess of optical properties, we compute a prediction of phase shift $(\theta_m)_i$ and log of ac amplitude $(M_m)_i$ at each detector i. Values of $(\eta\mu_{a_{x\rightarrow m}})_j$ and $(\tau)_j$ are iteratively adjusted at each grid point to minimize the error between the predicted and sim-

ulated experimental values of $(\theta_m)_i$ and $(M_m)_i$ resulting from each source, k, $k = 1, 4$. The choice of appropriate functions to be minimized for our reconstructions is now discussed. Section 3 describes at length how changes in the fluorescent yield and lifetime affect the measured values of ac magnitude and phase. Changes in fluorescent yield, $\eta\mu_{a_{x\rightarrow m}}$, have a direct and strong influence on the ac magnitude and only an indirect and weak influence on the phase. Hence we have chosen to adjust iteratively the values of $(\eta\mu_{a_{x\rightarrow m}})_j$ in order to minimize the merit function, χ_μ^2, that depends on the ac magnitude measurements:

$$\chi_\mu^2 = \frac{1}{4}\sum_{k=1}^{4}\frac{1}{20}\sum_{i=1}^{20}\left(\frac{M_{m_{\text{obs},i}} - M_{m,i}}{\sigma_M}\right)^2, \quad (5)$$

where σ_M is the typical standard deviation of noise in M_m, taken to be 0.01.

The value of $M_{m_{\text{obs},i}}$ is the simulated experimental value computed in Section 3 with added Gaussian noise. The goal of the algorithm is to minimize χ_μ^2 by appropriate updates of $(\eta\mu_{a_{x\rightarrow m}})_j$. After an iteration of the $(\eta\mu_{a_{x\rightarrow m}})_j$ update, values of $(\tau)_j$ were adjusted in the next iteration in order to minimize a second merit function, χ_τ^2:

$$\chi_\tau^2 = \frac{1}{4}\sum_{k=1}^{4}\frac{1}{20}\sum_{i=1}^{20}\left[\left(\frac{M_{m_{\text{obs},i}} - M_{m,i}}{\sigma_M}\right)^2 + \left(\frac{\theta_{m_{\text{obs},i}} - \theta_{m,i}}{\sigma_\theta}\right)^2\right], \quad (6)$$

where σ_θ is the typical standard deviation of noise in θ, taken to be 1°. The values of $\theta_{m_{\text{obs},i}}$ are the simulated experimental values computed in Section 3 with added Gaussian noise. The above merit

Table 3. Location and Area of the Simulated Heterogeneities: Comparison of Expected and Reconstructed Values

Case	Object 1		Object 2	
	Area (mm^2)	Location (x, y) (mm)	Area (mm^2)	Location (x, y) (mm)
5.A	706.0 (expected) 742 (obtained)	(60, 60) (expected) (61, 59) (obtained)	not applicable	not applicable
5.B	706.0 (expected) 683 (obtained)	(60, 60) (expected) (59, 58) (obtained)	not applicable	not applicable
5.C	314.1 (expected) 381 (obtained)	(32.3, 67.7) (expected) (34, 68) (obtained)	314.1 (expected) 342 (obtained)	(67.7, 32.3) (expected) (65, 35) (obtained)
5.D	706.0 (expected) 693 (obtained)	(60, 60) (expected) (61, 57) (obtained)	not applicable	not applicable

function is chosen because changes in lifetime τ have a direct and strong influence on both the ac magnitude and phase. Hence we have chosen to adjust iteratively the values of $(\tau)_j$ in order to minimize the merit function that consists of both ac magnitude and phase measurements. The goal of this part of the algorithm is to minimize χ_τ^2 by appropriate choice of $(\tau)_j$ as described below. In Eq. (5), the choice of the value of σ_M does not affect the minimization–update process. We have chosen the typical noise values for M and θ, σ_M and σ_θ, respectively, to be factors for converting to dimensionless numbers. In fact σ_M and σ_θ are simply scale factors that assess confidence in measurement. For example, when σ_θ is smaller for a given σ_M, the θ residuals are weighted more heavily in the inversion as compared with the M residuals. Thus, factor σ is necessary to normalize the individual sum of residuals of M and θ so the two can be added in Eq. (6).

To update values of $(\eta\mu_{a_{x \to m}})_j$ and $(\tau)_j$, one needs the Jacobian matrices that describe the sensitivity of the detector response at position i to changes in $(\tau)_j$ and $(\eta\mu_{a_{x \to m}})_j$ at each grid point, j. The elements of the three Jacobian matrices employed, $\bar{\bar{J}}(M, \eta\mu_{a_{x \to m}})$, $\bar{\bar{J}}(M, \tau)$, and $\bar{\bar{J}}(\theta, \tau)$, are given by $j_{i,j} = [\partial M_i / \partial(\eta\mu_{a_{x \to m}})_j], j_{i,j} = (\partial M_i / \partial \tau_j)$, and $j_{i,j} = (\partial\theta_i / \partial\tau_j)$, respectively. One calculates these elements by solving the forward problem four times for each grid point, j to obtain $M_{m,i}$ and $\theta_{m,i}$ calculated with $(\tau)_j$ and $(\tau + \Delta\tau)_j$ and with $(\eta\mu_{a_{x \to m}})_j$ and $(\eta\mu_{a_{x \to m}} + \Delta\eta\mu_{a_{x \to m}})_j$. From the least-squares minimization, one can show that the update in $\eta\mu_{a_{x \to m}}$ and τ can be calculated by using an algorithm (Newton's method) similar to that suggested by Yorkey et al.[30] for the reconstruction of images obtained by electrical impedance tomography.

Equations (7) and (8) provide updates

$$\left[\frac{\bar{\bar{J}}(M, \eta\mu_{a_{x \to m}})^T \bar{\bar{J}}(M, \eta\mu_{a_{x \to m}})}{\sigma_M^2} + \lambda_1 \bar{\bar{I}}\right][\overline{\Delta\eta\mu_{a_{x \to m}}}]$$

$$= \left[\frac{\bar{\bar{J}}(M, \eta\mu_{a_{x \to m}})^T}{\sigma_M^2}(\bar{M}_{m_{obs}} - \bar{M}_m)\right], \quad (7)$$

$$\left[\frac{\bar{\bar{J}}(M, \tau)^T \bar{\bar{J}}(M, \tau)}{\sigma_M^2} + \frac{\bar{\bar{J}}(\theta, \tau)^T \bar{\bar{J}}(\theta, \tau)}{\sigma_\theta^2} + \lambda_2 \bar{\bar{I}}\right][\overline{\Delta\tau}]$$

$$= \left[\frac{\bar{\bar{J}}(M, \tau)^T}{\sigma_M^2}(\bar{M}_{m_{obs}} - \bar{M}_m) + \frac{\bar{\bar{J}}(\theta, \tau)^T}{\sigma_\theta^2}(\bar{\theta}_{m_{obs}} - \bar{\theta}_m)\right],$$

$$(8)$$

$[\overline{\Delta\eta\mu_{a_{x \to m}}}]$, and $[\overline{\Delta\tau}]$ to the yield $[\overline{\eta\mu_{a_{x \to m}}}]$ and lifetime $[\bar{\tau}]$ vectors at each iteration. The update of $[\overline{\eta\mu_{a_{x \to m}}}]$ is based on the ac amplitude data, whereas that of $[\bar{\tau}]$ is based on both the ac amplitude and phase data. This follows from the discussion in the previous section on the forward problem. $\bar{M}_{m_{obs}}$ and $\bar{M}_m$ are the experimentally simulated and calculated vectors consisting of the log of the ac amplitude at each of the i detectors, respectively. Because of the ill-
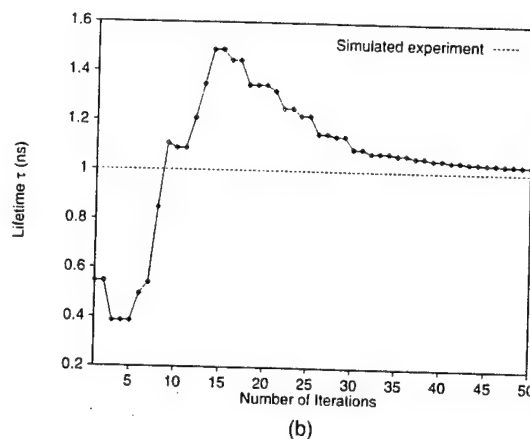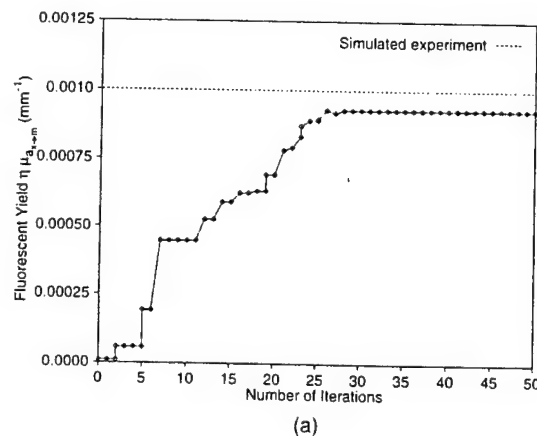

Fig. 6. Graphs depicting the convergence of (a) $\eta\mu_{a_{x \to m}}$, (b) τ versus the number of iterations during the image reconstruction for the case described in Subsection 5.A. Convergence is seen to be achieved within 20 iterations for (a) and 50 iterations for (b).

conditioned nature of the Jacobian matrices, terms $\lambda_1 \bar{\bar{I}}$ or $\lambda_2 \bar{\bar{I}}$ are added ($\bar{\bar{I}}$ is an identity matrix) to make the matrices more diagonally dominant and the solution of the algebraic equations more robust. Parameters λ_1 or λ_2 are adjusted by means of a Marquardt–Levenberg type of algorithm.[31] Lower triangular–upper triangular decomposition and backsubstitution are employed to solve the simultaneous linear algebraic equations given in Eqs. (7) and (8).[31] At each iteration, the merit functions, the Jacobian matrices, and the updates in the fluorescent yield and lifetime are evaluated and the iterations are continued until the convergence criterion is met. Convergence is achieved when any of the following three quantities, i.e., χ^2, change in χ^2 in successive iterations, and relative change in χ^2 in successive iterations, is lower than a predetermined value of 1.0×10^{-5}.

5. Results and Discussion

The performance of FLI by using the inversion algorithms described above is depicted in Figs. 6–9 for the case studies listed in Tables 2 and 3. Simulated experiment 5.A was designed to reconstruct $(\tau)_j$ and $(\eta\mu_{a_{x \to m}})_j$ with no absorption that is due to nonfluo-
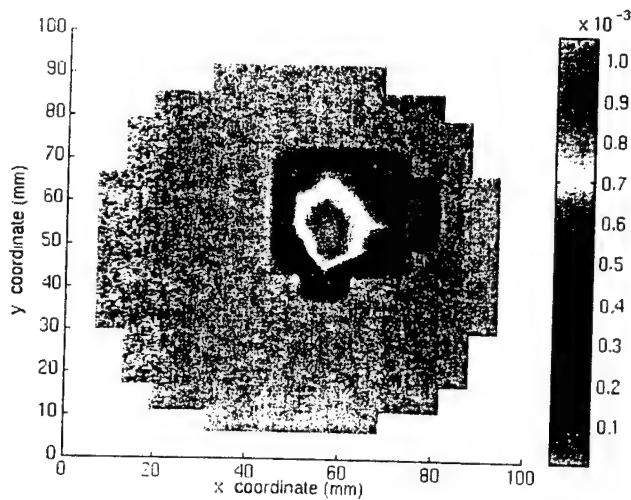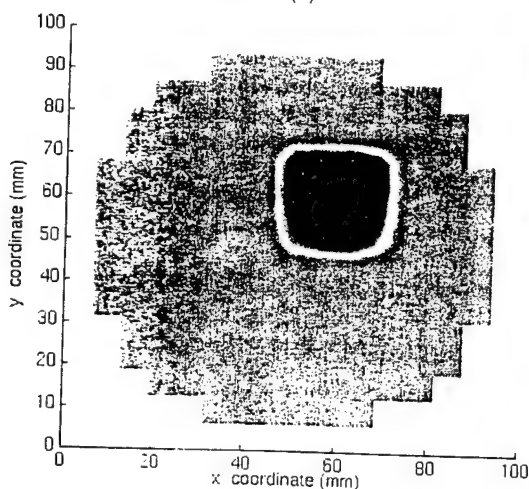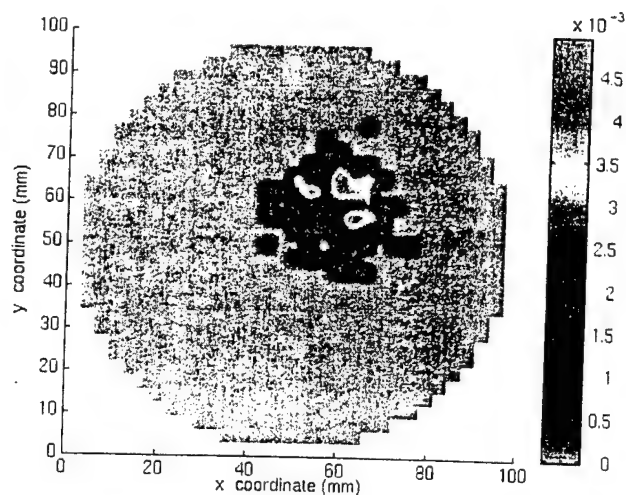
Fig. 7. Reconstructed spatial map of fluorescence (a) yield, $\eta\mu_{a_{x\rightarrow m}}$, (b) lifetime, τ, on a two-dimensional, 17×17 grid for the case described in Subsection 5.A. μ_{a_x} at the excitation wavelength not accounting for fluorophore absorption is zero; μ_{a_m} at the emission wavelength is also zero. The average values of $\eta\mu_{a_{x\rightarrow m}}$ and τ within the object were 1×10^{-3} mm^{-1} and 1 ns, respectively (expected) and 0.93×10^{-3} mm^{-1} and 1.03, respectively (reconstructed). Spurious unphysically high values of $\eta\mu_{a_{x\rightarrow m}}$ and τ have been replaced by the average background fluorescence yield and lifetime, respectively, obtained from the inversion.

Fig. 8. Reconstructed spatial map of fluorescence (a) yield, $\eta\mu_{a_{x\rightarrow m}}$, (b) lifetime, τ, on a two-dimensional, 17×17 grid for the case described in Subsection 5.B. μ_{a_x} at the excitation wavelength not accounting for fluorophore absorption is 1×10^{-3} mm^{-1}; μ_{a_m} at the emission wavelength is zero. The average values of $\eta\mu_{a_{x\rightarrow m}}$ and τ within the object were 1×10^{-3} mm^{-1} and 1 ns, respectively (expected) and 0.8×10^{-3} mm^{-1} and 0.7 ns, respectively (reconstructed). Spurious unphysically high values of $\eta\mu_{a_{x\rightarrow m}}$ and τ have been replaced by the average background fluorescence yield and lifetime, respectively, obtained from the inversion.
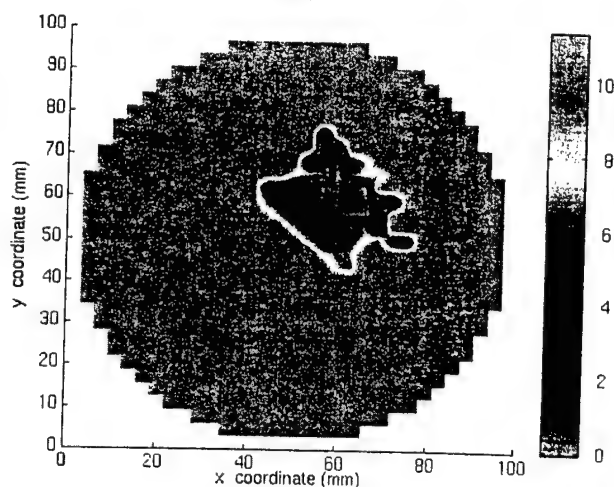
rescing chromophores, whereas simulated experiment 5.B included a finite chromophore absorption of excitation and fluorescent light that could be considered physiological. Finally, simulated experiment 5.C evaluated the ability to determine the location of two hidden objects within the tissue phantom, whereas 5.D examined the reconstruction when the uptake ratio (ratio of fluorescent yield in heterogeneity to that in the background) was 20.

A. Single Heterogeneity with Optical Contrast from $(\tau)_j$ and $(\eta\mu_{a_{x\rightarrow m}})_j$ with Absorption of Excitation and Fluorescent Light by Chromophores

To calculate the experimental data for the first case, the fluorescence yields, $\eta\mu_{a_{x\rightarrow m}}$, for the background

and a single object were chosen as 1×10^{-5} mm^{-1} and 1×10^{-3} mm^{-1}, respectively, and the lifetimes, τ, for the background and the object were chosen as 10 and 1 ns, respectively. During the inverse image reconstruction, no *a priori* knowledge of either the object location or the background fluorescence properties was assumed and a uniform guess of 1×10^{-5} mm^{-1} and 10 ns was given for $\eta\mu_{a_{x\rightarrow m}}$ and τ, respectively. Convergence was achieved in fewer than 50 iterations (computational time on a Sun-Sparc 10 was 2 h) for a two-dimensional 17×17 grid. The average values of $\eta\mu_{a_{x\rightarrow m}}$ and τ in the grid points that occupy the simulated object converge within 50 iterations to the values of $\eta\mu_{a_{x\rightarrow m}} = 0.93 \times 10^{-3}$ mm^{-1} and $\tau = 1.03$ ns, which are close to the
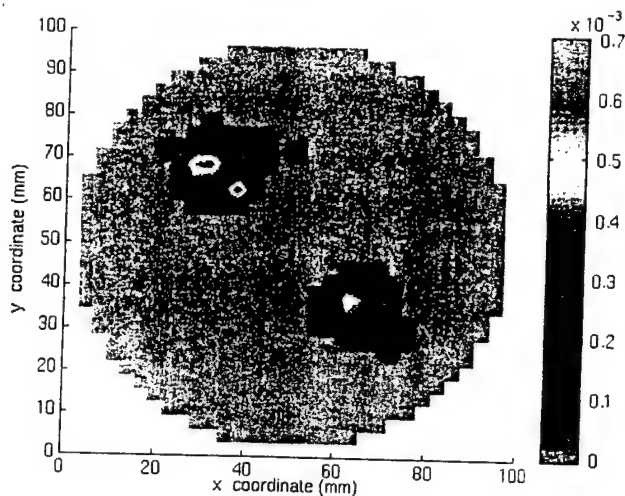
Fig. 9. Reconstructed spatial map of fluorescence yield, $\eta\mu_{a_{x-m}}$, on a two-dimensional, 33×33 grid for the case described in Subsection 5.C. $\mu_{a_{x-}}$ at the excitation wavelength not accounting for fluorophore absorption is zero; μ_{a_m} at the emission wavelength is also zero. The Gaussian noise that was introduced in the phase had a standard deviation of 1°. The object locations and sizes are recovered correctly. The average values of $\eta\mu_{a_{x-m}}$ within the two objects were top left, 1×10^{-3} mm^{-1} (expected) and 2×10^{-3} mm^{-1} (reconstructed); bottom right, 2×10^{-3} mm^{-1} (expected) and 1.8×10^{-3} mm^{-1} (reconstructed). Spurious unphysically high values of $\eta\mu_{a_{x-m}}$ have been replaced by the average background fluorescence yield obtained from the inversion.

correct values of $\eta\mu_{a_{x-m}} = 1 \times 10^{-3}$ mm^{-1} and $\tau = 1$ ns, as shown in Figs. 6(a) and 6(b) and listed in Table 4. Figures 7(a) and 7(b) illustrate the reconstructed images of $\eta\mu_{a_{x-m}}$ and τ, respectively, and are representative of the expected images. The images were smoothed by interpolation in this and subsequent cases. During the reconstruction, it was observed that some grid points, often on or close to the periphery, had unphysically high values of the yield as well as lifetime. Typically, these grid points were loners and were surrounded by grid points with reasonable yield and lifetime values. The high values of lifetime lead to a lower

magnitude of fluorescence generation and offset the effect of high yield values. We believe that additional criteria, such as smoothness of the reconstructed maps, may alleviate the spurious background peak values. In this study, these spurious values were replaced by the average background fluorescence yield and lifetime obtained from the inversion. In the subsequent reconstructions, spurious values were similarly handled.

The average values of $\eta\mu_{a_{x-m}}$ in the grid points that occupy the simulated background converge within 50 iterations to 9×10^{-5} mm^{-1} in comparison with the correct value of 1×10^{-5} mm^{-1} (data not shown for brevity). The value of background τ converges to 5.4 ns, which is also far from the correct value of 10 ns. Both discrepancies are attributed to the fact that most of the signal contribution is due to the object, with the object-to-background uptake ratio being 100:1. The dependence of the final images on the choice of the initial guess was examined by providing an initial uniform guess of 1×10^{-4} mm^{-1} and 10 ns for $\eta\mu_{a_{x-m}}$ and τ, respectively. This resulted in images similar to those obtained with the first guess.

The location of the heterogeneity was identified as consisting of all the grid points with $\eta\mu_{a_{x-m}}$ higher than 35% (arbitrarily chosen) of the peak value of $\eta\mu_{a_{x-m}}$ [Fig. 7(a)]. The average of the coordinates of all the identified object grid points was the position (60.8, 58.5), which is close to position (60, 60) that was used to simulate the experimental data. As listed in Table 3, the area of the heterogeneity based on our arbitrary definition for identification was 742 mm^2, close to that used to generate our simulated experimental data. In addition, upon inspection of Fig. 7(a), one can note that values of $\eta\mu_{a_{x-m}}$ for the object on grid points closer to the center of the phantom were higher than those toward the periphery. This is due to a reduction of signal contributions of grid points located farthest away from source and detectors. This is reflected in a smaller value in the Jacobian matrices and results in a poorer reconstruction at the center of the phantom.

B. Single Heterogeneity with Optical Contrast from $(\tau)_j$ and $(\eta\mu_{a_{x-m}})_j$ with Absorption of Excitation and Fluorescent Light by Chromophores

The same hidden object location as well as optical parameters were used as described in Subsection 5.A, except that a uniform background chromophore absorption coefficient of the excitation light, μ_{a_x}, of 1×10^{-3} mm^{-1}, and of the fluorescent light, μ_{a_m} of 1×10^{-3} mm^{-1}, was used to generate the simulated experimental data. Although excitation light propagation was not employed for image reconstruction, we considered this optical property known to estimate the best possible performance for inverse image reconstruction under physiological conditions. The two-dimensional reconstructed spatial map of the fluorescence yield, $\eta\mu_{a_{x-m}}$, and lifetime, τ, are shown in Figs. 8(a) and 8(b), respectively. The image quality is slightly

Table 4. Fluorescence Lifetime τ and Yield $\eta\mu_{a_{x-m}}$ of the Simulated Heterogeneities: Comparison of Expected and Reconstructed Values

Case	$\eta\mu_{a_{x-m}}$ (Object) (mm^{-1})	τ (Object) (ns)
5.A	1.0×10^{-3} (expected)	1.0 (expected)
	0.93×10^{-3} (obtained)	1.03 (obtained)
5.B	1.0×10^{-3} (expected)	1.0 (expected)
	2.1×10^{-3} (obtained)	4.1 (obtained)
5.C		
Top left object	1.0×10^{-3} (expected)	1.0 (expected)
	2×10^{-3} (obtained)	4.1 (obtained)
Bottom right object	2.0×10^{-3} (expected)	2.0 (expected)
	1.8×10^{-3} (obtained)	3.5 (obtained)
5.D	2.0×10^{-4} (expected)	1.0 (expected)
	7.0×10^{-4} (obtained)	4 (obtained)

inferior with respect to both the size as well as the shape of the hidden object. As shown in Table 3, the mean value of location of the object according to our criterion based on $\eta\mu_{a_{x-m}}$ occurred at position (59, 58), consistent with the conditions used to simulate the experimental data. The dimension of the heterogeneity based on our arbitrary definition for identification (all grid points with $\eta\mu_{a_{x-m}}$ higher than 35% of the maximum) was 683 mm^2, which is close to that used to generate our simulated experimental data. The average values of $\eta\mu_{a_{x-m}}$ and τ in the grid points that occupy the simulated object converge within 50 iterations to the values of $\eta\mu_{a_{x-m}} = 2.1 \times 10^{-3}$ mm^{-1} and $\tau = 4$ ns, which are slightly higher than the values used to generate the simulated experimental data (see Table 4). The average values of $\eta\mu_{a_{x-m}}$ and τ in the grid points that occupy the simulated background converge within 50 iterations to values similar to those reported in Case 5.A.

C. Two Heterogeneities with Optical Contrast from $(\tau)_j$ and $(\eta\mu_{a_{x-m}})_j$ with No Absorption of Excitation and Fluorescent Light by Chromophores

In Case 5.C, the same optical parameters were used in forward calculations as described in Subsection 5.A, except that the fluorescence yields, $\eta\mu_{a_{x-m}}$, for objects 1 and 2 were chosen as 1×10^{-3} mm^{-1} and 2×10^{-3} mm^{-1}, respectively, and lifetimes, τ, for the objects were chosen as 1 ns and 2 ns, respectively. Two 20-mm-diameter circular objects were placed along a diagonal at the coordinates shown in Table 3 within a 100-mm-diameter circular tissue phantom.

Again during the reconstruction, no *a priori* knowledge of either the object location or the background fluorescence properties was assumed and the values of yield $\eta\mu_{a_{x-m}}$ and lifetime τ were found at all the grid points on a 33×33 grid. The two-dimensional reconstructed spatial map of the fluorescence yield, $\eta\mu_{a_{x-m}}$, is shown in Fig. 9. The object locations (x, y) obtained are given in Table 3 and match well with the conditions used to generate the simulated experimental data. The areas of the objects from the reconstructed image (all grid points with $\eta\mu_{a_{x-m}}$ higher than 35% of the maximum) were 381 mm^2 (top left, object 1) and 342 mm^2 (bottom right, object 2), slightly larger than inputs to the forward problem. The average values of $\eta\mu_{a_{x-m}}$ and τ in the grid points that occupy the simulated object converge within 100 iterations to the values of $\eta\mu_{a_{x-m}} = 2 \times 10^{-3}$ mm^{-1} and $\eta\mu_{a_{x-m}} = 1.8 \times 10^{-3}$ mm^{-1} for objects 1 and 2, respectively, which again is close to the expected values of 1×10^{-3} mm^{-1} and 2×10^{-3} mm^{-1}. Lifetimes of the two objects were found to be 4.1 and 3.5 ns, respectively, whereas the expected values were 1 and 2 ns, respectively. The quantitative values of $\eta\mu_{a_{x-m}}$ and τ obtained from the inverse solution are currently unsatisfactory, and research is in progress to improve the solution procedure. The background value of $\eta\mu_{a_{x-m}}$ agrees well with the expected value of $1.0 \times$
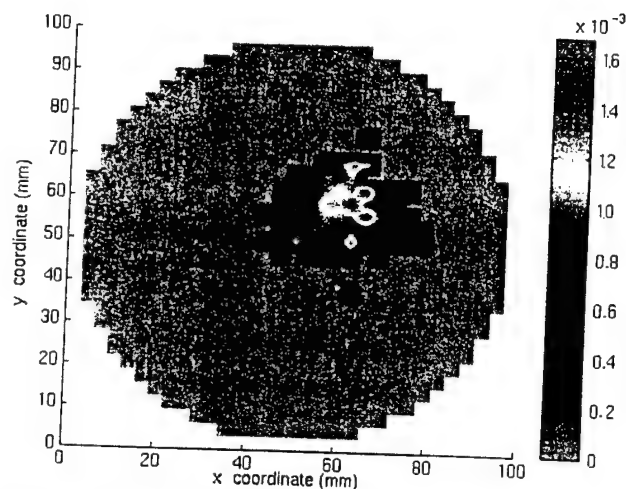

Fig. 10. Reconstructed spatial map of fluorescence yield, $\eta\mu_{a_{x-m}}$, on a two-dimensional, 33×33 grid for the case described in Subsection 5.D. μ_{a_x} at the excitation wavelength not accounting for fluorophore absorption is 1×10^{-3} mm^{-1}; μ_{a_m} at the emission wavelength is the same. The average value of $\eta\mu_{a_{x-m}}$ within the object was 2×10^{-4} mm^{-1} (expected) and 7.0×10^{-4} mm^{-1} (reconstructed). Spurious unphysically high values of $\eta\mu_{a_{x-m}}$ have been replaced by the average background fluorescence yield obtained from the inversion.

10^{-5} mm^{-1}, whereas the value of the background lifetime was poorly reconstructed.

D. Single Heterogeneity with Optical Contrast from $(\tau)_j$ and $(\eta\mu_{a_{x-m}})_j$ with Absorption of Excitation and Fluorescent Light by Chromophores and an Uptake Ratio of 20

The same hidden object location as well as optical parameters were used as described in Subsection 5.A, except that a uniform background chromophore absorption coefficient, μ_{a_x}, of 1×10^{-3} mm^{-1} as well as μ_{a_m} at the emission wavelength of 1×10^{-3} mm^{-1} were used to generate the simulated experimental data, and Gaussian noise was added as discussed above. Also, the values of $\eta\mu_{a_{x-m}}$ for the background and the object were chosen as 1×10^{-5} mm^{-1} and 2×10^{-4} mm^{-1}, thus giving an uptake ratio of 20. Again, although excitation light propagation was not employed for image reconstruction, we considered this optical property to be known in order to estimate the best possible performance for inverse image reconstruction under physiological conditions. The two-dimensional reconstructed spatial map of the fluorescence yield, $\eta\mu_{a_{x-m}}$, is shown in Fig. 10. The image quality with respect to both the size as well as the shape of the hidden object is good. As shown in Table 3, the mean value of location of the object according to our criterion based on $\eta\mu_{a_{x-m}}$ occurred at position (61, 57), consistent with the conditions used to simulate the experimental data. The dimension of the heterogeneity based on our arbitrary definition for identification (all grid points with $\eta\mu_{a_{x-m}}$ higher than 35% of the maximum) was 693 mm^2, which is close to that used to generate our simulated experimental data. The average values of

$\eta\mu_{a_{x\to m}}$ and τ in the grid points that occupy the simulated object converge within 50 iterations to the values of $\eta\mu_{a_{x\to m}} = 7 \times 10^{-4}$ mm^{-1} and $\tau = 4$ ns, which are slightly higher than the values used to generate the simulated experimental data (see Table 4). The average values of $\eta\mu_{a_{x\to m}}$ and τ in the grid points that occupy the simulated background converge within 50 iterations to values similar to those reported in Case 5.A. Nonetheless, it is shown that image reconstruction may be successful even in the case of uptake ratio as small as 20.

The performance of the inverse imaging algorithm may be improved by including additional information obtained from multifrequency measurements and from excitation wavelength measurements. In addition, the appropriate weighting of grid point contributions based on the signal strength may also improve reconstruction results.

6. Conclusions

The fluorescent yield and lifetime of an endogenous fluorophore may be sensitive to local environments, providing specificity for contrast of diseased over normal tissues and optimal detection of disease by using optical techniques.[32] Our simulated experiments show that it is possible to reconstruct the fluorescent yield and lifetime of embedded fluorophores in tissue-mimicking scattering media from frequency-domain measurements of fluorescent phase shift and ac amplitude or amplitude modulation. As we have shown in Subsection 5.C, the reconstruction of lifetime can be problematic by using the reemitted fluorescent signal at one modulation frequency. This is in agreement with O'Leary et al.,[33] who resorted to the need for measurements in the absence of fluorophore (background properties) as well as in its presence for lifetime reconstruction as suggested from multipixel measurements for photon migration imaging.[34] Currently, we are experimentally investigating the implementation of FLI by using both excitation and fluorescent wavelengths as well as multifrequency measurements to improve inverse solutions that predict both fluorescent yield and lifetime.

Appendix A: Nomenclature

c,	velocity of light
$D(r)$,	optical diffusion coefficient
f,	modulation frequency
I,	identity matrix
i,	detector number, $i = 1, 20$
$\bar{\bar{J}}$,	Jacobian matrix relating the sensitivity of optical parameters to the detector response
j,	grid point number
$j_{i,j}$,	individual elements of Jacobian matrix $\bar{\bar{J}}$
k,	source number, $k = 1,4$
M,	log of ac amplitude of modulated fluorescent light
r,	position
$S(r, \omega)$,	source term for the modulated light at position r and frequency ω

Greek

χ^2,	merit function representing the least-squares error
$\Phi(r, \omega)$,	complex number representing the photon flux in the frequency domain at position r and frequency ω
η,	quantum yield of the fluorescent probe or dye
μ_a,	average absorption coefficient of the tissue
μ_{a_m},	absorption coefficient of the fluorescence light by both the nonfluorescing chromophores and fluorophore
μ_{a_x},	absorption coefficient of the excitation light by both the nonfluorescing chromophores and fluorophore
$\mu_{a_{m\to}}$,	absorption coefficient of the fluorescence light by both the nonfluorescing chromophores
$\mu_{a_{x\_}}$,	absorption coefficient of the excitation light by the nonfluorescing chromophores
$\mu_{a_{x\to m}}$,	absorption coefficient of the excitation light by the fluorophore
μ_s',	effective scattering coefficient of the tissue
θ,	phase shift of the modulated light wave with respect to the modulated wave at the source
σ,	standard deviation of the Gaussian noise representing the experimental uncertainty
$\tau(r)$,	lifetime of the activated probe or dye at location r
ω,	angular modulation frequency, given by $2\pi f$

Subscripts

obs,	observed or experimental data
x,	excitation light
m,	fluorescence or emission light

Appendix B: Jacobian Matrices

We provide more details about the elements of the Jacobian matrices introduced in Section 4. Element $j_{i,j}$ of a Jacobian matrix represents the sensitivity of the response of detector i to changes in the optical property at grid point j. Here as an example we show the response of detector 16 for source A (see Fig. 1) to changes in τ and $\eta\mu_{a_{x\to m}}$ at all the grid points for the case described in Subsection 5.A for the first iteration during inversion when $\mu_{a_{x\_}}$ was chosen as zero. Similar results are observed for other cases. Figures 11(a) and 11(b) show the elements of Jacobian matrices $\bar{\bar{J}}(\theta, \tau)$ and $\bar{\bar{J}}(M, \tau)$, respectively, where τ at each of the grid points was increased by 5%. Similarly, Fig. 11(c) shows the elements of Jacobian matrix $\bar{\bar{J}}(M, \eta\mu_{a_{x\to m}})$, where $(\eta\mu_{a_{x\to m}})$ at each of the grid points was increased by 1%. Most of the elements of $\bar{\bar{J}}(\theta, \tau)$ and $\bar{\bar{J}}(M, \eta\mu_{a_{x\to m}})$ are positive, whereas most of the elements of $\bar{\bar{J}}(M, \tau)$ are negative. This is according to our expectation of systems with no scattering. The dependence on scatter has, of course, been taken into account in the above example.
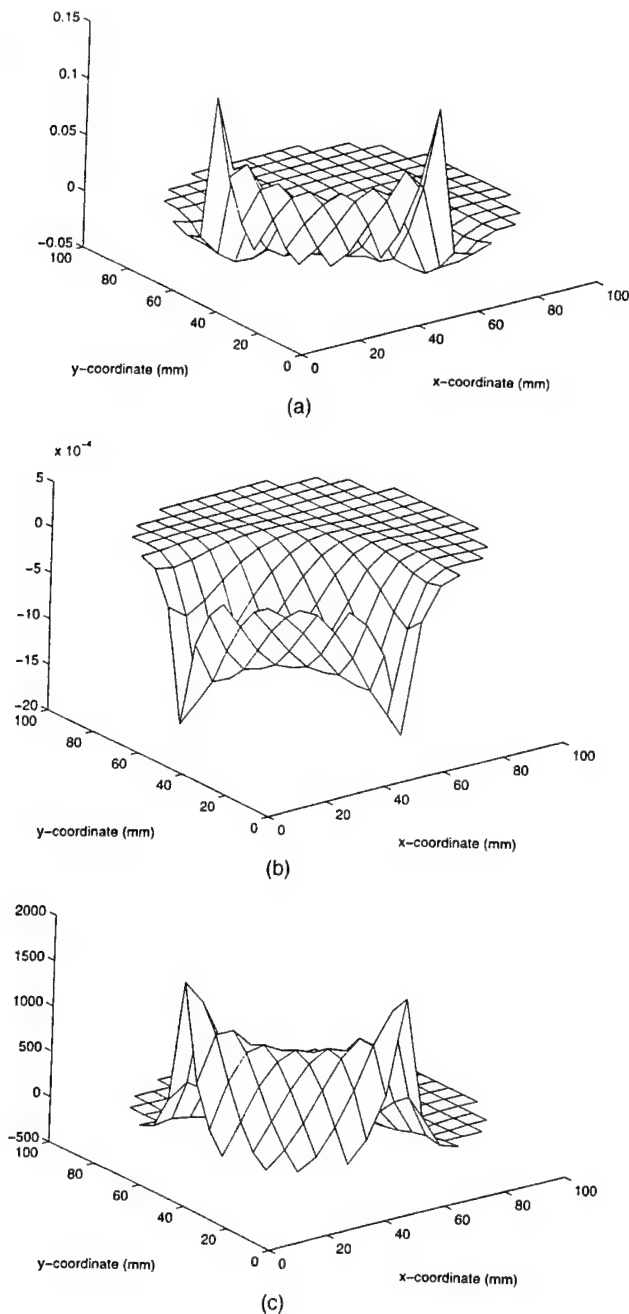
(a)

(b)

(c)

Fig. 11. Jacobian (a) $\bar{\bar{J}}(\theta, \tau)$, (b) $\bar{\bar{J}}(M, \tau)$, (c) $\bar{\bar{J}}(M, \eta\mu_{a_{x \to m}})$ for the case described in Subsection 5.A for source A, detector 16, and iteration 1. During the computation of the Jacobians, the values of τ for (a) and (b) and $\eta\mu_{a_{x \to m}}$ for (c) at each individual grid point were increased by 5%, 5%, and 1%, respectively.

References

1. R. L. Sheridan, K. T. Schomaker, L. C. Lucchina, J. Hurley, L. M. Yin, R. G. Tompkins, M. Jerath, A. Torri, K. Greaves, D. Bua, and N. S. Nishioka, "Burn depth estimation by use of indocyanine green fluorescence: initial human trial," J. Burn Care Rehabil. **16**, 602–604 (1995).

2. W. Poon, K. T. Schomaker, T. F. Deutsch, and R. L. Martuza, "Laser-induced fluorescence: experimental intraoperative delineation of tumor resection margins," J. Neurosurg. **76**, 679–686 (1992).

3. S. Andersson-Engels, J. Johansson, U. Stenram, K. Svanberg, and S. Svanberg, "Time-resolved laser-induced fluorescence spectroscopy for enhanced demarcation of human atherosclerotic plaques," J. Photochem. Photobiol. **4**, 363–369 (1990).

4. S. Andersson-Engels, J. Ankerst, J. Johansson, K. Svanberg, and S. Svanberg, "Laser-induced fluorescence in malignant and normal tissue of rats injected with benzoporphryin derivative," Photochem. Photobiol. **57**, 978–983 (1993).

5. B. C. Wilson, E. M. Sevick, M. S. Patterson, and B. Chance, "Time-dependent optical spectroscopy and imaging for biomedical applications," Proc. IEEE **80**, 918–930 (1992).

6. S. Mordon, J. M. Devoisselle, and V. Maunoury, "In vivo pH measurement and imaging of a pH-sensitive fluorescent probe (5-6-carboxyfluorescein): instrumental and experimental studies," Photochem. Photobiol. **60**, 274–279 (1994).

7. D. A. Russell, R. H. Pottier, and D. P. Valenzeno, "Continuous noninvasive measurement of in vivo pH in conscious mice," Photochem. Photobiol. **59**, 309–313 (1994).

8. S. A. Vinogradov, L. W. Lo, W. T. Jenkins, S. M. Evans, C. Koch, and D. F. Wilson, "Noninvasive imaging of the distribution in oxygen in tissue in vivo using near-infrared phosphors," Biophys. J. **70**, 1609–1617 (1996).

9. E. M. Sevick-Muraca, C. L. Hutchinson, and D. Y. Paithankar, "Optical tissue biodiagnostics using fluorescence lifetime," Opt. Photon. News **7**, 25–28 (1996).

10. B. W. Pogue, M. S. Patterson, H. Jiang, and K. D. Paulsen, "Initial assessment of a simple system for frequency domain diffuse optical tomography," Phys. Med. Biol. **40**, 1709–1729 (1995).

11. R. L. Barbour, H. L. Graber, Y. Wang, J. Chang, and R. Aronson, "Perturbation approach for optical diffusion tomography using continuous-wave and time-resolved data," in *Medical Optical Tomography: Functional Imaging and Monitoring*, G. Müller, B. Chance, R. Alfano, S. Arridge, J. Beuthan, E. Gratton, M. Kaschke, B. Masters, S. Svanberg, and P. Vander Zee, eds. (SPIE, Bellingham, Wash., 1993), pp. 87–120.

12. M. A. O'Leary, D. A. Boas, B. Chance, and A. G. Yodh, "Experimental images of heterogeneous turbid media by frequency-domain diffusing photon tomography," Opt. Lett. **20**, 426–428 (1995).

13. H. Jiang, K. D. Paulsen, U. L. Osterberg, B. W. Pogue, and M. S. Patterson, "Optical image reconstruction using frequency-domain data: simulations and experiments," J. Opt. Soc. Am. **13**, 253–266 (1996).

14. T. L. Troy, D. L. Page, and E. M. Sevick-Muraca, "Optical properties of normal and diseased breast tissues: prognosis for optical mammography," J. Biomed. Opt. **1**, 342–355 (1996).

15. G. Lopez, T. L. Troy, C. L. Hutchinson, J. S. Reynolds, and E. M. Sevick-Muraca, "Fluorescent contrast agents for biomedical optical imaging using frequency-domain techniques," J. R. Lakowicz and R. B. Thompson, eds., Proc. SPIE **2980** (1997).

16. J. Wu, Y. Wang, L. Perelman, I. Itzkan, R. Dasari, and M. Feld, "Three-dimensional imaging of objects embedded in turbid media with fluorescence and Raman spectroscopy," Appl. Opt. **34**, 3425–3430 (1995).

17. K. M. Yoo, Z.-H. Zang, S. A. Ahmed, and R. R. Alfano, "Imaging objects hidden in scattering media using a fluorescence-absorption technique," Opt. Lett. **16**, 1252–1254 (1991).

18. A. Knuttel, J. M. Schmitt, R. Barnes, and J. R. Knutson, "Acousto-optic scanning and interfering photon density waves for precise localization of an absorbing (or fluorescent) body in a turbid medium," Rev. Sci. Instrum. **64**, 638–644 (1993).

19. M. A. O'Leary, D. A. Boas, B. Chance, and A. G. Yodh, "Re-

radiation and imaging of diffuse photon density waves using fluorescent inhomogeneities," J. Lumin. **60&61,** 281–286 (1994).

20. R. Cubbedu, G. Canti, P. Taroni, and G. Valentini, "Time-gated fluorescence imaging for the diagnosis of tumors in a murine model," Photochem. Photobiol. **57,** 480–485 (1993).

21. E. M. Sevick-Muraca and C. L. Burch, "The origin of phosphorescent and fluorescent signals in tissues," Opt. Lett. **19,** 1928–1930 (1994).

22. M. S. Patterson and B. W. Pogue, "A mathematical model for time-resolved and frequency-domain fluorescence spectroscopy in tissues," Appl. Opt. **33,** 1963–1974 (1994).

23. C. L. Hutchinson, J. R. Lakowicz, and E. M. Sevick-Muraca, "Fluorescence lifetime based sensing in tissues: a computational study," Biophys. J. **68,** 1574–1582 (1995).

24. C. L. Hutchinson, T. L. Troy, and E. M. Sevick-Muraca, "Fluorescence-lifetime determination in tissues or other scattering media from measurement of excitation and emission kinetics," Appl. Opt. **35,** 2325–2332 (1996).

25. S. R. Fulton, C. E. Ciesielski, and W. H. Schubert, "Multigrid methods for elliptic problems: a review," Mon. Weather Rev. **114,** 943 (1986).

26. J. C. Adams, "MUDPACK: multigrid portable Fortran software for the efficient solution of linear elliptic partial differential equations," Appl. Math. Comp. **34,** 133 (1989).

27. R. A. Day, Jr. and A. L. Underwood, *Quantitative Analysis*, 6th ed. (Prentice-Hall, Englewood Cliffs, N.J., 1991), p. 446.

28. E. M. Sevick, J. K. Frisoli, C. L. Burch, and J. R. Lakowicz, "Localization of absorbers using frequency-domain measurements of time-dependent photon migration," Appl. Opt. **33,** 3562–3570 (1994).

29. X. D. Li, M. A. O'Leary, D. A. Boas, B. Chance, and A. G. Yodh, "Fluorescent diffuse photon density waves in homogeneous and heterogeneous turbid media: analytic solutions and applications," Appl. Opt. **35,** 3746–3758 (1996).

30. T. J. Yorkey, J. G. Webster, and W. J. Tompkins, "Comparing reconstruction algorithms for electrical impedance tomography," IEEE Trans. Biomed. Eng. **BME-34,** 843–852 (1987).

31. W. H. Press, S. A. Teukolsy, W. T. Vetterling, and B. P. Flannery, *Numerical Recipes: The Art of Scientific Computing* (Cambridge U. Press, New York, 1992).

32. E. M. Sevick-Muraca, D. Y. Paithankar, C. L. Hutchinson, and T. L. Troy, "Analysis of photon migration for optical diagnosis," in *Ultrasensitive Biochemical Diagnostics*, G. E. Cohn, S. A. Soper, and C. Chen, eds., Proc. SPIE **2680,** 114–123 (1996).

33. M. A. O'Leary, D. A. Boas, D. X. Li, B. Chance, and A. G. Yodh, "Fluorescence lifetime imaging in turbid media," Opt. Lett. **21,** 158–160 (1996).

34. E. M. Sevick, J. R. Lakowicz, H. Szamacinski, K. Nowaczyk, and M. L. Johnson, "Frequency domain imaging of absorbers obscured by scattering," J. Photochem. Photobiol. B **16,** 169–185 (1992).

Role of higher-order scattering in solutions to the forward and inverse optical-imaging problems in random media

E. M. Sevick-Muraca, D. L. Heintzelman, J. Lee, T. L. Troy, and D. Y. Paithankar

From analytical and numerical solutions that predict the scattering of diffuse photon density waves and from experimental measurements of changes in phase shift θ and ac amplitude demodulation M caused by the presence of single and double cylindrical heterogeneities, we show that second- and higher-order perturbations can affect the prediction of the propagation characteristics of diffuse photon density waves. Our experimental results for perfect absorbers in a lossless medium suggest that the performance of fast inverse-imaging algorithms that use first-order Born or Rytov approximations might have inherent limitations compared with inverse solutions that use iterative solutions of a linear perturbation equation or numerical solutions of the diffusion equation. © 1997 Optical Society of America

Key words: Photon migration imaging, image reconstruction, frequency-domain, inverse problem, biomedical optical imaging.

1. Introduction

With the development of near-infrared (NIR)-emitting laser diodes and the realization that NIR light can travel several centimeters through tissue, numerous groups have embarked upon development of optical imaging as a new medical imaging modality. Although approaches such as monitoring the vanishingly small component of coherent light with sophisticated techniques of Kerr filtering,[1] time gating,[2] and conservation of light polarization[3] vary, other approaches focus on monitoring the predominant optical signal re-emitted from tissues: the multiply scattered signal. Continuous wave,[4] time domain,[5] and frequency domain[6-8] measurements of multiply scattered light have been performed in simulated and experimental tissue phantom studies as well as in human studies.[9] However, the use of these measurements for reconstructing maps of internal tissue optical properties for diagnostic imaging has been problematic because the geometric correlation between incident and detected radiation is destroyed by multiple scattering.

While some investigators have used direct image reconstruction approaches that use measured optical data to directly form an image,[9-11] others have sought full solution to the inverse-imaging problem, which relates external time-dependent measurements made at the periphery to an optical property map of interior volumes through the optical diffusion equation.[6-8,12-16] Two approaches for solving the inverse solution have been adopted. In the first approach, the fluence associated with a propagating photon density wave launched at source position ρ_s and detected at the tissue periphery at position ρ_d [denoted $\Phi(\rho_s, \rho_d)$] is related to the fluence assumed in the absence of any optical heterogeneities [denoted $\Phi_{inc}(\rho_s, \rho_d)$] and the internal optical property perturbation map $\Delta(\rho)$ through a Fredholm integral equation of the first kind:

$$\Phi(\rho_s, \rho_d) = \Phi_{inc}(\rho_s, \rho_d) + \int G(\rho, \rho_d)\Phi_0(\rho_s, \rho)\Delta(\rho)\partial^3\rho, \quad (1)$$

where $G(\rho, \rho_d)$ is the Green's function to the diffusion equation,

$$G(\rho, \rho_D) = \frac{1}{4\pi(\rho - \rho_D)} \exp\{i[(-\mu_a + i\omega/c_n)/D]^{1/2}(\rho - \rho_D)\},$$

describing the propagation of light from position ρ to the detector at ρ_d, and Φ_0 is the incident wave impinging at position ρ. If one assumes that the incident wave impinging upon the position ρ can be

approximated by the fluence predicted in the absence of heterogeneities (i.e., $\Phi_0 \to \Phi_{inc}$, known as the Born approximation), upon measurement of fluence at a variety of source–detector separations and upon discretization of Eq. (1), an optical map of perturbations $\Delta(\rho)$ can be obtained to a first-order approximation.[15] However, the Born approximation $\Phi_0 \to \Phi_{inc}$ does not account for second- and higher-order effects that might arise from the rescattering of photon density waves associated with neighboring inhomogeneities. In addition, this approach assumes that perturbations in optical properties at a position ρ_j do not influence the propagation of light from position ρ_{j+1} to detector ρ_d as described by the Green's function $G(\rho, \rho_d)$.

Investigators use the Born iterative method (BIM) to account for strong perturbations and for second- and higher-order scattering effects by using the first-order approximation of optical property perturbations $\Delta(\rho)$ to iteratively calculate Φ_0 or the fluence incident at position ρ. Yao et al.[16] have shown that the BIM tends to compensate for the underprediction of the scattering and absorption properties of a single heterogeneity in an otherwise uniform medium that would occur when the Born approximation (or single iteration) is used. In addition to the BIM, the distorted Born iterative method (DBIM) represents a refinement in that it also recompiles the Green's functions $G(\rho, \rho_d)$ to reflect changes in light propagation and it should speed convergence. Yet to date there has been no investigation that addresses how these iterative reconstruction algorithms affect the resolution or, more precisely, how these linear perturbation approaches can be used to accurately image closely positioned, multiple heterogeneities between which nonlinear second- and higher-order scattering effects exist.

In contrast with this inversion approach, Jiang et al.[7,8] and Arridge et al.[14] have used full numerical solution to the diffusion equation that describes the interdependence of voxel optical properties and their contribution to the re-emitted optical signal detected from cw and frequency domain measurements. With this approach, the second- and higher-order scattering arising from multiple inhomogeneities, which are not accounted for in the first iterations of Born and Rytov approximations, are incorporated in the forward and inverse solutions. The inversion consists of the relating of spatial changes of optical properties on detected frequency domain measurements through numerical solution of the diffusion equation and then solving an update to the map of optical properties from the difference between the signals that are measured and those that are predicted by the forward solution to the diffusion equation. Note that convergence on the optical properties is achieved with these numerical approaches and not with the iterative Born and Rytov approaches. Nonetheless, while the computational investment of iterative but analytically based inversions is less than that of full numerical solution of the diffusion equation, the relative performance of these two inverse-solution approaches has yet to be evaluated.

For this reason we embarked on a study to assess the contributions of neighboring heterogeneities by using experimental, numerical, and analytical computations of scattered photon density waves from perfect light-absorbing cylinders. Specifically we experimentally and computationally monitor the multiple scattering of photon density waves between two neighboring perfect cylindrical absorbers embedded in a tissue-mimicking scattering medium to assess the higher-order perturbation effects on a re-emitted, detected photon density wave. In the following we briefly review the theory of higher-order perturbation effects as predicted from the experimental frequency domain measurements as well as from the Helmholtz equations. In addition, we present experimental measurements and numerical solutions of the optical diffusion equation that show the errors, which can be significant, introduced by neglecting second-order effects. These errors can define the limits of resolution for two perfect absorbers in the inverse-solution approaches that do not use BIM, DBIM, or the full numerical solution of the optical diffusion equation. We comment on these effects when contrast is caused by mechanisms other than a perfect absorber.

2. Theoretical Background for Perturbations Associated with Diffuse Photon Density Waves

Our work to assess the contributions of higher-order perturbations has been motivated by the work of Boas et al.[15] Their approach for image reconstruction from diffusely propagating photon density waves uses analytical expressions to describe the complex fluence of a propagating photon density wave $\Phi(\rho)$ in the presence of m heterogeneities by superposition of incident $\Phi_{inc}(\rho)$ and scattered $\Phi_{scat,k}{}^n(\rho)$ waves, from body k and of the order of n:

$$\Phi(\rho) = \Phi_{inc}(\rho) + \sum_{n=1}^{x} \sum_{k=1}^{m} \Phi_{scat,k}{}^n(\rho). \qquad (2)$$

The second-order effects caused by the scattering of a photon density wave between two objects are illustrated in Fig. 1, from the work of Boas and co-workers, and delineate the contribution of these effects to the detected photon density wave $\Phi(\rho)$. Second- and higher-order-scattering effects arise from the rescattering of an incident wave between the two bodies. Boas et al. assume that second-order-scattering effects (denoted by the dotted line in Fig. 1) are negligible under most circumstances. We explore this assumption, using experimental, numerical, and analytical predictions of second-order contributions.

A. Analysis of Experimental Measurements of Photon Density Waves

To measure second-order contributions we experimentally measured the detected photon density wave in the presence of one light-absorbing object alone, Φ_{k1}; object two alone, Φ_{k2}; and with both objects present, $\Phi_{k1,k2}$, as a function of object positions ρ_1 and
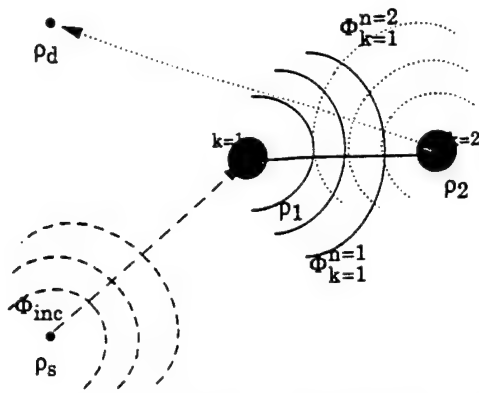
Fig. 1. Schematic illustrating the incident wave Φ_{inc} originating from the source at position ρ_s (dashed lines); the first-order scattered wave $\Phi_{scat,k1}{}^{n=1}$ arising from the first heterogeneity (solid lines); and the second-order wave $\Phi_{scat,k2}{}^{n=2}$ arising from rescatter of the first-order wave off the second heterogeneity (dotted lines).
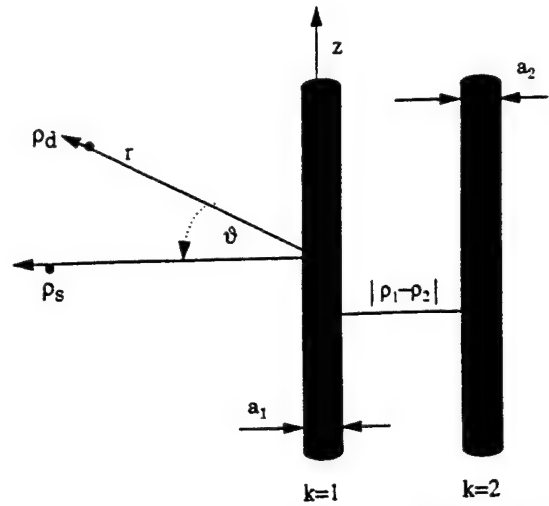

Fig. 2. Schematic detailing the geometry used in the calculation of scattered waves from analytical expression. The centroid of the cylinder is the origin, with z denoting the length, angle ϑ denoting the angle in the plane containing the source and the detector, and r denoting the radial direction.

ρ_2 and separation between the two objects $\rho_1 - \rho_2$ (see Fig. 2). From Eq. (2), expressions can be written for measurements of Φ_{k1} and Φ_{k2} made at detector position ρ_d in the presence of single objects:

$$\Phi_{k1}(\rho_d) = \Phi_{inc}(\rho_d) + \Phi_{scat,k1}{}^{n=1}(\rho_d), \qquad (3)$$

$$\Phi_{k2}(\rho_d) = \Phi_{inc}(\rho_d) + \Phi_{scat,k2}{}^{n=1}(\rho_d), \qquad (4)$$

where $k1$ denotes the presence of the first body alone and $k2$ denotes the presence of the second body. With simple algebraic manipulation of Eqs. (2)–(4),

predicted by measurements of $\Phi_{k1}(\rho_d)$, $\Phi_{k2}(\rho_d)$, and $\Phi_{inc}(\rho_d)$:

$$\Phi_{k1,k2}(\rho_d) = \Phi_{k=1}(\rho_d) + \Phi_{k=2}(\rho_d) - \Phi_{inc}(\rho_d). \qquad (6)$$

Because we report our results in terms of phase shift and amplitude demodulation, Eq. (6) can be written as

$$\theta_{k1,k2}(\rho_d) = \tan^{-1}\left(\frac{M_{k1}\sin\theta_{k1} + M_{k2}\sin\theta_{k2} - M_{inc}\sin\theta_{inc}}{M_{k1}\cos\theta_{k1} + M_{k2}\cos\theta_{k2} - M_{inc}\cos\theta_{inc}}\right), \qquad (7)$$

$$M_{k1,k2}(\rho_d) = [(M_{k1}\cos\theta_{k1} + M_{k2}\cos\theta_{k2} - M_{inc}\cos\theta_{inc})^2 + (M_{k1}\sin\theta_{k1} + M_{k2}\sin\theta_{k2} - M_{inc}\sin\theta_{inc})^2]^{1/2}. \qquad (8)$$

an expression accounting for higher-order-scattering effects can be written for the photon density wave in the presence of both objects $\Phi_{k1,k2}(\rho_d)$:

$$\Phi_{k1,k2}(\rho_d) = \Phi_{k1}(\rho_d) + \Phi_{k2}(\rho_d) - \Phi_{inc}(\rho_d)$$
$$+ \Phi_{scat,k1,k2}{}^{n=2}(\rho_d) + \Phi_{scat,k1,k2}{}^{n=3}(\rho_d) + \dots . \qquad (5)$$

For this study, it is assumed that third- and higher-order scattered waves are considered to have insignificant contributions to the measured fluence when compared with those of first- and second-order scattered waves.

From frequency domain measurements of phase shift θ and ac amplitude M, values of the complex fluence $\Phi = Me^{-i\theta}$ can be obtained (1) in the presence of the first object alone, $\Phi_{k1}(\rho_d)$; (2) in the presence of the second object alone, $\Phi_{k2}(\rho_d)$; (3) in the presence of both objects, $\Phi_{k1,k2}(\rho_d)$; and (4) in the absence of any inhomogeneities, $\Phi_{inc}(\rho_d)$. If second-order effects, i.e., $\Phi_{scat,k1,k2}{}^{n=2}(\rho_d)$, are negligible, from Eq. (5) it follows that measurements of $\Phi_{k1,k2}(\rho_d)$ should be

B. Analytical Predictions of Phase Shift and Amplitude Modulation Owing to Two Perfect Absorbing Cylinders

The complex fluence describing the propagation of a photon density wave can also be computed analytically from the Helmholtz equations.[15,16] The complex fluence propagating from a source point at ρ_s through an infinite random medium and received at position ρ, in the absence of an optical heterogeneity, is given by

$$\Phi_{inc}(\rho) = S_{source}(\rho_s)\frac{\exp\left[i\left(\frac{-\mu_a + i\omega/c_n}{D}\right)^{1/2}(\rho - \rho_d)\right]}{4\pi D(\rho - \rho_d)}, \qquad (9)$$

where S_{source} describes the phase and strength of modulation of the source located at position ρ_s; c_n is the speed of light in the medium; and D is the optical diffusion coefficient that is governed by the absorption μ_a and the isotropic scattering μ'_s, coefficients of the continuous or homogeneous medium:

$$D = 1/3(\mu_a + \mu_s'). \qquad (10)$$

In this study, we approximate a point-modulated source at the periphery of a large cylinder as a point-modulated source located at the interface of a semi-infinite medium. In this case the fluence is written in cylindrical coordinates and at the surface ($z = 0$) given by[17]

$$\Phi_{\mathrm{inc}}(\rho_d) = S_{\mathrm{source}}(\rho_s) \frac{1}{4\pi D}$$

$$\times \left(\begin{array}{c} \dfrac{\exp\left\{-\left(\dfrac{\mu_a + i\omega/c_n}{D}\right)^{1/2}\left[(\rho_s - \rho_d)^2 + (z - z_0)^2\right]^{1/2}\right\}}{\left[(\rho_s - \rho_d)^2 + (z - z_0)^2\right]^{1/2}} \\ \\ -\dfrac{\exp\left[-\left(\dfrac{\mu_a + i\omega/c_n}{D}\right)^{1/2}\left[(\rho_s - \rho_d)^2 + (z + z_0)^2\right]^{1/2}\right]}{\left[(\rho_s - \rho_d)^2 + (z + z_0)^2\right]^{1/2}} \end{array} \right),$$

(11)

where z_0 is one isotropic scattering length ($1/\mu'_s$).

The first-order ($n = 1$) scattered wave from the $k1$ infinitely long cylinder in an infinite medium is given by[15,18]

$$\Phi_{\mathrm{scat},k1}{}^{n=1}(\rho_d) = -\Phi_{\mathrm{inc}} \sum_{m=1}^{x} \int_0^x \cos(m\vartheta)\cos(pz)$$

$$\times K_m\left\{\left[p^2 + \left(\frac{-\mu_a + i\omega/c_n}{D}\right)\right]^{1/2} \rho_d\right\}$$

$$\times K_m\left\{\left[p^2 + \left(\frac{-\mu_a + i\omega/c_n}{D}\right)\right]^{1/2} \rho_s\right\}$$

$$\times \left[\frac{DxI_m'(x)I_m(y) - D_{k1}'yI_m(x)I_m'(y)}{DxK_m'(x)I_m(y) - D_{k1}'yK_m(x)I_m'(y)}\right]\mathrm{d}p,$$

(12)

where D_k' is the optical diffusion coefficient within the cylinder k; I_m and K_m are modified Bessel functions; and parameters x and y are given as

$$x = \left[p^2 + \left(\frac{-\mu_a + i\omega/c_n}{D}\right)\right]^{1/2} a_k,$$

$$y = \left[p^2 + \left(\frac{-\mu_a' + i\omega/c_n}{D_k'}\right)\right]^{1/2} a_k;$$

and a_k is the radius of cylinder $k1$. Radius ρ_d, angle ϑ, and length z denote the coordinates of the detector relative to the center of the infinite cylinder $k1$ (Fig. 2). The incident wave upon the infinite cylinder Φ_{inc} is computed from Eq. (11). A similar expression can be written for $\Phi_{\mathrm{scat},k2}{}^{n=1}$.

We calculated second-order-scattering contributions by evaluating the scattered wave originating

from the second object ($k2$) as the incident wave upon the first object ($k1$). In other words,

$$\Phi_{\mathrm{scat},k1}{}^{n=2}(\rho_d) = -\Phi_{\mathrm{scat},k2}{}^{n=1} \sum_{m=1}^{x} \int_0^x \cos(m\vartheta)\cos(pz)$$

$$\times K_m\left\{\left[p^2 + \left(\frac{-\mu_a + i\omega/c_n}{D}\right)\right]^{1/2} \rho_d\right\}$$

$$\times K_m\left\{\left[p^2 + \left(\frac{-\mu_a + i\omega/c_n}{D}\right)\right]^{1/2} \rho_s\right\}$$

$$\times \left[\frac{DxI_m'(x)I_m(y) - D_{k1}'yI_m(x)I_m'(y)}{DxK_m'(x)I_m(y) - D_{k1}'yK_m(x)I_m'(y)}\right]\mathrm{d}p,$$

(13)

where the incident wave upon cylinder $k1$ is now the first-order scattered wave $\Phi_{\mathrm{scat},k2}{}^{n=1}$ that is computed from Eq. (12). A similar expression can be written for $\Phi_{\mathrm{scat},k2}{}^{n=2}$. Because the optical properties and the diameter of the two cylinders were identical in this study, we consider the case in which $D_1' = D_2'$ and $a_1 = a_2$.

With the approach described above, the fluence detected at position ρ_d can be computed inclusive of first-order-scattering effects [i.e., $\Phi(\rho_d) = \Phi_{\mathrm{inc}}(\rho_d) + \sum_{k=1}^2 \Phi_{\mathrm{scat},k}{}^{n=1}(\rho_d)$], as well as second-order scattering effects [i.e., $\Phi(\rho_d) = \Phi\mathrm{inc}(\rho_d) + \sum_{n=1}^2 \sum_{k=1}^2 \Phi_{\mathrm{scat},k}{}^{n}(\rho_d)$]. From final values of complex fluence, the phase shift and amplitude demodulation can be predicted from the simple relationships:

$$\theta(\rho_d) = \tan^{-1} \frac{\mathrm{Im}[\Phi(\rho_d)]}{\mathrm{Re}[\Phi(\rho_d)]}$$

(14)

$$M(\rho_d) = (\{\mathrm{Im}[\Phi(\rho_d)]\}^2 + \{\mathrm{Re}[\Phi(\rho_d)]\}^2)^{1/2}.$$

(15)

3. Materials and Methods

A. Experimental Measurements of Phase Shift Owing to Two Cylindrical Absorbers

To experimentally measure $M_{k1,k2}(\rho_d)$, $M_{k1}(\rho_d)$, $M_{k2}(\rho_d)$, $M_{\mathrm{inc}}(\rho_d)$, $\theta_{k1,k2}(\rho_d)$, $\theta_{k1}(\rho_d)$, $\theta_{k2}(\rho_d)$, and $\theta_{\mathrm{inc}}(\rho_d)$, frequency domain measurements were made with an apparatus that uses picosecond pulsed light at 780 nm with an average power of 1.3 W. Details of the apparatus are described elsewhere.[19] The phantom consisted of a plexiglass cylinder (with a 16.5-cm diameter and 20-cm height) filled with a 0.5% Intralipid solution (Kabi Pharmacia, Inc., Clayton, N.C.). As illustrated in Fig. 3, light was delivered to a peripheral point on the cylinder with a 1000-μm fiber (Model HCP-M1000T-08, Spectron Specialty Optics Co., Avon, Conn.) and collected through a second fiber located 4 circumferential cm from the incident source. Bakelite plastic rods (diameter, 3.175 mm) were painted black to provide perfectly light-absorbing inhomogeneities. Measurements of $\theta(\rho_d)$ and $M(\rho_d)$ at 80 MHz were conducted as the rods were moved in tandem along the plane perpendicular to a line connecting the source
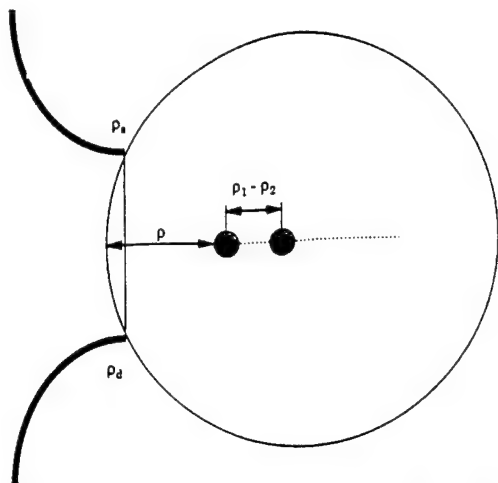
Fig. 3. Schematic illustrating the geometry of the experimental measurements.

and detector. Positioning was achieved with a motion controller (Model PMC200-P, Newport Corp., Irvine, Calif.) and a motorized actuator (Newport Model 850B). The actuator position was accurate to within 0.0050 mm. Phase and ac modulation were recorded as the distance between the center of the first absorbing cylinder, and the wall of the phantom was varied from 0 to 5 cm in 20 increments. When the two objects were moved in tandem, their separation distances (ρ_1–ρ_2) between the centers of the two perfect absorbers were 6, 10, and 20 mm. Three measurements were taken at each position. Measurements of phase shift and ac amplitude demodulation are reported relative to the absence case or θ_{inc} or M_{inc}.

B. Analytical Prediction of Phase Shift and Amplitude Modulation Owing to Two Absorbing Cylinders

In addition to the measurements of second-order interactions with the experimental approach described above, predictions of interactions between absorbers were computed analytically with Eqs. (11)–(15) with a modified version of an algorithm written by Boas that is available through the internet.[20] Complex fluence incorporating first- and second-order-scattering contributions was used to calculate phase shift owing to two infinite cylinders that effectively act as perfect absorbers ($\mu_a = 2$ cm^{-1}, $\mu_s' = 10$ cm^{-1}) in a turbid, semi-infinite medium mimicking our phantom ($\mu_a = 0.02$ cm^{-1}, $\mu_s' = 10$ cm^{-1}). Zero fluence boundary conditions were assumed and used in the algorithm.

C. Numerical Prediction of Phase Shift and Amplitude Demodulation Owing to Two Absorbing Heterogeneities
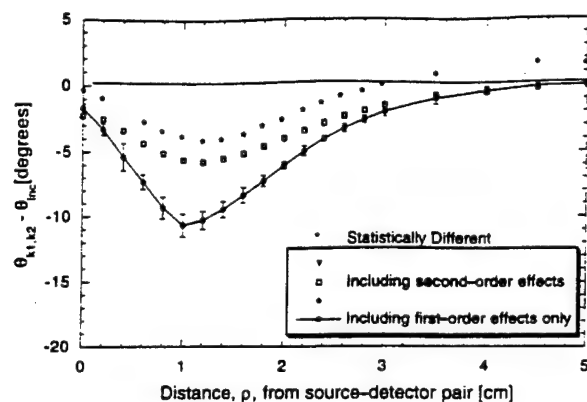
In addition to experimental measurements and analytical calculations, two-dimensional finite-element computations were conducted to predict the phase shift and amplitude demodulation resulting from first- and second-order interactions. The computations were performed on an Ultra 2 Sun Sparc workstation with a MATLAB partial differential equation toolbox. We solved the frequency domain diffusion equation for light propagation to determine the fluence from an 80-MHz sinusoidally modulated light source. The simulated phantom was an infinite cylinder 16.5 cm in diameter. The optical properties of the medium were set to mimic the experimental conditions of 0.02 cm^{-1} for the absorption coefficient μ_a and 10 cm^{-1} for the isotropic scattering coefficient μ_s'. We modeled the nearly perfect absorbers in these computations as infinite cylindrical rods and we approximated these by increasing the absorption coefficient to 100 times that of the surrounding medium ($\mu_a = 2.0$ cm^{-1}). The scattering coefficient for the object was set to that of the surroundings ($\mu_s' = 10$ cm^{-1}) to mimic the analytical computations. The phantom was discretized into 66,048 triangular elements that contained 33,281 nodes. A partial current boundary condition was used to approximate light reflection and transmission across the boundary of the phantom as would be expected in the experimental measurements. Although our meshing did not permit representation of the perfect absorber as a volume excluded for light transport, we approximated the heterogeneity with a high absorption coefficient because others have shown that the propagation characteristics are comparable.[18] It is noteworthy that, although these computations do not exactly mimic the experimental measurements described below, they nonetheless adequately describe the contributions of second-order scattering effects. The forward solution was obtained for each absorbing cylinder alone and then in combination. The results were analyzed in a manner similar to the analysis of the experimental results with Eq. (7) and (8).

## 4. Results and Discussion

A. Experimental Results

Figures 4(a)–4(c) and 5(a)–5(c) illustrate the phase shift and the amplitude demodulation changes as a function of position of the pair of perfect absorbers whose centers are separated by 6, 10, and 20 mm. The symbols denote individual measurements of phase shift difference in the presence of the two hidden objects, and the symbols connected by the lines denote the phase shift and the amplitude demodulation calculated from Eq. (7) and (8) with measurements made in the absence and in the presence of a single individual absorber. The measured values of phase shift and amplitude demodulation denoted by the open symbols are therefore reflective of higher-order contributions, whereas the solid line reflects only first-order contributions. Paired Student's t-test shows that there is a significant difference ($p < 0.005$) between the set of phase shift and amplitude demodulation measurements and that predicted by Eqs. (7) and (8) for two perfect light-absorbing objects separated by 6, 10, and 20 mm and positioned at various distances from the source and the detector [Figs. 4(a)–5(c)]. Our results also show that the magnitude of second-order effects is greatest for two
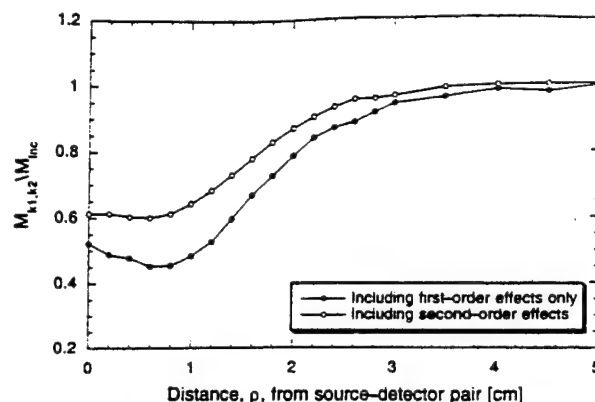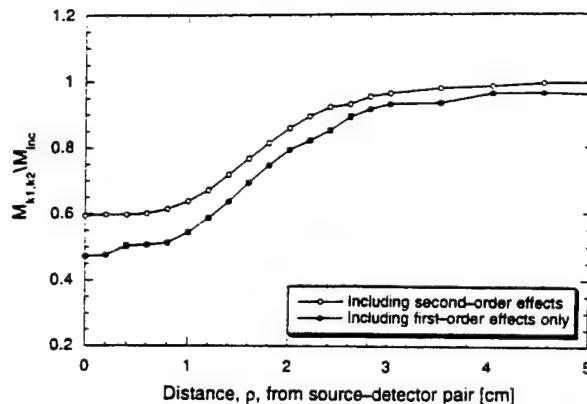
(a)
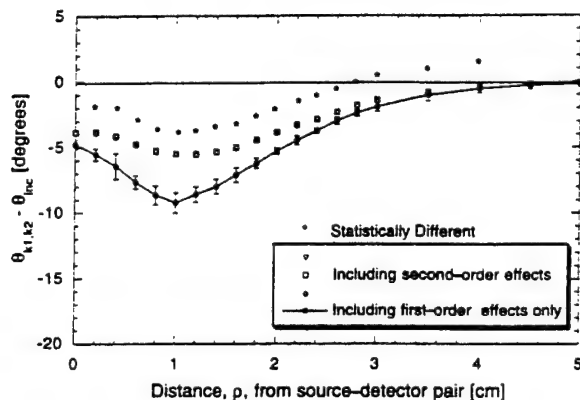
(b)
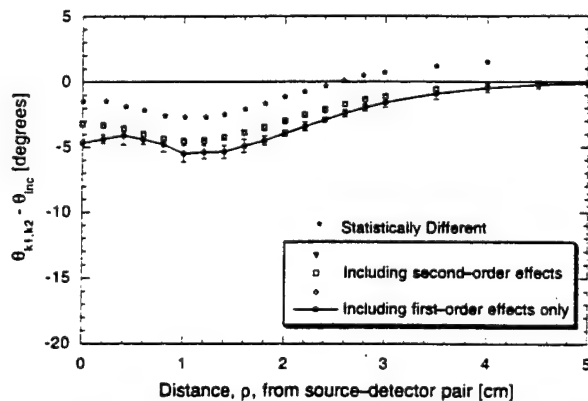
(c)

Fig. 4. Experimental values of $\theta_{k1,k2}-\theta_{inc}$ the phase difference (in degrees) relative to the absence condition as a function of distance from the source–detector pair. The symbols denote individual measurements in the presence of two cylinders separated by distances of (a) 6, (b) 10, and (c) 20 mm, whereas the line connects predictions from Eq. (7) and measurements of θ_{k1}, θ_{k2}, and θ_{inc}. The error bars denote the propagation of measurement errors (standard deviation) associated with θ_{k1}, θ_{k2}, and θ_{inc}. The x axis is reported as the distance between the wall and the first cylinder ($k1$). The asterisks denote significant difference ($p < 0.005$, paired Student's t-test) between the values experimentally measured and those obtained from Eq. (7).
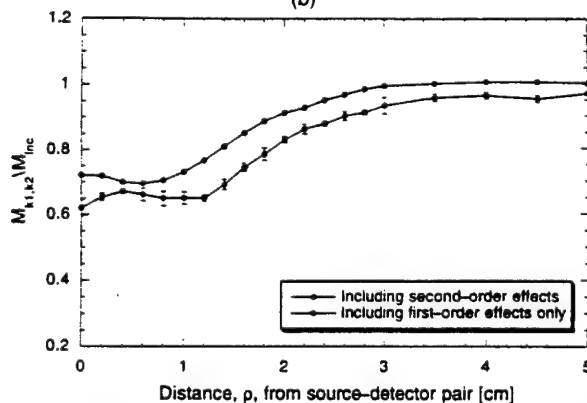
absorbing heterogeneities spaced 6 mm apart and becomes smaller at 10 and 20 mm. The paired t-test indicates that there are significant differences at the 99.5% confidence levels (indicated by the asterisks in

(a)

(b)

(c)

Fig. 5. Experimental values of $M_{k1,k2}/M_{inc}$ (in arbitrary units) relative to the absence condition as a function of distance from the source–detector pair. The symbols denote individual measurements in the presence of two cylinders separated by distances of (a) 6 (b) 10, and (c) 20 mm, whereas the line connects predictions from Eq. (8) and measurements of M_{k1}, M_{k2}, and M_{inc}. The error bars denote the propagation of measurement errors (standard deviation) associated with M_{k1}, M_{k2}, and M_{inc}. The x axis is reported as the distance between the wall and the first cylinder ($k1$).

Fig. 4) between individual experimental phase-shift values that reflect first- and higher-order scattering contributions to the detected signal and those computed values that are indicative of first-order effects only. From the data for 6-mm absorber separation illustrated in Fig. 4(a), it can be seen that the actual experimental measurements of phase shift change
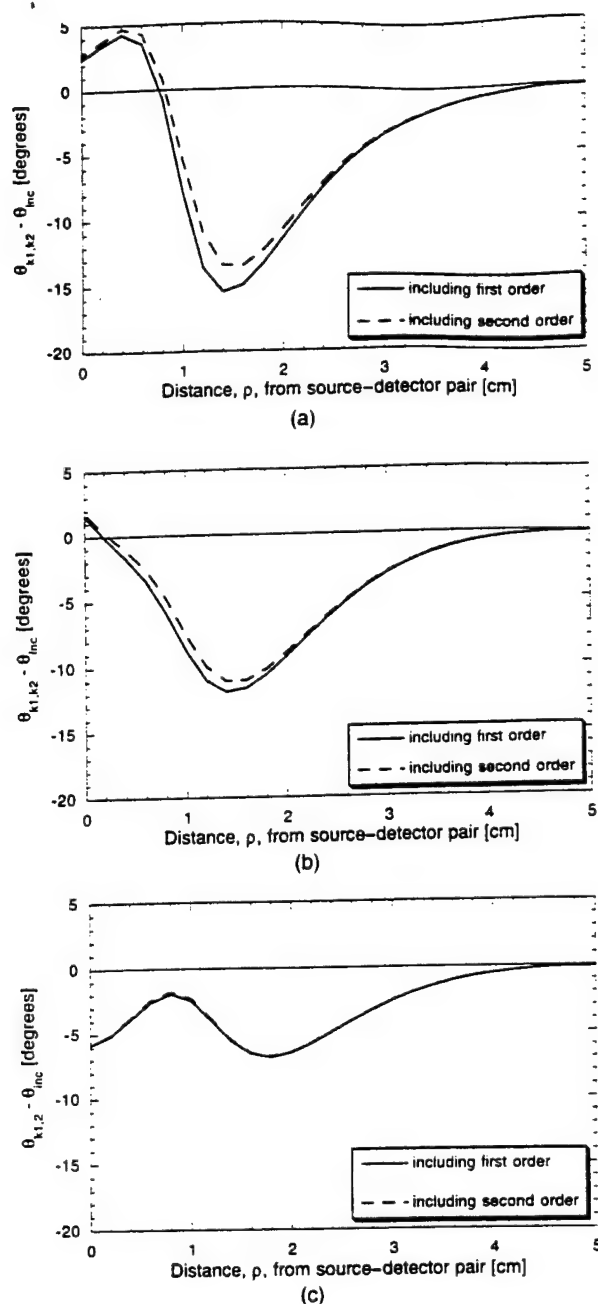
(a)

(b)

(c)

Fig. 6. Values of $\theta_{k1,k2} - \theta_{inc}$ (in degrees) calculated from the analytical prediction of first-order (solid line) and inclusive of second-order (dashed line)-scattering effects as a function of distance (cm) from the source-detector pair for two absorbing cylinders separated by (a) 6, (b) 10, and (c) 20 mm. The x axis is reported as the distance between the wall and the first cylinder ($k1$) and the phase shift reported relative to the absence case.

caused by two objects are smaller than those predicted by Eq. (7), in which second- and higher-order perturbations are not accounted for. At greater distances from the source and detector, agreement between experimental and predicted phase shift change suggests that second-order effects may indeed be negligible, even for the smallest separation, but only in a region where the objects' contributions to the detected signal is comparatively small. This is reason-
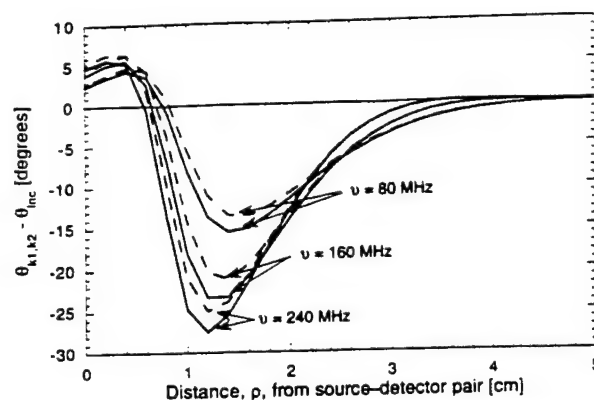

Fig. 7. Values of $\theta_{k1,k2} - \theta_{inc}$ (in degrees) calculated from analytical prediction of first order (solid curve) and inclusive of second order (dashed curve) for two absorbing cylinders separated by 6 mm and interrogated at 80, 160, and 240 MHz.

able because second-order effects are expected to increase with proximity to the source and the detector. From our studies, it appears that separations greater than 20 mm are necessary for their accurate resolution through perturbative reconstruction approaches when perfect absorbers are involved.

B. Analytical Computations

Our experimental results are also validated by the analytical predictions that account for first- and second-order scattering contributions. Figures 6(a)–6(c) depict the qualitative trends seen in the experimental data presented for phase difference in Figs. 4(a)–4(c). There appears to be good agreement between the trends observed experimentally with various separation distances and analytical predictions. Specifically, higher-order contributions significantly perturb the detected phase shift values when the separations between the center of two absorbing cylinders are 6 mm [Fig. 6(a)] and 10 mm [Fig. 6(b)]. The contribution of higher-order scattering from cylindrical absorbers is not significant when the separation distance is 20 mm [Fig. 6(c)]. However comparison with experimental results shows that there are differences in the absolute magnitude and shape of the phase shift change versus object distance. These distances are most likely caused by the differences in the boundary conditions, geometry, and absorber strength between the analytical and the experimental results. Nonetheless, the trends confirm experimental results that the presence of second-order perturbations reduces the phase shift change owing to two light-absorbing bodies. Neglecting second-order effects could cause an underestimation of absorption strength or size when reconstruction algorithms based on first-order perturbations are used.

In addition, we investigated the variation of second-order perturbations with modulation frequency as shown in Fig. 7. The simulated data of phase shift change versus position of the heterogeneities is depicted for two cylindrical absorbers ($d =$
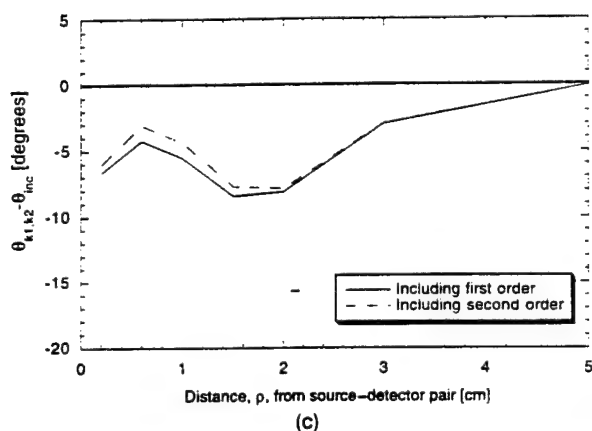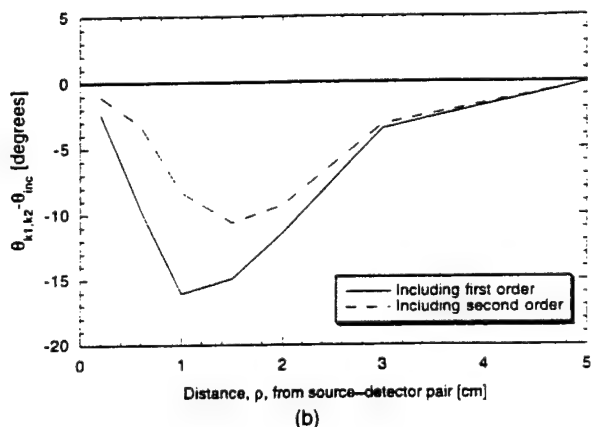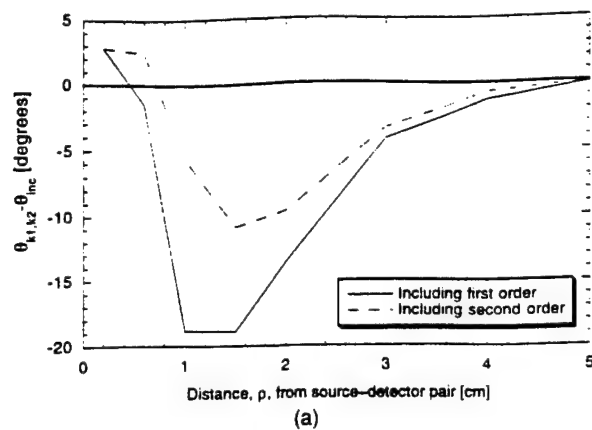
Fig. 8. Finite element computations of $\theta_{k1,k2}-\theta_{inc}$ (in degrees) relative to an absence condition for considering only first-order (solid line) and including second-order (dashed line) perturbations as a function of distance (cm) from the source–detector pair for absorbing cylinders separated by (a) 6, (b) 10, and (c) 20 mm. The x axis is reported as the distance between the wall and the first cylinder ($k1$) and the phase shift reported relative to the absence case.
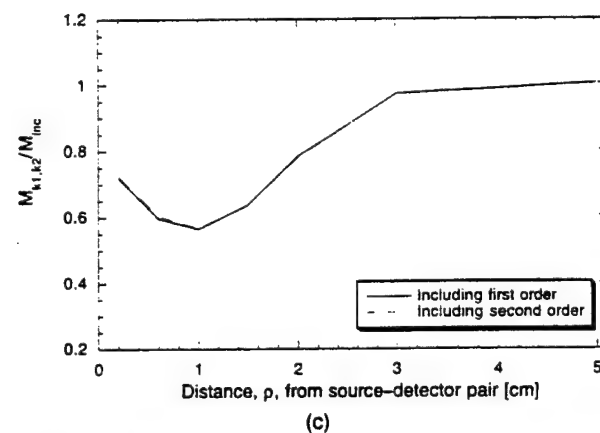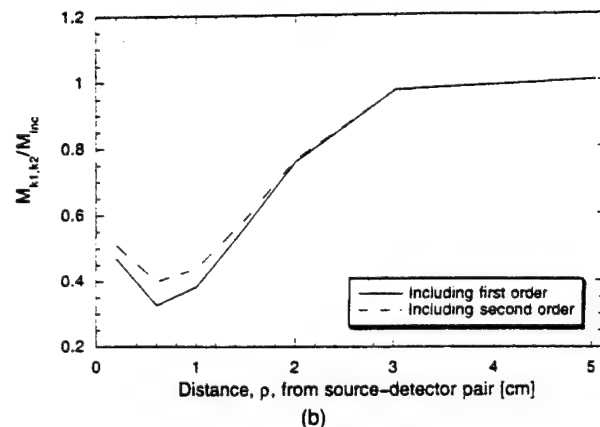

Fig. 9. Finite element computations of $M_{k1,k2}/M_{inc}$ (in arbitrary units) referenced to an absence condition for both the first-order (solid line) and the second-order (dashed line) perturbations as a function of distance (cm) from the source–detector pair for absorbing cylinders separated by (a) 6, (b) 10, and (c) 20 mm. The x axis is reported as the distance between the wall and the first cylinder ($k1$) and the modulation ratio is reported relative to the absence case.

3.125 mm, $\mu_a = 2$ cm^{-1}) separated by 6 mm in a semi-infinite medium. Again, the phase shift is reported relative to the absence case, and the distance is reported from the wall to the center of the first cylinder. Three frequencies were evaluated: 80, 160, and 240 MHz. The absolute value of phase shift increases with frequency, but the contribution of

second-order effect remains roughly the same absolute value. Consequently the error in assuming negligible second-order scattering effects becomes smaller at increasing frequencies. This is expected because increased damping of a rescattered photon density wave occurs at higher modulation frequencies. While these results intimately depend upon the choice of optical properties, they nonetheless

point out that the error in neglecting second-order scattering contributions in analytically based reconstructions becomes smaller with increasing modulation frequencies. Of course the error reduction occurs at the expense of interrogating a smaller volume of tissue with a source modulated at an increased frequency.[21]

C. Finite Element Computations

Our experimental results were validated not only by analytical predictions but also with finite element computations. Figures 8(a)–9(c) show the numerical computations that correspond to the experimental phase shift data presented in Figs. 4(a)–5(c). Again there appears to be good agreement between the trends of the experimental and the analytical results and the numerical solutions. Also, higher-order contributions perturb the detected phase shift values when the separation distances between the two rods are 6 mm [Fig. 8(a)] and 10 mm [Fig. 8(b)]. The contribution of higher-order scattering from the cylindrical absorbers is not significant when the separation distance is 20 mm [Fig. 8(c)]. Figures 9(a)–9(c) show the amplitude demodulation relative to an absence condition. The modulation data also show results similar to those obtained experimentally. These computation results confirm that the presence of second-order perturbations is important for two light-absorbing objects that are less than 20 mm apart.

5. Conclusions

In summary, our experimental measurements show that the contributions of higher-order scattering of propagating photon density waves may not always be insignificant. While our analytical and numerical computations do not exactly reproduce experimental conditions (i.e., two-dimensional finite element, semi-infinite geometry, etc.), they nonetheless demonstrate that the experimental trends can be attributed to second-order effects. Under conditions of high contrast caused by absorption, analytical approaches to the inverse imaging algorithm may restrict the resolution and the sensitivity of biomedical optical imaging performed in the frequency domain. An analogy can also be drawn for time domain and cw reconstruction approaches that do not deploy full solutions to the diffusion equation to account for the interdependence of voxel optical properties on measured fluences. Certainly our results are based on the worst-case scenario of perfect absorbers and may have less impact on the image reconstructions involving imperfect absorbers. Under conditions in which multiple heterogeneities are contrasted with their surroundings on the basis of scattering or fluorescence, the first-order perturbation assumption may not be as restrictive. Indeed, if the nonlinearity associated with second-order scattering effects is small, noniterative Born and Rytov approximations are especially attractive because image reconstruction is not computation intensive. Nonetheless, our results suggest that inverse imaging algorithms that depend solely on first-order perturbations caused by local changes in tissue absorption properties may

not provide a reconstruction as accurate as those algorithms that depend on the full numerical calculation of the diffusion equation with specified boundary conditions.

6. Appendix A

1. Nomenclature

a_k	Radius of cylinder k (cm)
c_n	Speed of light through the medium (cm/s)
D	Optical diffusion coefficient of homogeneous medium (cm)
$D_{k'}$	Diffusion coefficient inside the cylinder (cm)
I_n	Modified Bessel function
$I_{n'}$	Derivative of modified Bessel function I_n
K_n	Modified Bessel function
$K_{n'}$	Derivative of modified Bessel function K_n
M	ac demodulation of the incident light (mW/cm^2)
m	Number of objects
p	Integration variable in Helmholtz equation describing scatter from an infinite cylinder (cm^{-1})
S_{source}	Strength of modulated source at position ρ_s, represented as a complex number of amplitude and phase (mW)
x	Variable in Helmholtz equation describing scatter from an infinite cylinder (cm^{-1})
y	Variable in Helmholtz equation describing scatter from an infinite cylinder (cm^{-1})
z	Axial direction of the cylindrical heterogeneities or length (cm)

2. Greek

Φ	Photon fluence (mW/cm^2)
Φ_{inc}	Photon fluence of incident wave or in the absence of heterogeneities (mW/cm^2)
Φ_{scat}	Photon fluence arising from scattered wave (mW/cm^2)
ρ	Position vector (cm)
ρ_s	Position of the source (cm)
ρ_d	Position of detector (cm)
ρ_k	Center position of object k (cm)
θ	Phase shift of light wave (deg or rad)
ϑ	Angle between ρ_s and ρ_d
μ_a	Absorption coefficient of homogeneous surroundings (cm^{-1})
$\mu_{s'}$	Isotropic scattering of homogeneous surroundings (cm^{-1})
$\mu_{a'}$	Absorption coefficient of cylinder (cm^{-1})
$\mu_{s'}$	Isotropic scattering of cylinder (cm^{-1})

3. Subscripts and Superscripts

n	Order of perturbation or nth-order scattering effect
k	Index denoting cylindrical object one, $k1$; two, $k2$; or both objects, $k1$, $k2$
inc	Index denoting absence measurement or condition

References

1. L. M. Wang, P. P. Ho, and R. R. Alfano, "Double-stage picosecond Kerr gate for ballistic time-gated optical imaging in turbid media," Appl. Opt. **32**, 535–540 (1994).

2. B. B. Das, K. M. Yoo, and R. R. Alfano, "Ultrafast time-gated imaging in thick tissues: a step toward optical mammography," Opt. Lett. **18**, 1092–1094 (1993).

3. S. G. Demos, H. Savage, A. S. Heerdt, S. Schantz, and R. R. Alfano, "Time resolved degree of polarization for human breast tissue," Opt. Commun. **124**, 439–442 (1996).

4. J. R. Singer, F. A. Grunbaum, P. Kohn, and J. P. Zubelli, "Image reconstruction of the interior of bodies that diffuse radiation," Science **248**, 990–993 (1990).

5. J. C. Hebden, R. A. Kruger, and K. S. Wong, "Time-resolved imaging through a highly scattering medium," Appl. Opt. **30**, 788–794 (1991).

6. M. A. O'Leary, D. A. Boss, B. Chance, and A. G. Yodh, "Experimental images of heterogeneous turbid media by frequency domain diffusing photon tomography," Opt. Lett. **20**, 426–428 (1995).

7. H. Jiang, K. D. Paulsen, U. L. Osterberg, B. W. Pogue, and M. S. Patterson, "Simultaneous reconstruction of absorption and scattering maps in turbid media from near-infrared frequency domain data," Opt. Lett. **20**, 2128–2130 (1995).

8. H. Jiang, K. D. Paulsen, and U. L. Osterberg, "Optical image reconstruction using frequency domain data: simulations and experiments," J. Opt. Soc. Am. A **13**, 253–266 (1996).

9. M. A. Franceschini, K. T. Moesta, S. Fantini, G. Gaida, E. Gratton, H. Jess, W. W. Mantulin, M. Seeber, P. M. Schlag, and M. Kaschke, "Frequency-domain techniques enhance optical mammography: initial clinical results," Proc. Natl. Acad. Sci. USA **94**, 6468–6473 (1997).

10. E. M. Sevick, J. R. Lakowicz, H. Szmacinski, K. Nowaczyk, and M. L. Johnson, "Frequency domain imaging of absorbers obscured by scattering," J. Photochem. Photobiol. B **16**, 169–185 (1992).

11. E. Gratton, W. Mantulin, M. J. van de Ven, J. Fishkin, M. Maris, and B. Chance, "A novel approach to laser tomography," Bioimaging **1**, 40–46 (1993).

12. R. L. Barbour, H. L. Graber, Y. Wang, J. H. Chang, and R. Aronson, "A perturbation approach for optical diffusion tomography using continuous-wave and time resolved data," in *Fiber Optic Sensors: Engineering and Applications*, A. J. Bruinsma and B. Culshaw, eds., Proc. SPIE **1511**, 87–120 (1993).

13. S. R. Arridge, P. van der Zee, M. Cope, and D. T. Delpy, "Reconstruction methods for infra-red absorption imaging," in *Time-Resolved Spectroscopy and Imaging of Tissues*, B. Chance and A. Katzir, eds., Proc. SPIE **1431**, 204–215 (1991).

14. S. R. Arridge, M. Schweiger, M. Hiraoka, and D. T. Delpy, "Performance of an iterative reconstruction algorithm for near-infrared absorption and scatter imaging," in *Photon Migration and Imaging in Random Media and Tissues*, R. R. Alfano and B. Chance, eds., Proc. SPIE **1888**, 360–371 (1993).

15. D. A. Boas, B. O'Leary, B. Chance, and A. G. Yodh, "Scattering of diffuse photon density waves by spherical inhomogeneities within turbid media: analytical solution and applications," Proc. Natl. Acad. Sci. USA **91**, 4887–4891 (1994).

16. Y. Yao, Y. Wang, Y. Pei, W. Zhu, and R. L. Barbour, "Frequency-domain optical imaging of absorption and scattering distributions by a Born iterative method," J. Opt. Soc. Am. A **14**, 325–342 (1997).

17. S. R. Arridge, M. Cope, and D. T. Delpy, "The theoretical basis for the determination of optical path lengths in tissue: temporal and frequency-domain analysis," Phys. Med. Biol. **37**, 1531–1560 (1992).

18. H. C. van de Hulst, *Light Scattering by Small Particles* (Dover, New York, 1981).

19. C. L. Hutchinson, T. L. Troy, and E. M. Sevick-Muraca, "Fluorescence-lifetime determination in tissues or other scattering media from measurement of excitation and emission kinetics," Appl. Opt. **35**, 2325–2332 (1996).

20. D. A. Boas, http://dpdw.eotc.tufts.edu/boas/PMI/pmi.html.

21. E. M. Sevick, J. K. Frisoli, C. L. Burch, and J. R. Lakowicz, "Localization of absorbers in scattering media by use of frequency-domain measurements of time-dependent photon migration," Appl. Opt. **33**, 3562–3570 (1994).

Truncated Newton's optimization scheme for absorption and fluorescence optical tomography: Part I Theory and Formulation

R. Roy and E. M. Sevick-Muraca

The Photon Migration Laboratory, School of Chemical Engineering,

Purdue University, West Lafayette, IN 47907-1283

ranadhir@ecn.purdue.edu, sevick@ecn.purdue.edu

Abstract: The development of non-invasive, biomedical optical imaging from time-dependent measurements of near-infrared (NIR) light propagation in tissues depends upon two crucial advances: (i) the instrumental tools to enable photon "time-of-flight" measurement within rapid and clinically realistic times, and (ii) the computational tools enabling the reconstruction of interior tissue optical property maps from exterior measurements of photon "time-of-flight" or photon migration. In this contribution, the image reconstruction algorithm is formulated as an optimization problem in which an interior map of tissue optical properties of absorption and fluorescence lifetime is reconstructed from synthetically generated exterior measurements of frequency-domain photon migration (FDPM). The inverse solution is accomplished using a truncated Newton's method with trust region to match synthetic fluorescence FDPM measurements with that predicted by the finite element prediction. The computational overhead and error associated with computing the gradient numerically is minimized upon using modified techniques of reverse automatic differentiation.

References:

1 D. A. Boas, M. A. O'Leary, B. Chance and A.G. Yodh, "Scattering of diffuse photon density waves by spherical heterogeneities within turbid media: analytic solutions and applications," *Proc. Natl. Acad. Sci.,* **91**, pp 4887-91, (1994).

2 M. A. O'Leary, D. A. Boas, B. Chance and A.G. Yodh, "Experimental images of heterogeneous turbid media by frequency-domain diffusion photon tomogrpahy," *Opt. Lett.* **20**, 426-428, (1995).

3 R. L. Barbour, H. Graber, Y. Wang J. Chang and R. Aronson, "Perturbation approach for optical diffusion tomography using continuous-wave and time-resolved data," in *Medical Optical Tomography: Functional Imaging and Monitoring,* G. Muller, B. Chance, R. Alfano, J. Beuthan, E. Gratton, M. Kashke, B. Masters, S. Svanberg and P. van der Zee, eds. (SPIE Press, Bellingham, WA., 1993), pp 87-120.

4 Y. Yao, Y. Wang, Y. Pei, W. Zhu and R.L. Barbour, "Frequency-domain optical imaging of absorption and scattering by a Born iterative method," *J. Opt. Soc. Am. A,* **14**, 325-342, (1997).

5 W. C. Chew and Y. M. Wang, "Reconstruction of two-dimensional permittivity distribution using the distorted Born iterative method," *IEEE Trans. On Medical Imaging.* **9**, 218-225, (1995).

6 K. D. Paulsen and H. Jiang, "Spatially varying optical property reconstruction using a finite element diffusion equation approximation," *Med. Phys.* **22**, 691-701, (1995).

7 H. Jiang, K. D. Paulsen, U. L. Osterberg, B.W. Pogue and M. S. Patterson, "Optical image reconstruction using frequency-domain data simulations and experiments," *J. Opt. Soc. Am. A.* **13**, 253-266, (1996).

8 D.Y. Paithankar, A. U. Chen, B.W. Pogue, M. S. Patterson and E. M. Sevick-Muraca, "Imaging of fluorescent yield and lifetime from multiply scattered light re-emitted from tissues and other random media," *Appl. Opt,* **36**,

2260-2272, (1997).

9 M. Schweiger, S. R. Arridge. D. T. Delpy, " Application of the finite-element method for the forward and inverse models in optical tomography," *J. Math. Img. and Vision* **3,** 263-283. (1993)

10 J. J. McKeown ,"On algorithms for sums of squares problems," *Towards global optimization*, edited by Dixon. L. C. W. and Szeeg, G. P., North-Holland Amsterdam, Holland, (1975).

11 M. T. Vespucci, "An efficient code for the minimization of highly nonlinear and large residual least squares functions," *Optimization* **18,** 825-855, (1987).

12 R. R. Meyer, "Theoretical and computational aspects of nonlinear regression," *Nonlinear Programming*, edited by Rosen, J. B., Mangasarian, O. L. and Ritter. K., Academic Press, New York, (1970).

13 L. B. Rall, *Automatic differentiation: Techniques and application. Lecture notes in computer science.* 120, Springer Verlag, (1981).

14 A. Griewank, "On automatic differentiation." edited Iri, M. and Tanaka, K., *Mathematical programming: Recent developments and application*. Kluwer Academic Publishers, pp 83-108, (1989).

15 T. L. Troy, D. L. Page and E. M. Sevick-Muraca, "Optical properties of normal and diseased breast tissues: prognosis for optical mammography," *J. Biomed Opt.* **1,** 342-355, (1996).

16 E. M. Sevick-Muraca, G. Lopez., T. L. Troy, J. S. Reynolds and C. L. Hutchinson, "Fluorescence and absorption contrast mechanisms for biomedical optical imaging using frequency-domain techniques," *Photochemi and Photobiol*, **66**: 55-64, (1997).

17 M. A. O'Leary, D. A. Boas, B. Chance and A.G. Yodh, "Fluorescence lifetime imaging in turbid media," *Opt. Lett.*.**21,** 158-160, (1996).

18 J. Chang, H. L. Graber and R.L. Barbour, "Luminescence optical tomography of dense scattering media," *J. Opt. Soc. Am. A.* **14,** 288-299, (1997).

19 T. L. Troy and E. M. Sevick-Muraca, "Fluorescence lifetime imaging and spectroscopy in random media," in *Applied Fluorescence in Chemistry, Biology, and Medicine*, Rettig, Strehmel, Shrader, Seifert, eds., Springer Verlag, pp. 3-36, (1999).

20 H. Jiang, "Frequency-domain fluorescent diffusion tomography: a finite-element based algorithm and simulations," *Appl. Opt.* **37,** 5337-5343, (1998).

21. Chang, H. L. Graber and R.L. Barbour, "Improved reconstruction algorithm for luminescence optical tomography when background luminophore is present," *Appl Opt.* **37** , 3547-3552, (1998).

22 J. Lee and E. M. Sevick-Muraca, "Lifetime and absorption imaging with fluorescence FDPM," Time-resolved fluorescence spectroscopy and imaging in tissues. E. M. Sevick-Muraca (ed.)., *Proc. Soc. Photo-Opt. Instrum. Eng.*, 3600: (to be published), (1999).

23   A. Ishimaru, *Wave propagation and scattering in random media*,(Academic Press, New York, 1978).

24 M. Schweiger. S. R. Arridge, M. Hiraka D. T. Delpy, " The finite-element method for the propagation of light in scattering media- boundary and source conditions," *Med. Phys* **22,** 1779-1792, (1995)

25 R. A. J. Groenhuis, H. A. Ferwerda and J. J. Ten Bosch. "Scattering and absorption of turbid material determined from reflection measurements," *Appl. Opt.* **22,** 2456-2462, (1983).

26 O. C. Zienkiewcz and R. L. Taylor ,*The finite element methods in engineering science*. (McGraw-Hill, New York, 1989).

27 L. C. W. Dixon and R. C. Price, "Numerical experience with the truncated Newton method for unconstrained optimization," *JOTA*, **56,** 245-255, (1988).

28   R. Roy, *Image reconstruction from light measurements on biological tissue*. Ph. D. thesis, University of Hertfordshire, England,(1996).

29 R. S. Dembo and T. Steihaug, "Truncated Newton algorithms for large-scale unconstrained optimization," *Math Programming* **26,** 190-212, (1983).

30 R. C. Price, *Sparse matrix optimization using automatic differentiation*, Ph. D. thesis, University of Hertfordshire, U. K., (1987).

31 L. Armijo "Minimization of functions having Lipschitz continuous first partial derivatives," *Pacific J. Mathematics* **16,** 1-3. (1966).

32 P. Wolfe, "Convergence condition for ascent method," *SIAM Rev.*, **11** 226-253, (1969).

33 B., Christianson, A. J., Davies, L. C. W. Dixon, R. Roy and P. van der Zee, "Giving reverse differentiation a helping hand," *Opt. Meth. And Software* **8,** 53-67, (1997).

34 A. J., Davies, B. Christianson,, L. C. W. Dixon,, R. Roy and P. van der Zee, "Reverse differentiation and the inverse diffusion problem," *Adv. In Eng. Software* **28,** 217-221, (1997).

35 R. E. Wengert, "A simple automatic derivative evaluation program," *Comm. A. C. M.*, **7,** 463-464, (1964).

1. Introduction

Conventional imaging modalities such as magnetic resonance imaging (MRI) and x-ray computer-aided tomography (x-ray CT) provide high-resolution medical imaging enabled by the direct geometric correlation between incident and detected radiation. Yet the high cost of operating hospital MRI facilities, and the inability to detect important diseases through x-ray

CT imaging suggests an opportunity for the development of near-infrared (NIR) biomedical optical imaging. NIR biomedical optical imaging, or optical tomography, depends upon the low absorbance, yet high scattering of non-mutagenic near-infrared light in the "therapeutic wavelength window" (600-1000 nm) enabling it to safely propagate through several centimeters of tissues. While the propagation of low-energy NIR light can occur safely, the high scattering properties of tissues renders the direct geometric correlation between incident and detected irradiation invalid. The forward imaging problem, (i.e., prediction of the propagation of NIR light through tissues when a map of the tissue optical properties is known) can be described in terms of the diffusion approximation to radiative transfer. The inverse imaging problem (i.e., prediction of the interior optical properties from measurements of light propagation made at the exterior tissue-air interface positions) requires solution of a series of equations that are non-linear in the optical properties to be estimated. In this contribution, we describe a novel algorithm to estimate a solution to the nonlinear, inverse imaging problem for fluorescence frequency-domain photon migration (FDPM). In the following sections of this introduction, we briefly (i) present the background of frequency-domain photon migration (FDPM) imaging, (ii) compare prior work and our current approach towards solution of its inverse imaging problem, and (iii) introduce the concept of fluorescent contrast agents which can accelerate the convergence of the inverse imaging solution.

1.1   *Frequency-domain photon migration: forward and inverse problems*

Frequency-domain photon migration, depends upon launching intensity modulated (30-200 MHz) light at the interface of a highly scattering medium (such as tissue), and detecting the intensity-modulated wave that successfully propagates to the detector located a distance ρ away from the incident source. Depending upon the spatial distribution of interior absorption and scattering optical properties, the detected light is both phase-delayed by θ, and amplitude attenuated by factor M when compared to the incident light (see Figure 1). The solution to the forward imaging problem involves predicting the phase-delay, θ, and amplitude demodulation, M as a function of angular modulation frequency, ω, and position, r, along the tissue surface given a known spatial distribution of absorption and scattering optical properties. The absorption coefficient, μ_{a_x}, representing the inverse mean absorption path and the isotropic scattering coefficient, μ'_{s_x}, equivalent to the inverse isotopic scattering length, govern the propagation of light through scattering media, such as tissues. Since near-infrared light is multiply scattered in tissues, the numerical solution to the diffusion approximation of the radiative transfer equation provides solution to the forward biomedical optical imaging problem. For a propagating intensity modulated wave of light, the optical diffusion equation is written as

$$-\nabla \cdot \left[D_x(\bar{r}) \nabla \Phi_x(\bar{r},\omega) \right] + \left[\frac{i\omega}{c} + \mu_{a_{xi}}(\bar{r}) + \mu_{a_{xf}}(\bar{r}) \right] \Phi_x(\bar{r},\omega) = 0 \qquad on\ \Omega \quad (1)$$

where Φ_x represents the complex number describing the scalar flux of photons at position r; ω is the modulation frequency; c is the speed of light within the medium; $\mu_{a_{xi}}$ is the absorption due to chromophores and $\mu_{a_{xf}}$ is the absorption due to fluorophores $(\mu_{a_x} = \mu_{a_{xi}} + \mu_{a_{xf}})$. D_x is an optical diffusion coefficient equivalent to $1/[3(\mu_{a_x} + \mu'_{s_x})]$. From numerical solution of Eqn (1) with a Robin boundary condition, the complex scalar flux at the surface, $\Phi_x(=Me^{i\theta})$, and the phase delay, θ, and amplitude attenuation, M, can be

determined. It is important to note that the diffusion equation applies when $\mu_{a_x} \ll \mu'_{s_x}$ and D_x is approximated by $1/\left[3\left(\mu'_{s_x}\right)\right]$.
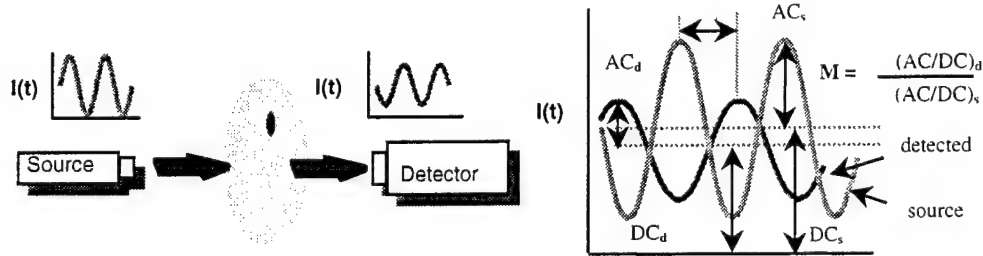

Figure 1 Schematic of fluorescence photon migration.

The successful implementation of biomedical optical imaging involves the effective solution of the inverse imaging problem, i.e., determining the interior optical property map of absorption and scattering given measurements of θ and M along the tissue surface. To date, approaches have focused upon the *linearization* of the problem using first order Born or Rytov approximations [1, 2]. Non-linear optimization employing iterative Born [3, 4], or distorted Born methods [3,5] require accurate information regarding the normal "background" optical properties which the tissue "heterogeneity" resides. Since the normal tissue background optical properties can be expected to vary greatly, this *a priori* information is not realistically feasible for biomedical optical imaging.

Other investigators have used the modified Newton-Raphson method with the Levenberg-Marquardt regularization as the central inversion step [6, 7, 8 and 9]. While not requiring accurate "background" optical properties for initial parameter estimate guesses for successful reconstruction, the Newton-Raphson with Levenberg-Marquardt regularization has three distinct disadvantages for biomedical optical imaging. The first disadvantage is that the full Hessian matrix is not fully considered making the method inefficient for highly non-linear problems such as optical imaging. Numerical experiments by McKeown [10] and Veapucci [111] have shown that while the Gauss-Newton and Levenberg-Marquardt methods solve nonlinear least squares problems efficiently when the residuals are small or zero at the solution, these methods are less efficient than the quasi-Newton method when the residuals are significantly nonlinear. Meyer [12] provides theoretical support of this observation. In the work presented herein, we demonstrate the use of a truncated Newton method with trust region for the efficient solution of the large scale, non-linear optical imaging problem. The second disadvantage to Newton-Raphson approaches is that the methods require expensive numerical calculation of the Jacobian that can be subject to error. In this work, we adapt modifications of the reverse automatic differentiation to compute the gradient defining the search direction efficiently and without numerical error [13, 14]. Finally, the Levenberg-Marquardt method requires storage of the full Jacobian matrix, which represents a limitation for optical imaging in three dimensions and when the number of unknowns increases. Since the truncated Newton method requires only the product of the Hessian with the direction at any point, the method is comparatively more efficient for large problems. Our inversion strategy is presented in its entirety in Section 3.

While the difficulties associated with the nonlinear and large scale of inverse imaging problem can be addressed with our inversion strategy, additional significant challenges exist when attempting to reconstruct absorption and scattering properties that are

physiologically feasible. In a study involving actual optical property measurements of normal and diseased tissues, Troy *et al.* [15] found that the optical properties of absorption and isotropic scattering of normal and diseased breast tissues, for example, may not provide sufficient contrast for successful image reconstruction. Indeed, the small influence of "heterogeneity" absorption and scattering on FDPM measurements measured at the boundary can often be within or close to the measurement error of 1 degree in phase and 1% in amplitude attenuation.

1.2 *Fluorescence frequency-domain photon migration: forward and inverse problems*

In order to over come the difficulties associated with insufficient contrast and costly non-linear optimization, we and other investigators have developed fluorescence FDPM imaging approaches and inversion strategies [8, 16, 17, 18]. Fluorescence FDPM physically depends upon the administration of a fluorescent contrast agent, or another agent or gene vector, which results in the expression of a fluorescent protein that emits in the near-infrared wavelength regime. When activated by the absorption of an intensity modulated wave, $\Phi_x(\mathbf{r}, \omega)$, an intensity modulated fluorescent wave, $\Phi_m(\mathbf{r}, \omega)$, is generated at the same modulation frequency, but is amplitude attenuated and phase-delayed relative to the activating excitation wave. The phase-delay, θ_m, and amplitude attenuation, M_m, of the generated fluorescent wave can be as high as 90 degrees and a factor of 10's –100's of the incident excitation wave owing to the fluorescence properties (lifetime and quantum efficiency) of the dye. Specifically, as the biochemical environment of the fluorophore changes, its lifetime. τ (i.e., the lifetime of the activated fluorophore, or the mean time between absorption of excitation and release of fluorescent light) also alters, providing discrimination of diseased tissues possibly on the basis of biochemical environment. The detected intensity modulated fluorescence wave that has been generated within and which has propagated to the tissue boundary possesses a phase-delay, θ_m, and amplitude attenuation, M_m, that is exquisitely more sensitive to embedded "heterogeneities" than possible with absorption FDPM imaging described above [16].

Predictions of fluorescence FDPM measurements of phase-delay, θ_m, and amplitude attenuation, M_m, are achieved through the solution of the complex fluorescence fluence, $\Phi_m(\mathbf{r}, \omega)$, at the boundary from the fluorescence optical diffusion equation:

$$-\nabla \cdot [D_m(\bar{\mathbf{r}})\nabla\Phi_m(\bar{\mathbf{r}}, \omega)] + \left[\frac{i\omega}{c} + \mu_{a_m}(\bar{\mathbf{r}})\right]\Phi_m(\bar{\mathbf{r}}, \omega) = \phi\mu_{a_{x\to m}}\frac{1}{1 - i\omega\tau}\Phi_x(\bar{\mathbf{r}}, \omega) \quad on \ \Omega$$

(2)

where D_m is the optical diffusion equation at the emission wavelength $\left(= 1/3[\mu_{a_m} + \mu'_{s_m}]\right) \approx 1/3[\mu'_{s_m}]$; μ_{a_m} and μ'_{s_m} are the absorption and isotropic scattering coefficients at the fluorescent wavelength; and the right hand term describes the generation of fluorescence within the medium. The term ϕ represents the quantum efficiency of the fluorescence process and the absorption owing to fluorophore is represented by the coefficient $\mu_{a_{x\to m}}$. Here we consider first order relaxation decays only. Note that the source term requires coupling with the solution of excitation fluence described by Eqn (1), where by the absorption coefficient at the excitation light, μ_{a_x} is now provided by the naturally occurring, non-fluorescent chromophores, $\mu_{a_{xi}}$. and the fluorescent contrast agent, $\mu_{a_{x\to m}}$. The numerical solution for the excitation fluence distribution Eqn (1) with the Robin boundary

condition enables prediction of Φ_m from Eqn (2) at the medium boundary and determination of θ_m and M_m. It is important to note that the diffusion equation applies when $\mu_{a_m} << \mu'_{s_m}$.

With the added unknowns at the emission wavelength, the disadvantages using Newton-Raphson optimization for fluorescence FDPM imaging may become more severe. Paithankar *et al.*, [8] and Troy and Sevick-Muraca [19] employed Newton-Raphson, multi-grid finite difference reconstructions of $\mu_{a_{x \to m}}$ τ, and $\phi \mu_{a_{x \to m}}$, given correct priors on other optical properties. Recently, Jiang [20] performed similar work, employing dual meshing finite element methods instead of finite difference methods. Both Paithankar *et al.* [8] and Jiang [20] resorted to removal of "spurious" optical property values or "filtering" using empirically chosen parameters to achieve the "correct" image distorted through inefficient numerical computation of the Jacobian. O'Leary *et al.*, [17] and Chang, *et al.*, [18] employed Born and iterative Born which again not only required known "background" optical properties, but which also was unable to handle fluorescence in the "background." Later Chang *et al.*, [21] demonstrated the ability to reconstruct fluorescence lifetime under conditions of "imperfect" uptake given the spatial distribution of absorption owing to fluorophore; and Lee and Sevick-Muraca [22] employed an iterative Born-type solution of simultaneous absorption and lifetime from fluorescence FDPM synthetic data.

1.3 *Fluorescence FDPM imaging: current work*

In this contribution, we also focus upon fluorescence FDPM imaging, owing to the significant influence of interior fluorescent heterogeneities on measured signals at the medium boundary and adapt our inversion strategy for the non-linear, large scale optimization required for biomedical optical imaging of absorption and fluorescence lifetime. In the following section, the numerical methodology for solving the FDPM forward imaging problem and the simulator used for generation of synthetic data sets for testing our inversion algorithm are presented. Section 3 describes our formulation of the inverse imaging problem as an optimization problem using truncated Newton's methods with trust region and the reverse automatic differentiation in order to reduce the computational overhead associated with optimization. The performance of our algorithm using synthetic data sets is presented in Section 4 and the conclusions, prognosis for FDPM imaging and ongoing work are summarized in Section 5.

2.0 Model prediction of FDPM

2.1 *Boundary conditions for FDPM forward simulator*

Prediction of FDPM measurements on surface $d\Omega$ resulting from diffusion of intensity-modulated waves within volume Ω. is accomplished from solution of Eqn (1) and (2) using the Robin boundary condition. We employ the Robin boundary condition of the form given by Ishimaru[23, 24]:

$$\Phi_x(\bar{r}, \omega) - 2\gamma D_x(\bar{r})\frac{\partial \Phi_x(\bar{r}, \omega)}{\partial n} + S\delta(\bar{r} - \bar{r}_s) = 0 \qquad \text{on} \quad d\Omega \qquad (3)$$

Where S is the complex flux density associated with a point source of excitation light located at r_s on $d\Omega$; n is the unit vector normal to the surface, and γ accounts for refractive index mismatch at the boundary which through Snell's reflection, results in internal reflection at the surface.

Groenhuis et al. [25] have developed an empirical approach to determine the value of the parameter γ, viz.

$$\gamma = (1 + r_d)/(1 - r_d) \tag{4}$$

where

$$r_d = -1.44n_{rel}^{-2} + 0.72n_{rel}^{-1} + 0.668 + 0.063n_{rel} \tag{5}$$

n_{rel} is the relative index of refraction of the scattering medium with respect to the surrounding medium.

2.2 *Galerkin finite element formulation for solution of* Φ_x

We employ the Robin boundary condition in our numerical solution of $\Phi_{x,m}$ employing the Galerkin finite element model with linear triangular elements. In our formulation, we assume $\mu_{a_{x,m}} \ll \mu_{s_{x,m}}$, so that $D_{x,m} \approx 1/3\mu_{s_{x,m}}$. The formulation of the Galerkin finite element solution of Φ_x begins by multiplying Eqn (1) by a weighting function, w_j, and integrating over the domain of interest:

$$\int_{\Omega}\left[-\nabla\cdot(D_x\nabla\Phi_x) + \left(\frac{i\omega}{c} + \mu_{a_{xi}} + \mu_{a_{xf}}\right)\Phi_x\right]w_j\, d\Omega = 0 \quad j=1,2,\ldots,N \tag{6}$$

where $w_j\ \{w_j : j = 1,\cdots,N\}$ is a set of linearly independent weighting functions. N is the number of unknowns.

Using Green's theorem, equation (6) becomes

$$\int_{\Omega}\left[D_x(\nabla\Phi_x)\cdot(\nabla w_j) + \left(\frac{i\omega}{c} + \mu_{a_{xi}} + \mu_{a_{xf}}\right)\Phi_x w_j\right]d\Omega - \int_{\Gamma}D_x w_j\frac{\partial\Phi_x}{\partial n}d\Gamma = 0 \tag{7}$$

where the second term is a line integral along the external boundary and w_j is assumed to be continuous over the whole domain. Now introducing equation (3) in the line integral

$$\int_{\Gamma}D_x w_j\frac{\partial\Phi_x}{\partial n}d\Gamma = \frac{1}{\gamma}\int_{\Gamma}(\Phi_x + S)w_j d\Gamma = \frac{1}{\gamma}\int_{\Gamma}\Phi_x w_j d\Gamma + \frac{1}{\gamma}\int_{\Gamma}Sw_j d\Gamma \tag{8}$$

Upon combing Eqns (8) and (7), once can write

$$\int_{\Omega}\left[D_x(\nabla\Phi_x)(\nabla w_j) + \left(\frac{i\omega}{c} + \mu_{a_{xi}} + \mu_{a_{xf}}\right)\Phi_x w_j\right]d\Omega - \frac{1}{\gamma}\int_{\Gamma}\Phi_x w_j d\Gamma = \frac{1}{\gamma}\int_{\Gamma}Sw_j d\Gamma \tag{9}$$

Suppose that the solution domain Ω is divided into M_1 triangular elements. Now we can obtain the element equation from Eqn (9) as follows:

$$\sum_{el=1}^{M}\left[\int_{\Omega^{el}}\left[D_x^{el}\left(\nabla\Phi_x^{el}\right)\left(\nabla w_j\right)+\left(\frac{i\omega}{c}+\mu_{a_{xi}}+\mu_{a_{xf}}^{el}\right)\Phi_x^{el}w_j\right]d\Omega+\frac{1}{\gamma}\int_{\Gamma^{el}}\Phi_x^{el}w_j d\Gamma\right]=$$

$$\sum_{el}^{M}\left[\frac{1}{\gamma}\int_{\Gamma^{el}}S\,w_j d\Gamma\right]$$

(10)

Assuming that Φ_x^{el},D_x^{el} and $\mu_{a_{xf}}^{el}$ vary linearly within each triangular element el and $\mu_{a_{xi}}$ is constant, we may then write Φ_x^{el},D_x^{el} and $\mu_{a_{xf}}^{el}$ for each element as:

$$\Phi_x^{el}=\sum_{j=1}^{3}L_j\left(\Phi_x\right)_j$$

(11)

where the L_i are the natural co-ordinates for the triangle [26]. According to the Bubnov-Galerkin method, the weighting functions are chosen to be the same as the approximation functions used to represent Φ_x^{el}, that is,

$$w_j=L_j\ for\ j=1,2,...,N$$

The equation (10) can be written as:

$$\sum_{el=1}^{M}\left[\int_{\Omega^{el}}\left[D_x^{el}\left(\frac{\partial\Phi_x^{el}}{\partial x}\frac{\partial L_j}{\partial x}+\frac{\partial\Phi_x^{el}}{\partial y}\frac{\partial L_j}{\partial y}\right)+\left(\frac{i\omega}{c}+\mu_{a_{xi}}+\mu_{a_{xf}}^{el}\right)L_j\right]\Phi_x^{el}d\Omega+\frac{1}{\gamma}\int_{\Gamma^{el}}\Phi_x^{el}L_j d\Gamma\right]=$$

$$\sum_{el=1}^{M}\left[\frac{1}{\gamma}\int_{\Gamma^{el}}S\,L_j d\Gamma\right]$$

(12)

After integration of Eqn (12) and rearrangement, the resulting element stiffness equations become:

$$\sum_{el=1}^{M}\left[\mathbf{K}_1^{el}+\mathbf{K}_2^{el}+\mathbf{K}_3^{el}\right]\Phi_x^{el}=\sum_{el}^{M}\mathbf{r}^{el}$$

(13)

Assembly of these element stiffness matrices $\mathbf{K}_i^{el}$ and local vector $\mathbf{r}^{el}$ yields the system equations $\mathbf{K}\overline{\Phi}_x=\mathbf{b}$ [26].

Since S denotes the complex point source applied to the surface $d\Omega$ at position r_s and S is expressed as:

$$S=S\delta\left(\overline{\mathbf{r}}-\overline{\mathbf{r}}_s\right)$$

(14)

where r_s is the position vector of the point source. By definition, we have

$$\int_{\Gamma^{el}} S\delta(r - r_s)d\Gamma = \begin{cases} S & r_s \in \Gamma^{el} \\ 0 & \text{otherwise} \end{cases} \tag{15}$$

where *el* is the element of the finite element mesh. From Eqn(12) we have

$$r^{el} = \frac{1}{\gamma}\int_{\Gamma^{el}} L_j S\delta(\bar{r} - \bar{r}_s)d\Gamma = \frac{1}{\gamma}L_j(r_s)S$$

If the position r_s of the point source coincides with the position of node j, when $L_j(r_s) = 1$, i.e. we have

$$\left(r^{el}\right)_j = \frac{1}{\gamma}S$$

2.3 *Galerkin formulation of finite element solution of Φ_m*

The forward finite element solution of the emission diffusion equation is formulated similarly to the excitation diffusion equation with the exception that (i) the complex excitation fluence must be first computed, and that (ii) the formulation of fluorescence lifetime poses some additional considerations. As in the formulation of the solution for Φ_x, parameters of $\mu_{a_{x \to m}}$, τ, and D_m are expected to vary linearly within the triangular elements. In order to facilitate the formulation of the Galerkin finite element method, the RHS term of Eqn (2) is expressed in terms of a binomial expansion assuming $\omega\tau < 1$ and higher order terms are neglected. Hence, the RHS source term of Eqn (2) becomes $S_m(\mathbf{r}, \omega) = \phi\mu_{a_{x \to m}}[1 + i\omega(\mathbf{r})\tau]\Phi_x(\mathbf{r}, \omega)$.

This assumption is appropriate, since the phase-delay, θ_m, of the generated fluorescent intensity modulated wave reaches a maximum of 90 degrees with respect the local excitation intensity modulated wave and becomes insensitive to fluorescence lifetime when $\omega\tau > 1$. The formulation of the emission finite element solution for Φ_m is identical to that presented in section 2.2 for Φ_x with the exception that the parameters Φ_m, D_m, $\mu_{a_{x \to m}}$, and τ are assumed to vary linearly within each element. The finite element formulation of emission diffusion is given below:

$$\sum_{el=1}^{M}\left[\int_{\Omega^{el}}\left[D_m^{el}\left(\frac{\partial\Phi_m^{el}}{\partial x}\frac{\partial L_j}{\partial x} + \frac{\partial\Phi_m^{el}}{\partial y}\frac{\partial L_j}{\partial y}\right) + \left(\frac{i\omega}{c} + \mu_{a_m}\right)\Phi_m^{el}L_j\right]d\Omega + \frac{1}{\gamma}\int_{\Gamma^{el}}\Phi_m^{el}L_j d\Gamma\right] =$$
$$\sum_{el=1}^{el}\left[\int_{\Omega^{el}}\Phi_x^{el}\mu_{a_{x \to m}}^{el}\phi\left(1 + \omega\tau^{el}\right)L_j d\Omega\right] \tag{16}$$

It is important to emphasize that the absorption owing to fluorophore is equivalent in our case to $\mu_{a_{x \to m}}$ and to $\mu_{a_{xf}}$. We differentiate between the two parameters when reconstructing absorption from synthetic excitation, $\mu_{a_{xf}}$, and absorption from emission data $\mu_{a_{x \to m}}$.

2.4 Solution of the system of finite element equations

For both excitation and emission finite element formulations, the local stiffness matrices, K_j^{el}, are formed and then combined into a complex, global stiffness matrix, **K**, which depends upon the absorption and scattering properties at each wavelength. For solution of excitation fluence, $\overline{\Phi}_x$, the vector **b** reflects the complex source of excitation light from boundary point sources at positions r_s, while for solution of the emission fluence, $\overline{\Phi}_m$, vector **b** represents the source generated from within volume Ω.

To solve for $\overline{\Phi}_{x,m}$, the complex set of sparse, linear equations generated by the finite element method,

$$K\overline{\Phi}_{x,m} = b \tag{17}$$

are efficiently solved using a subroutines ZGBTRF and ZGBTRS (LAPACK subroutines). ZGBTRF computes a LU factorization of a complex M_2 by N band matrix using partial pivoting with row interchanges. ($M_2 = 2*KL + KU + 1$, KL and KU are the numbers of subdiagonals and superdiagonals within the band of **K,** respectively). ZGBTRS solves a system of linear equations with a general band matrix **K** using the LU factorization computed by ZGBTRF. The main advantage of this method is that once the decomposition is done, the solution vector can be obtained for any number of right hand side vectors. The accuracy of the solution for $\overline{\Phi}_{x,m}$ depends crucially on the mesh size, h, with the accuracy improving with h^2.

3.0 Inverse solution for fluorescence FDPM

The variables in the inverse problems are the absorption coefficients, $\mu_{a_{xf}}$ (for excitation), $\mu_{a_{x \to m}}$ (for emission), and the lifetime τ at each nodal point of a finite element model. If there are N nodal points then the number of measurements must be greater than N. The number of measurements made at N_B boundary nodes for N_s sources, requires that

$$(N_B - 1)N_s \geq N \tag{18}$$

Due to the reciprocality of sources and detectors, i.e., when a detector position is swapped with a source position equivalent measurements are registered, then we require:

$$\frac{(N_B - 1)N_s}{2} \geq N \tag{19}$$

If $l = 1,...,N_s$ denotes the different distribution of source s and $j = 1,...,N_B$ denotes the boundary nodes at which measurements are made, the error function for optimization of absorption and lifetime imaging may be taken as

$$E_{x,m}\left(\mu_{a_{xf}}\right)=\frac{1}{2}\sum_{l=1}^{N_s}\sum_{\substack{j=1\\j\neq l}}^{N_B}\left[\frac{\left(\left(\left(\Phi_{x,m}\right)_l\right)_j\right)_c-\left(\left(\left(\Phi_{x,m}\right)_l\right)_j\right)_{me}}{\left(\left(\left(\Phi_{x,m}\right)_l\right)_j\right)_{me}}\right]\left[\frac{\left(\left(\left(\Phi_{x,m}^*\right)_l\right)_j\right)_c-\left(\left(\left(\Phi_{x,m}^*\right)_l\right)_j\right)_{me}}{\left(\left(\left(\Phi_{x,m}^*\right)_l\right)_j\right)_{me}}\right] \quad (20)$$

The subscript c denotes the values calculated by the forward simulator problem and the subscript me denotes the experimental (or in this case synthetically generated) fluence values. The superscript $*$ denotes the complex conjugate of the complex function $\Phi_{x,m}$. The subscript l and j denote fluence values that arise between source l and detector j.

It is seen from the equation (20) that the calculation of error function E involves N_s solutions of the direct problem. The global stiffness matrix $\mathbf{K}_{x,m}$ for excitation and emission remains constant with only the vector $\mathbf{b}$ changing with each excitation source. Since the global stiffness matrix $\mathbf{K}_x$ depends on $\overline{\mu}_{a_{xf}}$ and $\mathbf{b}$ is independent of $\overline{\mu}_{a_{xf}}$, LU decomposition of $\mathbf{K}_x$ for solution of Φ_x need only be performed once in each iteration of the optimization problem.

An efficient way of calculating $E_{x,m}$ for excitation and emission equations consists of the following steps:

Step 1   Given $\mu_{a_{xf}}$, calculate the local stiffness matrices $\mathbf{K}^{el}\left(\overline{\mu}_{a_{xf}}\right)$

Step 2 $\mathbf{K}=\sum_{el}\mathbf{K}^{el}$ and set $F=0$

Step 3   Decompose $\mathbf{K}$ into the $\mathbf{LU}$ decomposition $\mathbf{LU}=\mathbf{K}$

For each source l
Step 4   calculate $\mathbf{b}(s)$
Step 5   Solve, $\mathbf{LU}\,\overline{\Phi}_{x,m}=\mathbf{b}$ gives $\left(\overline{\Phi}_{x,m}\right)_c$

Step 6 $E_{x,m}=\frac{1}{2}\sum_{j\in d\Omega}\left(\frac{\left(\Phi_{x,m}\right)_c-\left(\Phi_{x,m}\right)_{me}}{\left(\Phi_{x,m}\right)_{me}}\right)_j\left(\frac{\left(\Phi_{x,m}^*\right)_c-\left(\Phi_{x,m}^*\right)_{me}}{\left(\Phi_{x,m}^*\right)_{me}}\right)_j$

Step 7 $F=F+E_{x,m}$

As most of the efficient optimization algorithms, the truncated Newton method requires the function value $E_{x,m}$ and the gradient of the error function, $\nabla E_{x,m}$, in order to efficiently update parameter estimates. The gradients of the error function in Eqn (20) represent the direction in which the error function is increasing/decreasing most rapidly. Since absorption coefficients $\mu_{a_{xf}}$, $\mu_{a_{x\to m}}$ and τ are the unknown parameters, the gradients are obtained by taking partial derivatives of Eqn (20) with respect to $\mu_{a_{xf}}$, $\mu_{a_{x\to m}}$ and τ.

$$\nabla E_x=\frac{\partial E_x}{\left(\partial\mu_{a_{xf}}\right)}=\mathrm{Re}\sum_{j\in d\Omega}\left(\left\langle\left(\frac{\left(\Phi_x^*\right)_c-\left(\Phi_x^*\right)_{me}}{\left(\Phi_x\right)_{me}\left(\Phi_x^*\right)_{me}}\right),\frac{\partial\left(\Phi_x\right)_c}{\left(\partial\mu_{a_{xf}}\right)}\right\rangle\right) \quad (21)$$

$$\nabla E_m = \frac{\partial E_m}{(\partial \tau)} = \mathrm{Re} \sum_{j \in d\Omega} \left(\left\langle \left(\frac{\left(\Phi_m^*\right)_c - \left(\Phi_m^*\right)_{me}}{\left(\Phi_m\right)_{me}\left(\Phi_m^*\right)_{me}} \right), \frac{\partial\left(\Phi_m\right)_c}{(\partial \tau)} \right\rangle \right) \tag{22}$$

$$\nabla E_m' = \frac{\partial E_m}{\left(\partial \mu_{a_{x \to m}}\right)} = \mathrm{Re} \sum_{j \in d\Omega} \left(\left\langle \left(\frac{\left(\Phi_m^*\right)_c - \left(\Phi_m^*\right)_{me}}{\left(\Phi_m\right)_{me}\left(\Phi_m^*\right)_{me}} \right), \frac{\partial\left(\Phi_m\right)_c}{\left(\partial \mu_{a_{x \to m}}\right)} \right\rangle \right) \tag{23}$$

$\langle .,. \rangle$ denotes the inner product of two complex vectors and Re(.) denotes the real part of a complex. number. The gradient of the real valued error function with respect to real valued $\overline{\mu}_{a_{xf}}$, $\overline{\mu}_{a_{x \to m}}$, and τ remains real valued. At minimum these gradients should be zero, so the real part of the gradients are zero. Therefore, we consider only the real part of the gradients. In the following, the optimization strategy using the truncated Newton method with the gradients computed by reverse automatic differentiation is described.

3.1 *Truncated Newton's method as an optimization strategy for FDPM imaging*

The truncated Newton method with trust region is used for non-linear optimization problem. The reader interested in background literature is referred to the references [27, 28].

Newton's method is based upon approximating the function $E_{x,m}\left(\overline{\mu}_{a_k} + \mathbf{d}\right)$ (μ_a denotes $\mu_{a_{xf}}$ {for excitation} or $\mu_{a_{x \to m}}$ {for emission} in this section) at the kth iteration by the quadratic model:

$$E_{x,m}\left(\overline{\mu}_{a_k} + \mathbf{d}\right) = E_{x,m}\left(\overline{\mu}_{a_k}\right) + Q(\mathbf{d})$$

$$Q(\mathbf{d}) = \mathbf{g}_k^T \mathbf{d} + \frac{1}{2}\mathbf{d}^T \mathbf{G}_k \mathbf{d} \tag{24}$$

In these equations $\mathbf{g}_k = g\left(\overline{\mu}_{a_k}\right) = \nabla E_{x,m}\left(\overline{\mu}_{a_k}\right)$ and $\mathbf{G}_k = \nabla^2 E_{x,m}\left(\overline{\mu}_{a_k}\right)$ denote the gradient vector and Hessian matrix, respectively. The Newton direction is obtained from an exact minimum of above equation; i.e. the search direction $\mathbf{d}$ at iteration k is defined by the equation

$$\mathbf{G}_k \mathbf{d} = -\mathbf{g}_k \tag{25}$$

A sequence of approximate solutions of the above equation is generated by the conjugate gradient method until a vector $\mathbf{d}_i$ (see Step 3) is obtained for which the following condition on the relative residual is satisfied as suggested by Dembo and Steihaug [29];

$$\frac{\|\mathbf{r}_i\|}{\|\mathbf{g}_k\|} \leq \min\left(\frac{1}{k}, \|g_k\| \right)$$

where $\mathbf{r}_i = \mathbf{G}_k \mathbf{d}_i + \mathbf{g}_k$. The conjugate gradient iteration is then truncated and $\mathbf{d}_i$ is used as the search direction for the minimization. The relative residual is used as a measure of accuracy and the required level of accuracy improves as the minimization proceeds and as $\left(\overline{\mu}_{a_k}\right)$ approaches a minimum. It is not necessary to compute the Hessian $\mathbf{G}$ as only the product $\mathbf{Gd}$ is required. The product is calculated using the finite difference formula given below:

$$G(x)d = \frac{1}{\sigma}[g(x + \sigma d) - g(x)] \tag{26}$$

where $\sigma = \dfrac{\sqrt{machine\ precision}}{\|d\|}$. This avoids the calculation and storage of the Hessian but requires an additional gradient evaluation for each minor iteration. The pseudo codes for truncated Newton optimization is as follows:

Step 1   Initialization
An initial guess $\left(\overline{\mu}_{a_0}\right)$ is made of the solution: The radius $R_1 = 0.01$ of the trust region is defined around $\left(\overline{\mu}_{a_0}\right)$, $E_0 = E\left(\overline{\mu}_{a_0}\right)$, $\mathbf{g}_0 = \mathbf{g}\left(\overline{\mu}_{a_0}\right)$ are computed.

Step 2   Stopping Criteria
If $\|\mathbf{g}_k\| \le \varepsilon$ exit, ε is specified by the user
Else continue with next Step 3

Step 3   Computing Newton Direction
Apply conjugate gradient method to find an approximate solution $\mathbf{d}_k$ of the Newton equation $\mathbf{G}_k \mathbf{d}_k = -\mathbf{g}_k$ such that $\|\mathbf{d}_k\| \le R_k$ and $\mathbf{d}_k^T \mathbf{g}_k \le -\varepsilon_1 \|\mathbf{d}_k\| \|\mathbf{g}_k\|$, typically $\varepsilon_1 = 0.001$ [30]. The conjugate gradient algorithm ensures that at the j-th iteration $\mathbf{d}_{j+1} = \mathbf{d}_j + \alpha_j \mathbf{p}_j$ remains within the trust region (α_j = steplength and p_j is the conjugate direction)

Step 4   Line Search
After computing the truncated Newton direction $\mathbf{d}_k$, a line search is used to find an appropriate λ_k that reduces the function $E_{x,m}$ along the line $\overline{\mu}_{a_k} + \lambda_k \mathbf{d}_k$. The Armijo line search [31] is used. It calculates λ_k such that Wolfe's [32] conditions 2 and 3 are satisfied.
Condition 2:
$E(\overline{\mu}_a + \alpha \mathbf{d}) - E(\overline{\mu}_a) \le \varepsilon_2 \alpha \mathbf{d}^T \mathbf{g}$ where ε_2 is a constant, such that $0.5 > \varepsilon_2 > 0$ (typically $\varepsilon_2 = 0.1$).

Condition 3
$E(\overline{\mu}_a + 2\alpha \mathbf{d}) > E\left(\overline{\mu}_a + 2\varepsilon_3 \alpha \mathbf{d}^T \mathbf{g}\right)$ where ε_3 is a constant such that $0.5 > \varepsilon_3 > 0$

Step 5   New Approximation
Compute $\overline{\mu}_{a_{k+1}} = \overline{\mu}_{a_k} + \lambda_k \mathbf{d}_k$, $E_{x,m_{k+1}}$, $\mathbf{g}_{k+1}$

Step 6   Update the trust region
Once λ_k has been found the radius of the trust region R_{k+1} is altered as follows:

$$R_1 = 0.01$$

$$R_{k+1} = 2R_k \quad if \ \lambda_k \ \geq 1.0$$

$$R_{k+1} = \frac{1}{3}R_k \quad if \ \lambda_k \ < 1.0$$

The truncated Newton search direction is constructed so that it always satisfies Wolfe's condition 1 (Step 3, $\mathbf{d}_k^T \mathbf{g}_k \leq -\varepsilon_1 \|\mathbf{d}_k\| \|\mathbf{g}_k\|$). Wolfe's conditions 2 and 3 are satisfied within the line search, as discussed is Step 4. Since all the Wolfe's conditions have been satisfied, the method is globally convergent, and will terminate in a finite number of iterations.

A similar formula applies for lifetime τ and absorption coefficient $\mu_{a_{x \to m}}$.

3.2 Reverse automatic differentiation for computation of $\nabla E_{x,m}$

The reverse automatic differentiation (RAD) method is used to calculate the gradient $\mathbf{g} = g\left(\overline{\mu}_a \ or \ \overline{\tau} \ or \ \overline{\mu}_{a_{x \to m}}\right)$. The reader interested in background literature is referred to References [28, 33, and 34]. A brief description of the reverse differentiation and analytic implementation of this method is discussed in the following section.

Reverse automatic differentiation is discussed in terms of the Wengert [35] list. This list decomposes complicated function of many variables into a sequence of simpler functions of one or two variables. Functions of two variables are called the "binary function". Binary functions are either addition, or subtraction or multiplication. Functions of one variable are either reciprocation, raise of power, exponential, logarithm, trigonometric, or hyperbolic. These functions are defined as unary functions.

If $f(x)$ is a function of the n variables $x_1,...,x_n$ then a set of new variables $x_{n+1},...x_P$ are introduced, where P is the number of arithmetic operations involved in calculating the function $f(x)$. A Wengert list for the calculation for the calculation of $f(x)$ consists of a list of these unary and binary function processed in a given order;

Given	$x_i, \quad i = 1,...,n$
For	$i = n+1,...,P$
then if F_i is binary	$x_i = F_i(x_j, x_k), \quad j, k < i$
and if F_i is unary	$x_i = F(x_j). \quad j < i$
	$f(x) = x_{n+P}$

Reverse differentiation can be explained as follows. Given the Wengert list for the calculation of f, a set of adjoint variables $\hat{x}_i = \partial f / \partial x_i$ is introduced and the order of the operations reversed. The method is based on the function of a function rule of calculus that implies

$$\frac{\partial f}{\partial x_i} = \sum_j \frac{\partial f}{\partial x_j} \frac{\partial F_j}{\partial x_i} \quad j > i$$

The automatic method involves a pass in the reverse direction through the list after the function has been evaluated in a forward sweep. Hence the method is:

Given $\quad x_i, \quad i = 1,...,P$

set $\qquad \hat{x}_i = 0, \quad i = 1,...,n+P-1 \quad and \quad \hat{x}_{n+P} = 1$

for $\qquad i = n+P,...,n+1$

then, if F_i is binary, $\qquad \hat{x}_j = \hat{x}_j + \hat{x}_i \dfrac{\partial F_i}{\partial x_j} \quad i > j$

and $\qquad\qquad\qquad\qquad \hat{x}_k = \hat{x}_k + \hat{x}_i \dfrac{\partial F_i}{\partial x_k} \quad i > j$

else if F_i is unary, $\qquad \hat{x}_j = \hat{x}_j + \hat{x}_i \dfrac{\partial F_i}{\partial x_j} \quad i > j$

derivatives $\qquad\qquad g_i = \hat{x}_i \quad i = 1,...,n$

Griewank [14] showed that it is always possible to calculate any gradient vector of a function in less than 3 times the computational cost of the function by the reverse automatic differentiation method irrespective of the dimension of the problem. The main disadvantage of the automatic code is that it requires large storage and significant data accessing overheads [28, 33, and 34]. In order to overcome these difficulties, the reverse differentiation method is extended and has been performed analytically. This does not require large storage and at the same time gradients are calculated in less than three times the operation count of the function.

The gradients of $E_{x,m}$ with respect to parameter μ_{axf} are calculated using the reverse differentiation method as follows.

Step 1 $\qquad F_{x,m} = 0, \quad \hat{\mathbf{K}} = \dfrac{\partial E_{x,m}}{\partial K} = 0, \quad \hat{\mathbf{b}} = \dfrac{\partial E_{x,m}}{\partial b} = 0$

Step 2 $\qquad$ Calculate element matrix $\mathbf{K}^{el}(\overline{\mu}_a)$

Step 3 $\qquad$ Assemble global matrix $\mathbf{K}$

Step 4 $\qquad$ Decompose $\mathbf{K} = \mathbf{LU}$

For each light source s:

Step 5 $\qquad$ Calculate $\mathbf{b}(s)$

Step 6 $\qquad$ Solve $\mathbf{LU}\overline{\Phi}_{x,m} = \mathbf{b}(s)$ to give $\left(\overline{\Phi}_{x,m}\right)_c$

Step 7 $\qquad E_{x,m} = \sum_j \dfrac{1}{2} \left(\dfrac{\left(\Phi_{x,m}\right)_c - \left(\Phi_{x,m}\right)_{me}}{\left(\Phi_{x,m}\right)_{me}} \right)_j \left(\dfrac{\left(\Phi^*_{x,m}\right)_c - \left(\Phi^*_{x,m}\right)_{me}}{\left(\Phi^*_{x,m}\right)_{me}} \right)_j$

Step 8 $\qquad F_{x,m} = F_{x,m} + E_{x,m}$

Step 9 $\qquad \hat{\overline{\Phi}}_{x,m} = \dfrac{\partial E_{x,m}}{\partial \Phi_{x,m}} = \begin{cases} \left(\dfrac{\left(\Phi^*_{x,m}\right)_c - \left(\Phi^*_{x,m}\right)_{me}}{\left(\Phi_{x,m}\right)_{me}\left(\Phi^*_{x,m}\right)_{me}} \right)_j & for\,all\ j \in d\Omega \\ 0 & for\,all\ j \notin d\Omega \end{cases}$

Step 10 Solve $\mathbf{LU}\overline{v}_{x,m} = \hat{\overline{\Phi}}_{x,m}$

Step 11 Update $\hat{\mathbf{K}} = \hat{\mathbf{K}} - \overline{v}^T_{x,m}\overline{\Phi}_{x,m}, \quad \hat{\mathbf{b}} = \hat{\mathbf{b}} + \overline{v}_{x,m}$

$$\left(\hat{\mu}_{a_{xf}}\right)_p = \frac{\partial E_{x,m}}{\partial\left(\mu_{a_{xf}}\right)_p} = \frac{\partial E_{x,m}}{\partial K}\frac{\partial K}{\partial\left(\mu_{a_{xf}}\right)_p} + \frac{\partial E_{x,m}}{\partial b}\frac{\partial b}{\partial\left(\mu_{a_{xf}}\right)_p}$$

Step 12

$$= \sum_{el}\sum_{i,j}\left(\hat{K}^{el}\right)_{i,j}\left(\frac{\partial K_{i,j}^{el}}{\partial\left(\mu_{a_{xf}}\right)_p}\right) + \sum_{el}\sum_{j}\hat{b}_j\frac{\partial b_j}{\partial\left(\mu_{a_{xf}}\right)_p}$$

The above gradients of error function $E_{x,m}$ are calculated using the global stiffness matrices, **K,** and the matrix **b** assembled from the excitation and emission diffusion equations as described in Section 2.2 and 2.3. (The reverse differentiation method described above uses the fact that if $\Phi_{x,m}$ is the solution of the equation $K\overline{\Phi}_{x,m} = \mathbf{b}$ then $\hat{K} = -\overline{v}^T_{x,m}\overline{\Phi}_{x,m}$ and $\mathbf{b} = \overline{v}_{x,m}$ where $\overline{v}_{x,m}$ is the solution of the equation $K\overline{v}_{x,m} = \hat{\overline{\Phi}}_{x,m}$, see Appendix A). With $\nabla E_{x,m}$ and $E_{x,m}$ computed, the Newton directions can be computed as described in Section 3.1. Similar formulas hold for $\hat{\tau}$ and $\hat{\mu}_{a_{x\to m}}$.

4   Conclusions

We have formulated the solution to the absorption and fluorescence FDPM optical imaging problem as a non-linear optimization scheme. We develop the truncated Newton method for minimizing the sum of errors between measured and synthetic data generated using a simplistic finite element model with a minimal number of sources and detectors. Since the truncated Newton method requires only the product of the Hessian with a direction at any point, it is computationally efficient for large optimization problems. We couple the truncated Newton method with a finite element solver which assumes a polynomial series in absorption and lifetime in order to accurately compute $\Phi_{x,m}$ and employ principles of reverse differentiation in order to efficiently compute the gradient of the error function, $\nabla E_{x,m}$.

Using synthetic data with simulated measurement noise, we demonstrate in Part II the optimization strategy on a series of studies involving a minimum number of sources and detectors.

Appendix A

Calculation of adjoint variables

In this appendix we derive the expressions for the adjoint variables $\hat{K} = \dfrac{\partial E_{x,m}}{\partial K}$ and

$$\hat{\mathbf{b}} = \frac{\partial E_{x,m}}{\partial b}.$$

(i)   Adjoint variable $\hat{\mathbf{K}}$

$$\hat{K} = \frac{\partial E_{x,m}}{\partial K} = \frac{\partial E_{x,m}}{\partial\overline{\Phi}_{x,m}}\frac{\partial\overline{\Phi}_{x,m}}{\partial K} = \hat{\overline{\Phi}}_{x,m}\frac{\partial\overline{\Phi}_{x,m}}{\partial K} = \hat{\overline{\Phi}}_{x,m}\frac{\partial\Phi_{x,m}}{\partial\overline{\mu}_{a_{xf}}}\frac{\partial\overline{\mu}_{a_{xf}}}{\partial K} \qquad (A1)$$

(since K is a function of $\mu_{a_{xf}}$, we differentiate K with respect of $\mu_{a_{xf}}$). Now we use the global equation $\mathbf{K}\overline{\Phi}_{x,m} = \mathbf{b}$ to find $\dfrac{\partial \overline{\mu}_{a_{xf}}}{\partial K}$ as follows:

$$\mathbf{K}\overline{\Phi}_{x,m} = \mathbf{b}$$

$$\frac{\partial K}{\partial \overline{\mu}_{a_{xf}}}\overline{\Phi}_{x,m} + K\frac{\partial \overline{\Phi}_{xf}}{\partial \overline{\mu}_{a_{xf}}} = 0$$

Since the source term b is constant in excitation equation.

$$\frac{\partial K}{\partial \overline{\mu}_{a_{xf}}} = -\frac{K\dfrac{\partial \overline{\Phi}_{x,m}}{\partial \overline{\mu}_{xf}}}{\overline{\Phi}_{x,m}}$$

$$\frac{\partial \overline{\mu}_{xf}}{\partial K} = -K^{-1}\frac{\overline{\Phi}_{x,m}}{\dfrac{\partial \overline{\Phi}_{x,m}}{\partial \overline{\mu}_{a_{x,m}}}} \tag{A2}$$

On substituting Eqn (A2) in Eqn (A1) we have

$$\hat{K} = -\hat{\overline{\Phi}}_{x,m}\ K^{-1}\Phi_{x,m} = -\overline{v}^{T}\overline{\Phi}_{x,m} \tag{A3}$$

where

$$\overline{v} = \hat{\overline{\Phi}}K^{-1}$$

$$\mathbf{K}\overline{v} = \hat{\overline{\Phi}}_{x,m} \tag{A4}$$

We can solve the Eqn(A4) and obtain $\overline{v}$. Finally $\hat{K}$ is obtained using Eqn(A3).

(ii)   Adjoint variable $\hat{b}$

$$\hat{b} = \frac{\partial E_{x,m}}{\partial b} = \frac{\partial E_{x,m}}{\partial \overline{\Phi}_{x,m}}\frac{\partial \overline{\Phi}_{x,m}}{\partial b} = \hat{\overline{\Phi}}_{x,m}\frac{\partial \overline{\Phi}_{x,m}}{\partial b} = \hat{\overline{\Phi}}_{x,m}\frac{\partial \overline{\Phi}_{x,m}}{\partial \overline{\tau}}\frac{\partial \overline{\tau}}{\partial b} \tag{A5}$$

(since b is a function of $\overline{\tau}$, we differentiate b with respect of $\overline{\tau}$). Now we use the global equation $\mathbf{K}\overline{\Phi}_{x,m} = \mathbf{b}$ to find $\dfrac{\partial \overline{\tau}}{\partial b}$ as follows:

$$\mathbf{K}\overline{\Phi}_{x,m} = \mathbf{b}$$

$$\mathbf{K}\frac{\partial \overline{\Phi}_{x,m}}{\partial \overline{\tau}} = \frac{\partial b}{\partial \overline{\tau}}$$

$$\frac{\partial \bar{\tau}}{\partial b} = \mathbf{K}^{-1} \frac{1}{\dfrac{\partial \overline{\Phi}_{x,m}}{\partial \bar{\tau}}} \tag{A6}$$

Substitute Eqn(A6) into Eqn(A5) we have

$$\mathbf{K}\hat{\mathbf{b}} = \hat{\overline{\Phi}}_{x,m} \tag{A7}$$

Eqn(B7) is the same as Eqn (B4). Hence $\hat{\mathbf{b}} = \overline{v}$

Nomenclature

M	amplitude modulation
r	position
c	speed of light
$S(r_{s,\omega})$	source at location r_s and modulated frequency ω.
D	optical diffusion coefficient $= 1/3\left[\mu_a + \mu_s'\right]$
n	normal
r_s	source position
r_d	parameter describing γ
n_{rel}	relative refractive functions
w_j	independent weighting functions
L_j	co-ordinates for triangular elements
$\mathbf{K}_i^{el}$	element stiffness matrices
$\mathbf{r}^{el}$	local vector in FEM stiffness equations
b	local vector in FEM stiffness equation containing source terms
Z	variance
$G(0,1)$	random number with Gaussian distribution of zero mean and unit variance
N	number of nodal points
N_s	number of sources
N_B	number of boundary nodes
ρ	distance between source and detector pair
θ	phase-delay
ω	angular modulation frequency
μ_a	absorption coefficient
μ_s'	isotropic scattering coefficient
Φ	complex fluence
ϕ	quantum efficiency
τ	fluorescence lifetime
Ω	volume
γ	parameter to account for refractive index mismatch
Γ	surface
ε	stopping criteria for truncated Newton's method
E	error function for all sources
F	error function for individual sources
$\mathbf{g}_k$	gradient vector at iteration $k = \nabla E_k$

d   search direction

$\mathbf{G}_k$ Hessian matrix

Truncated Newton's optimization scheme for absorption and fluorescence optical tomography: Part II Reconstruction from synthetic measurements

R. Roy and E. M. Sevick-Muraca

The Photon Migration Laboratory, School of Chemical Engineering,

Purdue University, West Lafayette, IN 47907-1283

ranadhir@ecn.purdue.edu, sevick@ecn.purdue.edu

Abstract: Using two dimensional synthetic frequency-domain measurements, the inverse imaging problem is solved for absorption and fluorescence lifetime mapping with the truncated Newton's optimization scheme developed in Part I of this contribution. Herein, we present reconstructed maps of absorption owing to a fluorophore from excitation and emission measurements which detail the presence of tissue heterogeneities characterized by tenfold increase in fluorescent contrast agent. Our results confirm that fluorescence provides superior mapping of heterogeneities over excitation measurements. Using emission measurements we then map fluorescent lifetime under conditions of tenfold uptake of contrast agent in tissue heterogeneities. The ability to map fluorescent quenching and lengthening of contrast agents facilitates the solution of the inverse problem and further improves the ability to reconstruct tissue heterogeneities.

References:

1 R. Roy and E.M. Sevick-Muraca, "Truncated Newton's optimization scheme for absorption and fluorescence optical tomography: Part I- Theory and formulation," Optics Express, this volume, 1999.

2 T. L. Troy, D. L. Page, and E. M. Sevick-Muraca, "Optical properties of normal and diseased breast tissues: prognosis for optical mammography," J. Biomedical Optics, 1, 342-355, 1996.

3 E. M. Sevick-Muraca, G. Lopez, T. L. Troy, J. S. Reynolds, and C. L. Hutchinson, "Fluorescence and absorption contrast mechanisms for biomedical optical imaging using frequency-domain techniques," Photochemistry and Photobiology, 66: 55-64, 1997.

4 R. Cubeddu, G. Canti, A. Pifferi, P. Taroni, and G. Valentini, "Fluorescence lifetime imaging of experimental tumors in hematoporhyrin derivate-sensitized mice," Photochem. Photobiol. 66, 229-236, 1997.

5 D.Y. Paithankar, A. U. Chen, B.W. Pogue, M. S. Patterson, and E. M. Sevick-Muraca, "Imaging of fluorescent yield and lifetime from multiply scattered light re-emitted from tissues and other random media," Appl. Optics, 36, 2260-2272, 1997. .

6 M. A. O'Leary, D. A. Boas, B. Chance, and A.G. Yodh, "Fluorescence lifetime imaging in turbid media," Opt. Lett. 21, 158-160, 1996.

7 E. M. Sevick-Muraca, C. L. Hutchinson, and D.Y. Paithankar, "Optical Tissue Biodiagnostics Using Fluorescence Lifetime," Optics and Photonics News, 7 פp 25-28, 1996.

8 H. Jiang, "Frequency-domain fluorescent diffusion tomography: a finite-element based algorithm and simulations," Appl. Opt.37, 5337-5343, 1998.

9   M. J. Eppstein, D. E. Dougherty, D. J. Hawrysz, and E. M. Sevick-Muraca, "Three-dimensional optical tomography," Optical Tomography and Spectroscopy of Tissue III, B. Chance. R.R. Alfano, and B.J. Tromberg (eds.), Proc. Soc. Photo-Opt. Instrum. Eng., 3597: 000-000, 1999.

10 M. Schweiger and S. R. Arridge, "Comparison of two- and three- dimensional reconstruction methods in optical tomography," Appl. Opt. 37, 7419-7428, 1998.

11 J. S. Reynolds, T. L. Troy and E. M. Sevick-Muraca, "Multi-pixel techniques for frequency-domain photon migration imaging," Biotech. Prog. 13, 669-680, 1997.

12 Reynolds, J. S., Troy, T. L., Thompson, A., Mayer, R., Thompson, A. B., Waters, D. J., Cornell, K.K., Snyder, P.W., and E. M. Sevick-Muraca, "Multi-pixel frequency-domain of spontaneous canine breast disease using fluorescent agents," Optical Tomography and Spectroscopy of Tissue III, B. Chance, R.R. Alfano, and B.J. Tromberg (eds.), Proc. Soc. Photo-Opt. Instrum. Eng., 3597: 000-000, 1999.

---

1.   Introduction

In Part I of this contribution, we have formulated the absorption and fluorescence inverse imaging problem as an optimization problem in which an interior map of tissue optical properties of absorption and fluorescence lifetime can be reconstructed from excitation and emission frequency-domain photon migration (FDPM) measurements. Since significant challenges for the non-linear and large scale reconstructions are further exaggerated by the physiological low contrast of absorption and scattering property differences between normal and diseased tissues [2], we have focused upon the development of absorption and fluorescence lifetime imaging following the administration of a fluorescent contrast agent. Previously, we have conducted FDPM experimental measurements to show that the FDPM contrast owing to fluorescence exceeds that possible by monitoring absorption with excitation FDPM measurements [3]. One objective of this contribution is to compare the reconstruction of absorption cross section owing to a fluorescent agent, which has a tenfold preferential uptake in the tissue region of interest using excitation and emission FDPM measurements. Secondly, we focus upon the reconstruction of fluorescent lifetime for cases in which a tenfold preferential uptake exists within the tissue volume of interest is accompanied by a shortening and lengthening of a first order fluorescence decay time (or fluorescence lifetime). In the following, we describe the generation of the synthetic data set for input into the optimization scheme, and then the results for absorption and fluorescence lifetime imaging. Finally, we comment on the availability of fluorescent contrast agents for inducing optical contrast and the future work to adapt our inversion strategies to actual FDPM measurements.

2.0 Generation of synthetic data set using forward simulator

In order to test our inversion a truncated Newton's optimization scheme developed in ref. [1], we generated synthetic data of $\Phi_{x,m}$ in a two dimensional, square domain of 4 x 4 cm^2. For the forward simulation, the mesh contained 2209 internal and 192 boundary nodes with 4608 triangular elements. It should be noted that a uniform grid is used in this exercise whereas for future work we adapt a finer grid near the source points where the gradients are very high. Four sources of intensity modulated excitation light were simulated midpoint on each side of the domain with a total of 59 point detectors simulated equidistant along the domain periphery excluding positions occupied by one of the four sources and at each corner of the domain. Predictions of $\Phi_{x,m}$ were made at each detector for each of the four sources, each providing intensity modulation at 50, 100 and 150 MHz with unit depth of modulation and zero phase. For this simulated measurement configuration there were 4 x 59 = 236 simulated observations obtained for reconstruction of interior optical properties at the excitation and emission wavelengths. At the excitation wavelength, "heterogeneities" were to be detected based upon their absorption, and at the emission wavelength, based upon their fluorescence lifetime. **Table I** lists the background and "heterogeneity" optical properties, as well as the location and size of the simulated "heterogeneities" used for the generation of synthetic data

for reconstruction. The simulator was coded in Fortran 77 and took 6 seconds on a SUN Ultrasparc 10 Workstation (200MHz).

Table 1. Parameters used in truncated Newton method optimization for absorption and lifetime imaging

reconstruction variables	background						targets	
	$\mu_{a_{xi}}$ cm^{-1}	$\mu_{a_{xf}}$ or $\mu_{a_{x\to m}}$ cm^{-1}	μ_{s_x} μ_{s_m} cm^{-1}	μ_{a_m} cm^{-1}	τ ns	ϕ	$\mu_{a_{xf}}$ or $\mu_{a_{x\to m}}$ cm^{-1}	τ ns
case I, $\mu_{a_{xf}}$ Figure 1	0.0	0.02	10.0	N/A	N/A	N/A	0.2	N/A
case II, $\mu_{a_{x\to m}}$ Figure 2	0.0	0.02	10.0	0.02	1.0	0.034	0.2	10.0
case III, τ Figures 3 & 4	0.0	0.02	10.0	0.02	1.0	0.034	0.2	10.0
case IV, τ Figures 5 & 6	0.0	0.02	10.0	0.02	10.0	0.034	0.2	1.0

Footnotes: case I- excitation equation is used, emission equation is used for all other cases. In this study, we assume all absorption at the excitation wavelengths is owing to fluorophore.

To mimic measurement error, zero-mean, Gaussian noise corresponding to 1.0% standard error in fluence was added to the synthetic data sets by using the formula:

$$\Phi_x = \Phi''_x(1.0 + Z*G(0,1)) \tag{1}$$

where $G(0,1)$ is a Gaussian distribution with zero mean and unit variance; $Z = 0.01$; and Φ''_x are the simulated data without noise.

To simulate 0.1 degree noise in phase, we compute the error in the final complex fluence, Φ'_x:

$$\tan(\theta + 0.1*G(0,1)) = \frac{img(\Phi^1_x)}{re(\Phi^1_x)}$$

$$\frac{\tan\theta + \tan(0.1*G)}{1 - \tan\theta\tan(0.1*G)} = \frac{img(\Phi^1_x)}{re(\Phi^1_x)}$$

$$\frac{\frac{img(\Phi_x)}{re(\Phi x)} + \tan(0.1*G)}{1 - \frac{img(\Phi_x)}{re(\Phi x)} * \tan(0.1*G)} = \frac{img(\Phi_x^1)}{re(\Phi_x^1)}$$

$$\frac{img(\Phi_x) + re(\Phi_x)*\tan(0.1*G)}{re(\Phi_x) - img(\Phi_x)*\tan(0.1*G)} = \frac{img(\Phi_x^1)}{re(\Phi_x^1)}$$

$$img(\Phi_x^1) = img(\Phi_x) + re(\Phi_x)*\tan(0.1*G)$$

$$re(\Phi_x^1) = re(\Phi_x) - img(\Phi_x) * \tan(0.1*G)$$

Now our new fluence is:
$$\Phi_x' = \left(re(\Phi_x^1), img(\Phi_x^1)\right) \qquad (2)$$

The synthetic fluence for emission is similarly generated and employed as input to the iterative inversion algorithm.

A user specified double precision parameter ε is used as the convergence parameter within the inversion scheme (see section 3.1 of reference [1]). The iterative method is stopped if the length of the gradient vector is less than ε. The final images reported herein are the results of iterations until the length of the gradient $\|g\|$ is less than $\varepsilon = 10^{-9}$, chosen by trial and error.

3.0 Results and discussion

A coarse mesh with 225 internal nodes and 64 boundary nodes (total 289 nodes) is used for the inversion problems, whereas total 2401 nodes with uniform mesh is used for forward problem. Using the synthetic data sets described in Section 2, we demonstrate the truncated Newton method for reconstruction of absorption from excitation and fluorescence FDPM measurements as well as for reconstruction of lifetime from fluorescence FDPM measurements. For this mesh one function $(E_{x,m})$ evaluation took 9.1 seconds and one function and gradient calculation by reverse differentiation took 10.5 seconds.

3.1 *Absorption imaging from synthetic excitation measurements*

As described in Table I, Case I synthetic data set consisted of detecting three "heterogeneities" based upon a ten-fold increase in absorption as might occur upon the administration of a contrast agent. Figure 1(a) illustrates the actual distribution of absorption within the phantom with a background absorption $\mu_{a_{xf}}$ value of 0.02 cm^{-1}. Upon using the background absorption value as an initial starting guess, our attempt to reconstruct the spatial distribution of absorption with simulated measurement with noise was aborted after 25 iterations because the results remain unchanged. The result, illustrated in Figure 1(b), shows that the heterogeneities may be located and differentiated from the relatively uniform background. However, the differentiation of the heterogeneities from one another and the quantitation of their ten-fold increase in absorption are disappointing. The average values of the reconstructed absorption estimate of each of the three "heterogeneities" are plotted as a function of iteration in Figure 1(c). While oscillations in the parameter estimates occur in the initial iterations, the average values appear to smoothly approach an absorption value that underestimates their actual values. These numerical approximation errors may be due to inadequate discretization of the model geometry by the finite element method. Since the
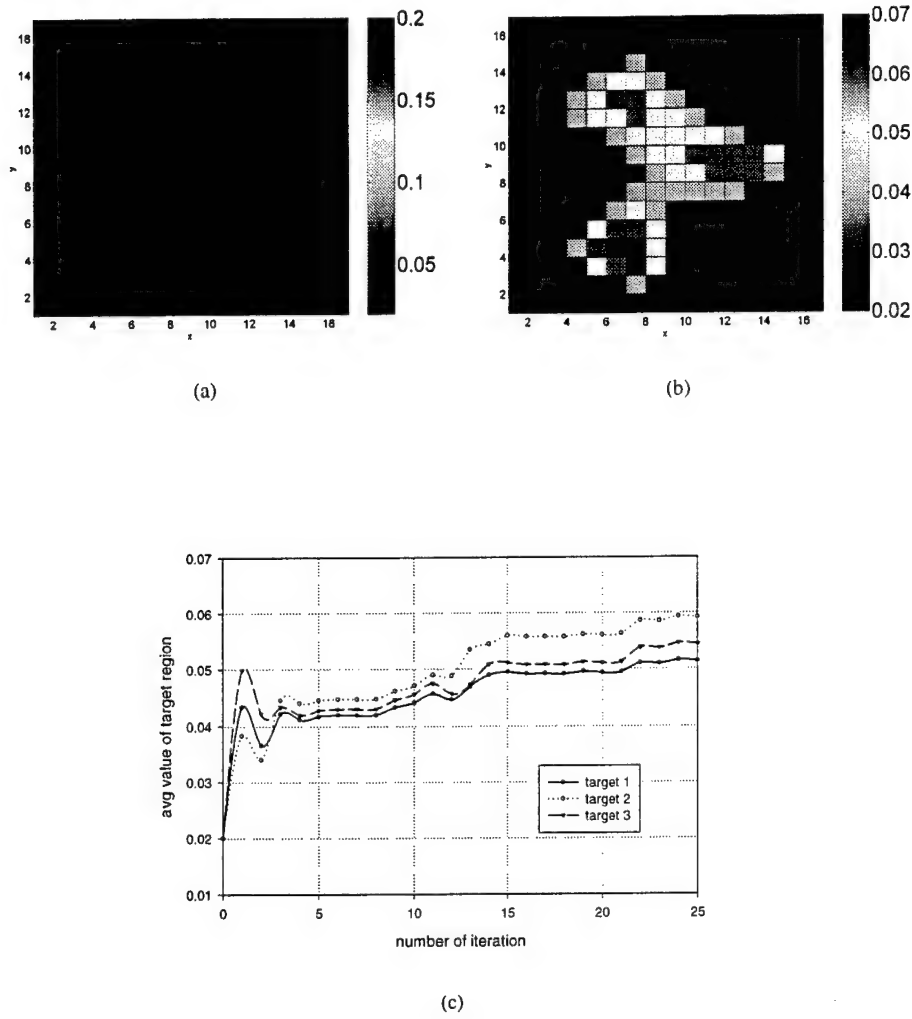
(a)   (b)

(c)

Figure 1 (a) Actual 'true' distribution of absorption, $\mu_{a_{xf}}$ [target 1 top, target 2 right, target 3 bottom] (b) reconstructed $\mu_{a_{xf}}$ from excitation measurement (c) Average value of $\mu_{a_{xf}}$ as a function of iteration

variations of the gradients near the source are very high, in future work we use a finer grid near the boundary. The choice of regularization schemes, finer mesh near the source point and optimal placement of sources and detectors should assist in the convergence.

3.2   Absorption imaging from synthetic fluorescence measurements

As described by Sevick *et al.*[3],reconstruction from excitation measurements is inherently disadvantaged by the small   influence of light-absorbing heterogeneities on the excitation signal measured at the interface. Figure 2 (a) represents the reconstruction of the ten-fold absorption owing to fluorophore in three heterogeneities from
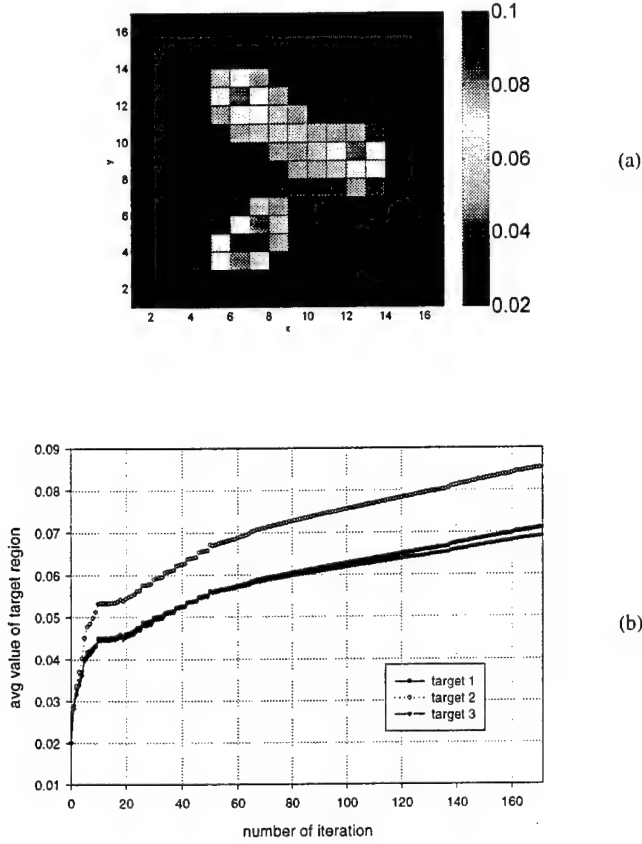
Figure 2 (a) Reconstructed absorption, $\mu_{a_{x \to m}}$, from fluorescence measurements and (b) Average value of $\mu_{a_{x \to m}}$ as a function of iteration.

the synthetic fluorescence FDPM measurements as described by case II in Table I. Figure 2(b) shows the corresponding average values within each of the heterogeneities as a function of iteration. As expected from the superior contrast offered by fluorescence over absorption and the linearity of emission equation (see Eqn (2) of ref [1]), the convergence upon an absorption map from fluorescence measurements occurs faster and more accurately than from excitation measurements. Reconstruction of absorption from excitation requires recalculation of the global matrix at each iteration while the global matrix in absorption or lifetime reconstructions from emission remains unchanged throughout the calculation.

3.3   Lifetime imaging from synthetic fluorescence FDPM measurements

While the contrast owing to absorption may provide localization of tissue disease, the discrimination of diseased tissues based upon changes in lifetime of exogenous fluorescent contrast agents has been demonstrated in endoscopic applications [4] and proposed for optical tomography [5-7]. In the following two studies, we demonstrate the truncated Newton method for demonstrative cases of fluorophore quenching (shortening of fluorophore lifetime) and

enhanced activated fluorophore stability (i.e.. lengthening of fluorophore lifetime) within tissue "heterogeneities."

3.3.1 *Imaging based upon lengthening of fluorophore lifetime*

Figure 3(a) depicts the actual lifetime map of the Case III study listed in Table I in which three heterogeneities with ten-fold uptake of fluorescent dye exhibit a lengthening of lifetime (τ_b=10 ns) within a background which possessed a shorter lifetime (τ_h=1 ns). With an initial starting guess equal to the background lifetime, the reconstructed maps of lifetime are shown for 50MHz (Figure 3(b)); 100 MHz (Figure 3(c)); and 150 MHz (Figure 3(d)). The quality of the reconstruction map seems to improve with increasing modulation frequency and Figure 4(a) through (c) suggests more rapid convergence at increased modulation frequencies. It is noteworthy that using the Levenberg-Marquardt approaches. Paithankar. *et al.* [5] and Jiang [8] report only reconstruction involving fluorophore quenching and were unable to successfully reconstruct heterogeneities with longer lifetimes within a background of short lifetime. Two additional observations of the results can be made:(i) while the recovered values of the absorption from excitation measurements underpredict their local absorption coefficient (0.05 as opposed to 0.20 cm^{-1}), the recovered values of lifetime appear to be closer to the actual values (7 instead of 10 ns); (ii) while the absorption imaging from excitation FDPM measurements (Figure 1) did not achieve convergence after 25 iterations, convergence of fluorescence lifetime imaging was achieved in 20-30 iterations. As described below similar results were obtained for fluorescence lifetime imaging involving fluorophore quenching.
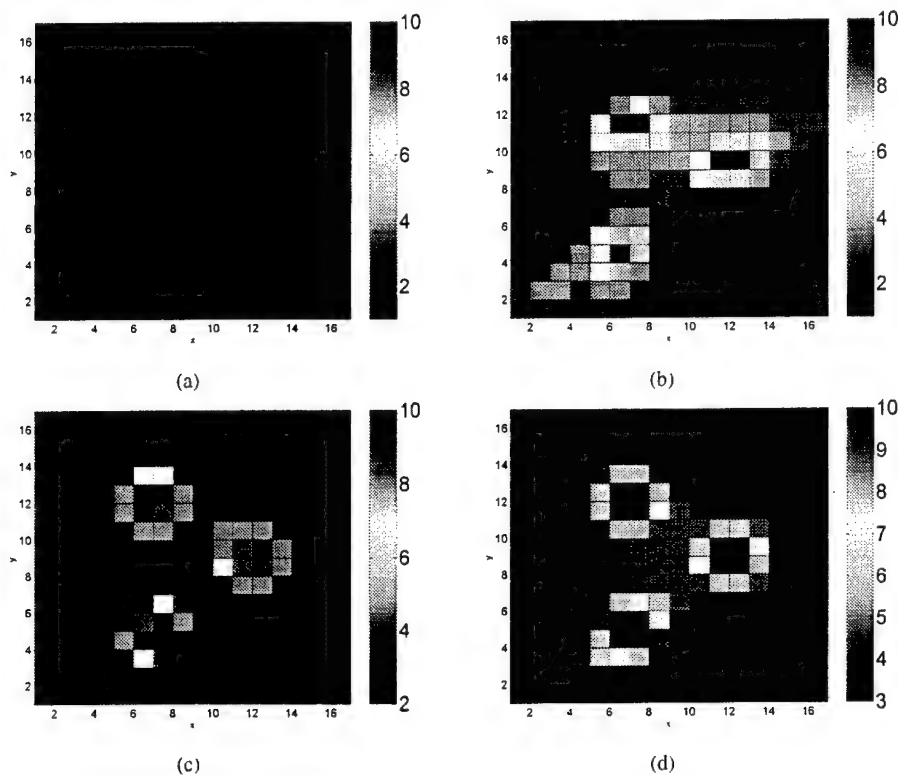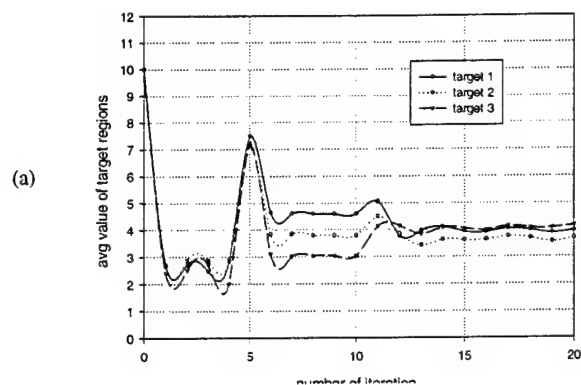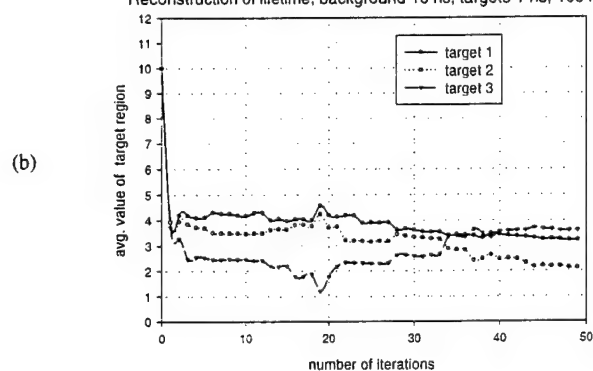

(a)

(b)

(c)

(d)

Figure 3 (a) "True' distribution of fluorophore lifetime, possessing longer lifetime within three heterogeneities having ten-fold uptake of fluorescent dye; (b) Reconstructed lifetime at 50 MHz; (c) 100 MHz; (d) 150 MHz.

Reconstruction of lifetime, background 10 ns, target 1 ns, 50 mhz

(a)

Reconstruction of lifetime, background 10 ns, targets 1 ns, 100 mhz

(b)

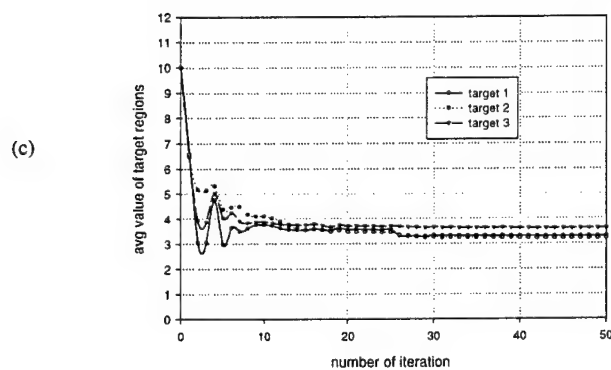Reconstruction of lifetime, background 10 ns, target 1 ns , 150 mhz

(c)

Figure 4 The distribution of fluorophore lifetime, possessing longer fluorescent lifetime within three heterogeneities having ten-fold uptake of fluorescent dye. Average value of heterogeneity lifetime as function of iteration; (b) at 50 MHz; (c) 100 MHz; (d) 150 MHz

3.3.2 *Imaging based upon fluorophore quenching*

Figure 5(a) depicts the actual lifetime map of the Case IV study listed in Table I in which three heterogeneities with ten-fold uptake of fluorescent dye exhibit a shortening of lifetime (τ_b=1 ns) within a background which possessed a longer lifetime (τ_h=10 ns). We assume all other parameters are known. With an initial starting guess equal to the background lifetime, the reconstructed maps of lifetime are shown for 50MHz (Figure 5(b)); 100 MHz (Figure 5(c)); and 150 MHz (Figure 5(d)). The quality of the reconstruction map again seems to improve with increasing modulation frequency and Figures 6(a) through (c) again suggests rapid convergence at increased modulation frequencies and greater efficiency than can be shown with absorption imaging.
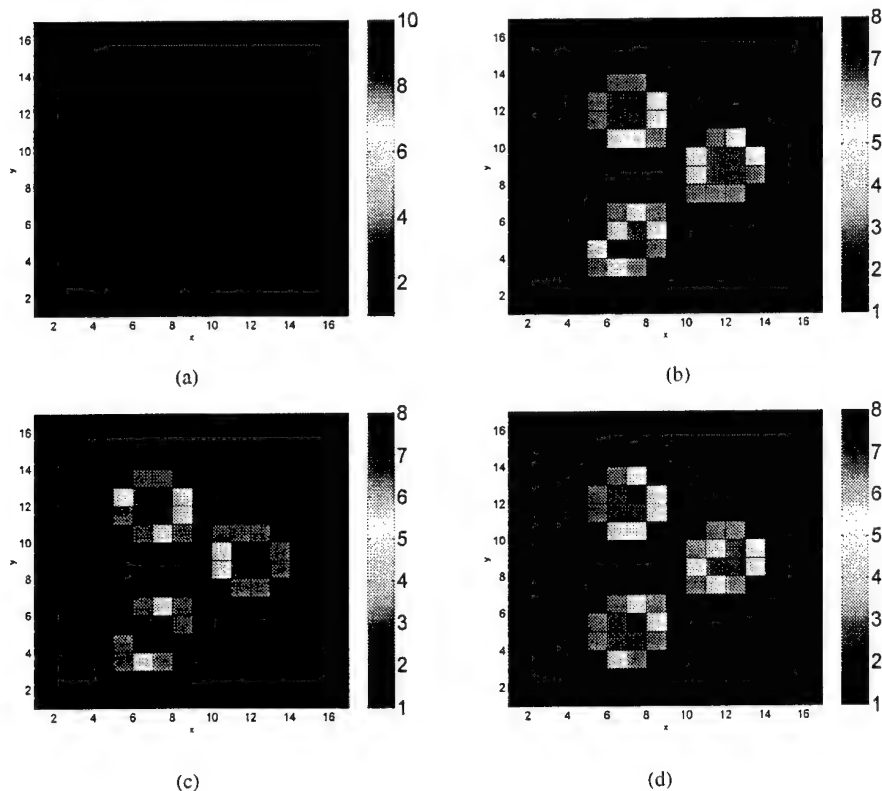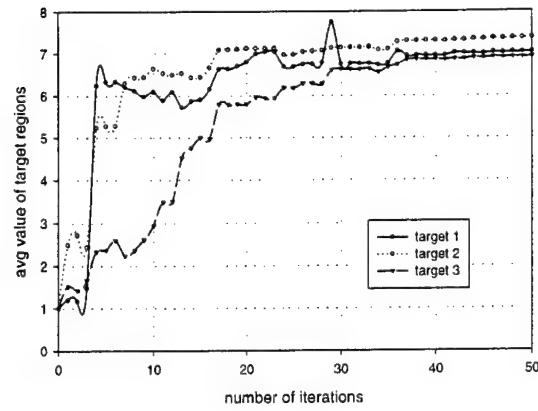

(a)

(b)

(c)

(d)

Figure 5 (a) 'True' distribution of fluorophore lifetime, with fluorophore quenching within three heterogeneities having ten-fold uptake of fluorescent dye; (b) Reconstructed lifetime at 50 MHz; (c) 100MHz; (d) 150 MHz.
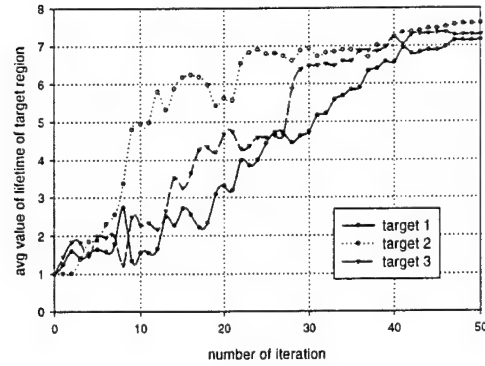
Reconstruction of lifetime, background 1 ns, targets 10 ns, 50Mhz
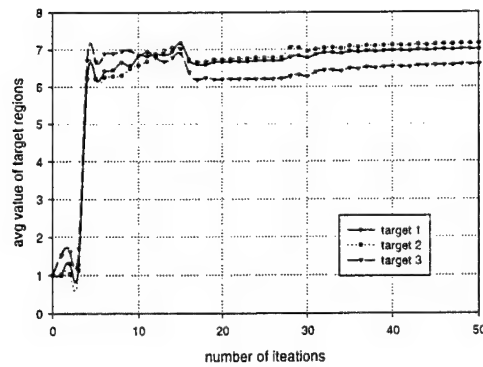
(a)

Reconstruction of lifetime, background 1 ns, targets 10 ns, 100mhz

(b)

Reconstruction of lifetime, background 1 ns, target ns, 150 mhz

(c)

Figure 6 The distribution of fluorophore lifetime, quenching fluorescent lifetime within three hetergeneities having ten-fold uptake of fluorescent dye. Average value of heterogeneity lifetime as function of iteration; (b) at 50 MHz; (c) 100 MHz; (d) 150 MHz

4.0 Conclusions and Future Work

In this contribution, we demonstrate the truncated Newton's optimization scheme for absorption and fluorescence optical tomography. We have presented a method to calculate the gradient of error function based on reverse differentiation method in a finite element method based scheme. This method is programmed by hand so that the overhead problems usually associated with automatic differentiation do not occur. It is shown that a function and the gradient calculations are cheaper than three function evaluations using reverse differentiation. Our work confirms that reconstruction of absorption owing to a contrast agent is enhanced if fluorescence measurements are made over excitation measurements. In addition, the ability to detect heterogeneities with a tenfold uptake of dye that experiences lengthening and shortening of fluorescence lifetime is demonstrated. In practice, FDPM optical tomography must be accomplished with a substantive number of source-detector measurements and for three-dimensional geometries [9,10]. While work continues to develop three-dimensional multi-pixel FDPM measurements [11] using fluorescent contrast agents [12], the development of effective inversion strategies to handle large data sets at minimal computational cost and storage burden is paramount. We believe the continued development of gradient-based optimization schemes, such as presented herein, are necessary for stable recovery of interior optical property maps for medical imaging.

Fluorescence-Enhanced Absorption and Lifetime Imaging

Jangwoen Lee[a] and Eva Sevick-Muraca[b]

[a]School of Electrical and Computer Engineering, Purdue University, West Lafayette. IN. USA

[b]School of Chemical Engineering, Purdue University, West Lafayette. IN. USA

ABSTRACT

Near-infrared biomedical optical imaging consists of imaging interior volumes on the basis of optical property contrast from measurements conducted at the air-tissue interface. However, the ability to optically image or detect diseased tissue volumes located deep within tissues depends upon the contrast provided by differences in absorption and scattering. The exogenous contrast offered by fluorescent contrast agents may be superior to that provided by nonfluorescing, light-absorbing compounds, when the optical measurements are conducted with frequency-domain techniques. However, the reconstruction of internal fluorescent properties of quantum efficiency and lifetime has been difficult, especially when the finite partitioning of fluorescent compounds takes place between normal and diseased tissues. Also, the correct absorption coefficient map is required for the successful reconstruction of lifetime. Herein we present a novel fluorescence-enhanced imaging algorithm for frequency-domain photon migration measurements conducted at the air-tissue interface. Similar to Born iterative image reconstruction techniques. fluorescence-enhanced imaging differs in that it utilizes measurements of generated fluorescent wave instead of scattered excitation wave. Using synthetic data sets, we demonstrate fluorescence-enhanced imaging using FDA approved fluorescent agent. Indocynine Green (ICG). Our results show the fluorescence-enhanced imaging algorithm works well up to 10:1 dye uptake ratio, and it is relatively insensitive to measurement noise. In addition, we present the lifetime reconstruction with a modified fluorescence-enhanced imaging technique.

Keywords: Image reconstruction, Fluorescence, Lifetime

1. INTRODUCTION

Photon migration, or light scattering through turbid media, offers new possibilities for medical applications such as biomedical diagnostics and imaging. In near-infrared (NIR) wavelength range (600 nm - 1300 nm) the absorption of light by endogenous chromophores is relatively low, ranging from $0.1 \sim 1.0 \ cm^{-1}$, while the scattering coefficient is high - typically $100 \sim 1000 \ cm^{-1}$.[1,2] The low absorption properties allow the transmission of measurable amount of visible and near-infrared light deep into the tissue volume. The high tissue scattering, however, reduces the contrast and deteriorates image resolution formed with this light, especially when tissue structures of interest are buried deep within the tissue. The endogenous optical contrast for detection of diseased tissues can be provided by (1) the local absorption coefficient, μ_a, which arises primarily due to hemoglobin and increased vascular volumes associated with tumor angiogenesis,[1] and (2) the isotropic tissue scattering coefficient, μ'_s. The capabilities that improve the detectability of the diseased tissues lie upon (1) the degree of optical contrast, $\Delta\mu_a$ and $\Delta\mu'_s$, or the differences in absorption and scattering properties that must exist between normal and diseased tissue for the effective detection and (2) the successful implementation of image reconstruction algorithms.

In past decade, several investigators have sought ways to reconstruct internal tissue optical properties to differentiate diseased tissues from normal tissues based upon the optical contrast due to absorption and isotropic scattering coefficients.[3-8] However, Troy et al.[9] have shown from their in vitro measurements of breast tissue specimen that the optical contrast due to normal and diseased tissues may not be enough for the successful detection of tumors. The efforts to enhance the optical contrast by the use of exogenous contrast agents such as fluorescent compounds have received more attention recently.[10-12] Sevick et al.[13] showed that the exogenous contrast offered by fluorescent compounds is superior to that provided by nonfluorescing, light-absorbing compounds when time-dependent photon migration measurements are employed. While the preferential uptake of fluorescent contrast agents into disease tissue

Part of the SPIE Conference on Time-Resolved Fluorescence Spectroscopy and Imaging in Tissues
San Jose, California • January 1999 • SPIE Vol. 3600 • 0277-786X/99/$10.00

246

volume of interest is responsible for contrast, the kinetics of fluorescence decay processes can be environmentally specific to tissue volumes and further induce additional optical contrast for the detection.

In this paper, we present a novel fluorescence-enhanced imaging algorithm using frequency-domain photon migration measurements. Using synthetic data sets, we demonstrate the reconstruction of the absorption coefficient due to fluorophores, and simultaneous reconstruction scheme for the absorption coefficient and lifetime. Our results show that the fluorescence-enhanced reconstruction algorithm works works well up to 10:1 uptake ratio. and it is relatively insensitive to measurement noise.

2. OPTICAL CONTRAST

Frequency-domain photon migration imaging consists of launching sinusoidally modulated excitation light at source. location. $\vec{r}_s$, and detecting the wave of excitation and/or emission light at detector position. $\vec{r}_d$. Propagation of the incident excitation wave through the tissue results in a decrease in amplitude, $M(\vec{r}, \omega)$, and an increase in phase shift , $\theta(\vec{r}, \omega)$.

2.1. Contrast due to absorbing heterogeneities

The presence of a light-absorbing heterogeneity results in the reflection of the propagating wave from its position. $\vec{r}_h$. contributing a small, first-order scattered wave, $\Phi^x_{scatt}(\vec{r}_d)$ to the detected signal. The detected wave at the detector position, $\vec{r}_d$, is the sum of the incident wave and the scattered wave, $\Phi^x_{inc}(\vec{r}_d) + \Phi^x_{scatt}(\vec{r}_d)$. If the contrast is defined as the detected signal in the presence of the heterogeneity minus that detected in the absence. the contrast owing to the absorption will be determined by the scattered wave, $\Phi^x_{scatt}(\vec{r}_d)$.

Even with the perfect absorber in the lossless scattering media, the dominant first-order scattered wave. $\Phi^r_{scatt}(\vec{r}_d)$, is small in comparison to the incident wave, $\Phi^x_{inc}(\vec{r}_d)$. Hence the contrast due to the absorbing heterogeneity is expected to be small. As the absorption contrast between the heterogeneity and its surrounding decreases. the magnitude of the scattered wave becomes even smaller. In addition, when the heterogeneity is buried deep within the tissue, the contrast available for the successful image reconstruction will diminish even more and can be lost in the noise of the phase and amplitude measurements.

2.2. Contrast due to uptake of fluorescent dyes

Consider the perfect uptake of fluorescent dye (*i.e.* no exogenous fluorescence attributed to the surroundings) with the assumption that the excitation and emission spectra are well separated. The emission wave generated from the heterogeneity, $\Phi^m_{het}(\vec{r}_d)$ can be detected at the tissue-air interface with an appropriate interference filter. The emission wave generated by the incident excitation wave, $\Phi^x_{inc}(\vec{r}_h)$ is proportional to $[\phi\mu_{ax \to m}\Phi^r_{inc}(\vec{r}_h)]/(1 - i\omega\tau)$, where ϕ is the quantum efficiency of the fluorophore; τ, its lifetime and $\mu_{ax \to m}$, its absorption coefficient owing to the fluorophore. Thus, we can expect that amplitude and the phase lag of the detected emission wave should change according to changes in ϕ, $\mu_{ax \to m}$, and τ. By manipulating ϕ, $\mu_{ax \to m}$, and τ, we could expect the contrast offered by the fluorescence of the heterogeneity to be greater than that offered by its absorbance.

When the finite partitioning of a contrast agent occurs between diseased and normal tissues. the fluorescent signal originated from the surroundings or background has to be accounted for. A series of distributed fluorescent sources also contribute to the resultant phase and amplitude measurements at the detector position and affect the final optical contrast. As the concentration of fluorophore in the surroundings increases, the amplitude modulation of the detected wave increases, and the phase lag will be affected by the strong presence of the fluorophores in surroundings. However, in the presence of a fluorescent dye-laden heterogeneity, a second source of fluorescent generation. $\Phi^m_{het}(\vec{r})$. is set up in coincidence with the location of the heterogeneity, $\vec{r}_h$, within the tissue phantom. In the presence of both heterogeneity and finitely partitioned fluorophores in the surroundings, the detected signal at the detector consists of $\Phi^m_{het}(\vec{r})$ and $\Phi^m_b(\vec{r})$. As in the contrast offered by absorption, the contrast offered by the fluorescence is determined by the size of the contribution of $\Phi^m_{het}(\vec{r})$ relative to $\Phi^m_b(\vec{r})$.

The greater the partitioning of the fluorescent dye within the heterogeneity, the stronger will be its fluorescent source enabling optimal contrast. Fluorescent dyes whose quantum yield and lifetime changes upon the preferential uptake by the diseased tissue can aid contrast. For example, if the dye experiences enhanced and reduced partitioning measured by the ratio of $\mu_{ax \to m}$ of the heterogeneity and its surroundings, the modulation will increase or decrease. respectively. Even if the quantum efficiency, ϕ, and lifetime, τ, do not change in the heterogeneity and in its surroundings, the ratio of $\mu_{ax \to m}$ and the additional phase-shift due to lifetime, τ, will give rise to the larger contrast for measurement at the fluorescent wavelengths than excitation measurements.

3. FORMULATION OF THE INVERSE PROBLEM

In this paper, we consider a simulated infinite homogeneous turbid medium with a spatially uniform distribution of fluorophores in the background. For the purpose of this description, we identify the normal tissues surrounding the diseased tissue by the 'background', while the diseased lesion will be identified as the 'heterogeneity'. Heterogeneities are simulated by regions of increased uptake and changed lifetime. Excitation light is launched at the air-tissue interface and propagates within the phantom. Upon encountering a fluorophore, either in the background or heterogeneity, the excitation photons activate the fluorophore and result in the emission of fluorescent photons which propagate in the media. We assume that the dye's fluorescence and absorption spectra are separated so that we can ignore the possibility of the excitation of fluorophores by the fluorescent reemission. In addition, we ignore the possibility of photo bleaching.

In highly scattering media such as tissues, the propagation of light is well described by the diffusion approximation of the radiative transport equation.[14] The excitation light fluence, $\Phi^x(\vec{r}, \omega)$, or the angle integrated flux of light modulated at angular frequency, ω at position $\vec{r}$ is described by the diffusion equation in the frequency domain for excitation light (superscript x):

$$\nabla \cdot [D^x(\vec{r}) \nabla \Phi^x(\vec{r}, \omega)] + (-\mu_a^x(\vec{r}) + \frac{i\omega}{c})\Phi^x(\vec{r}, \omega) = -S^x(\vec{r}) \tag{1}$$

where $\mu_a^x(\vec{r})$ is the absorption coefficient, $D^x(\vec{r}) = [3 \cdot (\mu_a^x(\vec{r}) + \mu_s'^x(\vec{r})]^{-1}$ is the optical diffusion coefficient, c is the speed of light in the medium. $S^x(\vec{r})$ is the excitation source term, and $\mu_s'^x(\vec{r})$ is the isotropic scattering coefficient. For a point source, $S^x = M^x \delta(\vec{r} - \vec{r_s})$, where M^x is the complex source AC amplitude, and $\vec{r_s}$ is the position of the source.

The complex emission light fluence, $\Phi^m(\vec{r}, \omega)$, is also described by the diffusion equation in the frequency domain. The excitation fluence is coupled with the emission fluence as the source term in the emission diffusion equation. Superscript, m denotes the emission characteristics.

$$
\begin{aligned}
\nabla \cdot [D^m(\vec{r}) \nabla \Phi^m(\vec{r}, \omega)] + \left(-\mu_a^m + \frac{i\omega}{c}\right) \Phi^m(\vec{r}, \omega) &= -S^m(\vec{r}, \omega) \\
&= \frac{-\phi \mu_{ax \to m}}{1 - i\omega\tau(\vec{r})} \Phi^x(\vec{r}, \omega)
\end{aligned}
\tag{2}
$$

where ϕ is the quantum efficiency of the fluorophore, $\mu_{ax \to m}$ is the absorption coefficient due to the fluorophore. $S^m(\vec{r}, \omega)$ is the emission fluence source term, and $D^m(\vec{r})$ is the diffusion coefficient at the emission wavelength, and $\tau(\vec{r})$ is the probe lifetime at position, $\vec{r}$.

Since the emission diffusion equation is an inhomogeneous differential equation, the Green's function is used to obtain the analytical solution of the emission fluence, $\Phi^m(\vec{r})$. The emission fluence, $\Phi^m(\vec{r_d}, \vec{r_s})$, at the detector position, $\vec{r_d}$, and the excitation source position, $\vec{r_s}$, is expressed as follows.

$$
\begin{aligned}
\widetilde{\Phi^m}(\vec{r_d}, \vec{r_s}) &= \int_\Omega G_f(\vec{r_d}, \vec{r'}) S^m(\vec{r'}, \vec{r_s}) \, d\Omega, \quad d\Omega = d\vec{r'}^3 \\
&= \int_\Omega G_f(\vec{r_d}, \vec{r'}) \frac{\phi(\vec{r'}) \mu_{ax \to m}(\vec{r'})}{D^m(\vec{r'})(1 - i\omega\tau(\vec{r'}))} \Phi^x(\vec{r'}, \vec{r_s}) \, d\Omega
\end{aligned}
\tag{3}
$$

where Ω is the integration space and $G_f(\cdot)$ is the Green's function solution of the emission diffusion equation.

In order to reconstruct the spatial map of $\mu_{ax \to m}$ detailing the heterogeneity, we discretize Eqn.(3) into a series of equations in terms of G_f, Φ^x, and measurements of $\widetilde{\Phi^m}(\vec{r_d}, \vec{r_s})$. The solution of the forward problem and determination of G_f and Φ^x, is obtained with MUDPACK, a finite difference differential equation solver.[15] Both forward and inverse problems are carried out in a two-dimensional geometry, since the three-dimensional geometry is prohibitive for the preliminary computations presented herein. We simulate measurements of θ^m and M^m (or $\Phi^m(\vec{r_d}, \vec{r_s}) = M^m e^{i\theta^m}$) at detector position, $\vec{r_d}$, in response to excitation source at $\vec{r_s}$.

By discretizing Eqn.(3),

$$\widetilde{\Phi^m}(\vec{r_{di}}, \vec{r_{sk}}) = \sum_{j=1}^{n} G_f(\vec{r_j}, \vec{r_{di}}) \Phi^x(\vec{r_j}, \vec{r_{sk}}) \frac{\phi(\vec{r_j}) \mu_{ax \to m}(\vec{r_j})}{D_m(\vec{r_j})(1 - i\omega\tau(\vec{r_j}))} h^2 \tag{4}$$

where n is the number of total voxels, h^2 is the area of one pixel, and $i = 1 \ldots n_d$, $j = 1 \ldots Tvoxel$, and $k = 1 \ldots n_s$. respectively, where n_d is the number of detectors, Tvoxel is the total number of voxels, and n_s is the number of sources. The consequent matrix equation, $\widetilde{\Phi^m} = FX$, is

$$
\begin{pmatrix}
\widetilde{\Phi^m}(\vec{r}_s, \vec{r}_d)_1 \\
\widetilde{\Phi^m}(\vec{r}_s, \vec{r}_d)_2 \\
\vdots \\
\widetilde{\Phi^m}(\vec{r}_s, \vec{r}_d)_m
\end{pmatrix}
=
\begin{pmatrix}
F_{11} & \cdots & F_{1n} \\
F_{21} & \cdots & F_{2n} \\
\vdots & \ddots & \vdots \\
F_{m1} & \cdots & F_{mn}
\end{pmatrix}
\begin{pmatrix}
X(\vec{r}_1) \\
X(\vec{r}_2) \\
\vdots \\
X(\vec{r}_n)
\end{pmatrix}
\tag{5}
$$

$$
F_{ij} = \frac{G_f(\vec{r}_{di}, \vec{r}_j)\Phi^x(\vec{r}_{si}, \vec{r}_j)\phi(\vec{r}_j)h^2}{D^m(\vec{r}_j)(1 - i\omega\tau(\vec{r}_j))}
$$

$$
X(\vec{r}_j) = \mu_{ax \to m}(\vec{r}_j)
$$

where $F \in C^{m \times n}$, $X \in R^n$, $\widetilde{\Phi^m} \in C^m$, respectively. Also, $m = n_d \times n_s$, n is the total number of voxels (Tvoxel$= 17^2$).

In the case of reconstruction of τ, the matrix, F_2, and the solution vector, Y, are constructed such that

$$
F_{2,ij} = \frac{G_f(\vec{r}_{di}, \vec{r}_j)\Phi^x(\vec{r}_{si}, \vec{r}_j)\mu_{ax \to m}(\vec{r}_j)\phi(\vec{r}_j)h^2}{D^m(\vec{r}_j)}
$$

$$
Y(\vec{r}_j) = \frac{1}{(1 - i\omega\tau(\vec{r}_j))}
\tag{6}
$$

where $F_2 \in C^{m \times n}$, $Y \in C^n$, respectively.

4. SIMULATION

The simulation of Forward and Inverse problems in lifetime reconstruction is carried out using MUDPACK, a finite difference partial differential equation solver.[15] Both forward and inverse problems are simulated on 17×17 grids. and the dimension of 2-D geometry is chosen to be a 4×4 [cm^2] square leading to the pixel length of 0.25 cm^2. The refractive index of the phantom is set to 1.33 to mimic the properties of tissue. A source is centered on each side of the square phantom, and 56 detectors are evenly spaced around the phantom. Under condition of perfect uptake. a fluorescent contrast agent will preferentially be taken up in a tissue volume of interest. However. we confine our simulation to consider imperfect uptake with 100:1 uptake ratio unless otherwise specified. Also. in the lifetime reconstruction, we will consider the case where the lifetime of the heterogeneity. τ^h. is shorter than that of the background, τ^b. The following table lists the values of optical properties used in the simulation. There

Table 1. Optical properties of background and heterogeneity in the simulation.

	Optical Properties						
	$\mu_{am \to i}$ (cm^{-1})	$\mu_{am \to m}$ (cm^{-1})	μ'_{sx}, μ'_{sm} (cm^{-1})	ϕ	τ (ns)	$\mu_{ax \to i}$ (cm^{-1})	$\mu_{ax \to m}$ (cm^{-1})
Background	0.002	0.0	10.0	0.03	1.0	0.0	0.002
Heterogeneity	0.002	0.0	10.0	0.03	1.0	0.0	0.2

are two parts in the simulation: the forward and inverse simulations. The forward simulator is used to compute simulated measurements. For solutions of the forward problem, the known optical properties of the background and the heterogeneity shown in Table 1 are used to calculate the fluence at each node, and the complex fluence values are collected at the detector nodes. Gaussian random noise is added and the calculated values are used as simulated measurement input into the inverse problem. The following describes the simulation data generation and inversion.

- Forward solution

    1. One of four isotropic point sources of $1/D^x(\vec{r}_s)$ is active at a time. The isotropic point source. $3(\mu_{ax} + \mu_{sx})\delta(\vec{r} - \vec{r}_s)$, represents the incident light at the simulated air-tissue interface.

2. The complex excitation fluence, $\Phi^x(\vec{r})$, is calculated at each grid point in response to an isotropic source. Zero fluence boundary condition is imposed.

3. The calculated excitation fluence, $\Phi^x(\vec{r})$, at each node is coupled into the source term of the emission diffusion equation in Eqn.(2), and the complex emission fluence, $\Phi_m(\vec{r}, \vec{r_s})$, is calculated. Then, the complex emission fluence at the detector position $\vec{r_d}$, $\Phi^m(\vec{r_d}, \vec{r_s})$ is determined at 56 detector positions.

4. The next source becomes active and the previous steps are repeated. In the end, a total of 224 simulated detector measurements are stored in a column vector, $\widetilde{\Phi^m}$.

5. Random Gaussian 1% AC amplitude and 5° (or 10°) phase noises are added.

- Inverse solution

The spatial map of absorption coefficient due to fluorophores, $\mu_{ax \to m}(\vec{r})$ is obtained by Levenberg-Marquadt method. The reconstruction of lifetime of the fluorophores follows the same inversion procedures except the parameter of interest is τ instead of $\mu_{ax \to m}$. The procedure is as follows.

1. The Green's function, $G_f(,)$ and the background excitation fluence, Φ_b^x are solved using MUDPACK. For the first iteration, $\Phi^x(\vec{r_s}, \vec{r})$ is set equal to $\Phi_b^x(\vec{r_s}, \vec{r})$ and $\mu_{ax \to m}(\vec{r})$ to $\mu_{ax \to m, b}(\vec{r})$. (i.e. Born approximation). The iteration counter, k, is set to zero, and the regularization parameter, λ, is adjusted to an initial value.

2. The matrix $F^{(i)}$ is calculated from $G_f(,)$, $\Phi^x(\vec{r_s}, \vec{r})$, and given estimates of ϕ, τ, and D^m.

3. The update, $\Delta\mu_{ax \to m}$, is obtained by solving

$$\Delta X = (F^{(k)}F^{(k)^H} + \lambda I)^{-1} F^{(k)^H} (\widetilde{\Phi^m} - F^{(k)}X^{(k)})$$

where X is $\mu_{ax \to m}$, and, for lifetime measurement, X is equal to τ. The regularization parameter, λ is incorporated to reduce the condition number of $F^{(k)}F^{(k)^H}$ matrix since the matrix is ill-posed.[16]

4. $\mu_{ax \to m}^{(k+1)}(\vec{r}) = \mu_{ax \to m}^{(k)}(\vec{r}) + \Delta\mu_{ax \to m}(\vec{r})$.

5. Calculate $RMSE^{(k)}$.

6. If $RMSE^{(k)} \geq RMSE^{(k-1)}$, λ is increased and procedures starting at step 3 are repeated.

7. Increment the counter, k=k+1.

8. The forward solver is called and the excitation fluence, $\Phi^{x^{(k)}}$ is updated.

9. Repeat until the convergence criteria is satisfied.

This reconstruction algorithm is different from other conventional absorption imaging modalities in that the absorption coefficient owing to the fluorophore is updated with the detected fluorescent wave, $\Phi^m(\vec{r_d})$, and not with $\Phi_{scatt}^x(\vec{r_d})$. Thus, only the incident excitation wave, $\Phi_{inc}^x(\vec{r})$ is updated iteratively, rendering the problem a Fredholm integral equation of the first kind. This algorithm utilizes the added optical contrast in terms of phase-shift and amplitude demodulation due to the fluorophore.

5. RESULTS

To compare the overall accuracy of the reconstruction, the relative root-mean-square error (RMSE) of the reconstructed profile as a function of the iteration steps. The relative RMSE is defined as

$$RMSE^{(i)} = \sqrt{\frac{\sum_j [X^{(i)}(\vec{r_j}) - X^a(\vec{r_j})]^2}{\sum_j [X^a(\vec{r_j})]^2}} \qquad (7)$$

where $X^{(i)}(\vec{r_j})$ is the reconstructed value of the parameter of interest in the ith iteration ($\mu_{ax \to m}$ or τ) and in the jth cell, with $X(\vec{r_j})$ being the actual value. While artificial for this synthetic demonstration of the inverse imaging algorithm, our criteria nonetheless provides information for comparisons between several test cases given in following sections. In the ultimate execution, RMSE is determined from the errors between measured and computed phase and amplitude attenuation.

(a) 1 iteration   (b) 200 iterations

(c) 1 iteration   (d) 200 iterations   (e) RMSE$^{(i)}$ vs. Iteration
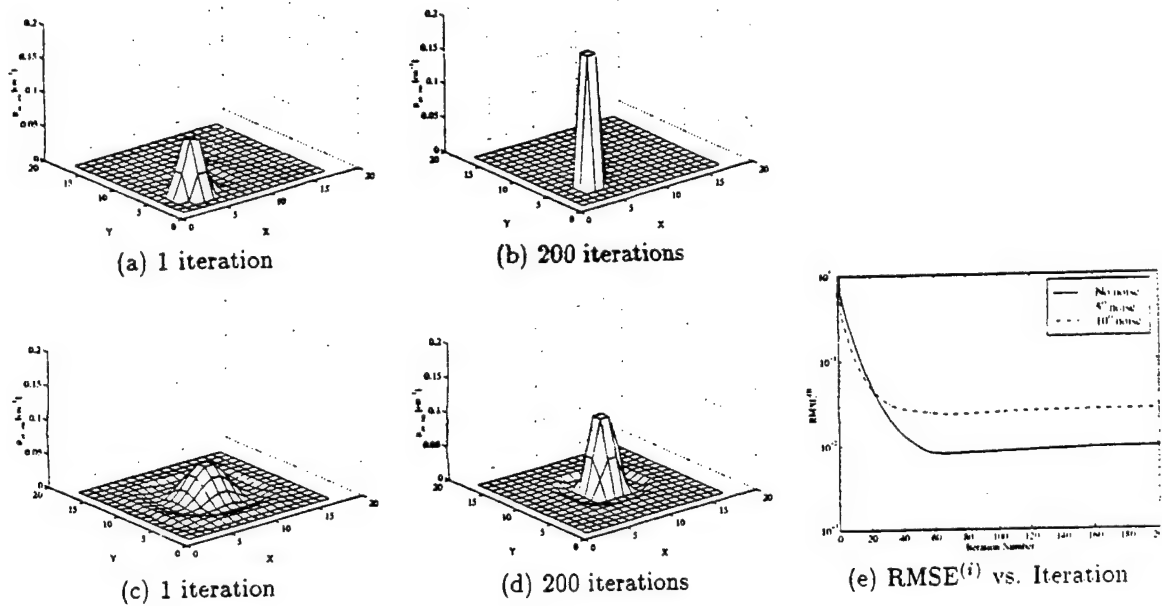
Figure 1. $\mu_{ax \to m}$ reconstruction with 1% amplitude and 5° phase error, 100:1 uptake ratio. $\mu_{ax \to m}^h = 0.2\,cm^{-1}$. $\mu_{ax \to m}^b = 0.002\,cm^{-1}$, frequency=100MHz, and $\lambda = 10^{-8}$. (a), (b) object at (4,4). and (c), (d) object at (9,9). (e) comparison between RMSE$^{(i)}$ values without noise and with 5° and 10° phase noise and 1% amplitude noise.

5.1. Reconstruction with noise

Random Gaussian noise of 1% amplitude and 5° and 10° phase errors are added to $\widetilde{\Phi^m}(\vec{r}_d)$ to test the stability of the algorithm. Figure 1 shows that this reconstruction algorithm was able to reconstruct the absorption map even in the presence of 10° phase random noise. This robustness of algorithm is attributed to the added phase and amplitude contrast from the fluorescence dynamic, which is absent from the conventional absorption algorithm. One can see the effect of the added noise in the RMSE vs. iteration plot. As expected, the calculated RMSE values in the presence of amplitude and phase noises are considerably higher than the case without noise. The small difference in RMSE values indicate that the presence of noise does not affect the reconstruction of $\mu_{ax \to m}$ significantly.

5.2. τ and $\mu_{ax \to m}$ simultaneous reconstruction

In the previous section, we showed that the absorption coefficient reconstruction with the emission wave, Φ^m. instead of the excitation wave, Φ^x was possible. Since the additional phase contrast comes from the lifetime of the heterogeneity, τ^h, we can consider the phase contrast originating from τ^h as an additional phase error. Taking into account that the fluorescence-enhanced imaging can withstand high phase error, we construct the map of $\mu_{ax \to m}$ first, and then construct the lifetime map. The reconstruction of $\mu_{ax \to m}$ and τ was alternately repeated until the desired RMSE values were achieved. Figure 2 and Figure 3 show the reconstruction results. In the simultaneous reconstruction scheme, the original $\mu_{ax \to m}$ value of 0.2 cm^{-1} was recovered and τ reconstruction converged after less than 20 iterations. The final reconstruction profiles indicate that it is desirable to have an additional phase contrast as well as the absorption coefficient change due to the finite partitioning of fluorophores.

5.3. Results owing to perturbation of a strong absorption region

In real situations, there may exist variation in the absorption coefficient due to the endogenous chromophores inside the phantom. The simulation is performed to test the reconstruction algorithm in the presence of a strong absorption regions besides the heterogeneity positioned at (9,9). The reconstruction results are shown in Figure 4. Since both absorption and lifetime reconstruction is performed using the emission wave information, the fluorescence-enhanced
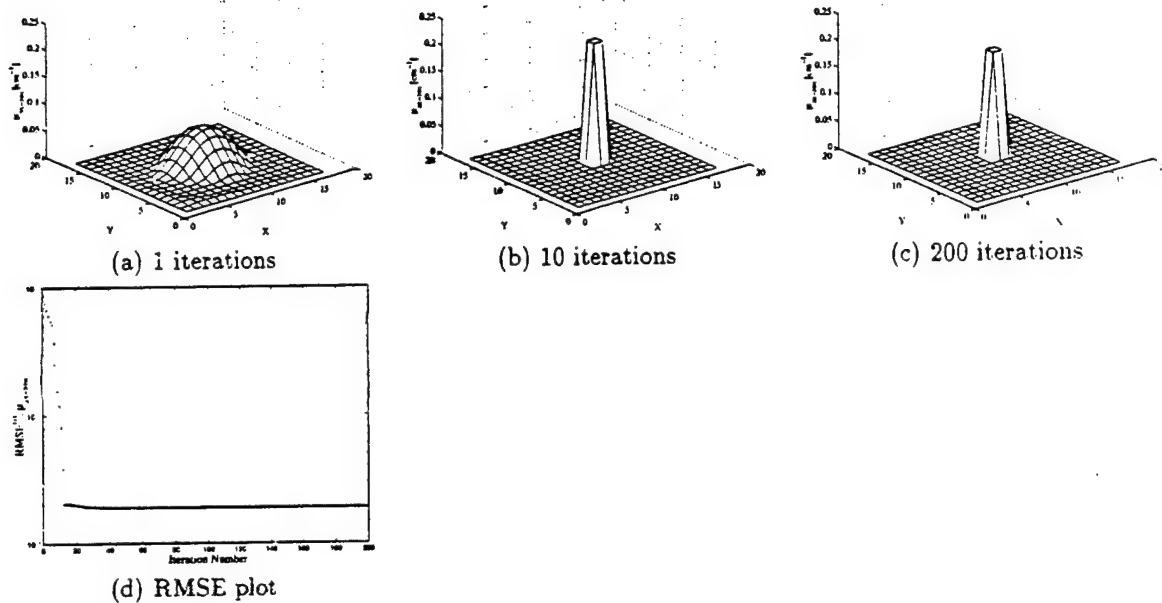
(a) 1 iterations   (b) 10 iterations   (c) 200 iterations

(d) RMSE plot

Figure 2. $\mu_{ax\to m}$ reconstruction results. $\mu_{ax\to m}^{h} = 0.2\,cm^{-1}$, $\mu_{ax\to m}^{b} = 0.002\,cm^{-1}$, initial $\lambda = 10^{-7}$.

(a) 1 iterations   (b) 10 iterations   (c) 200 iterations

(d) RMSE plot
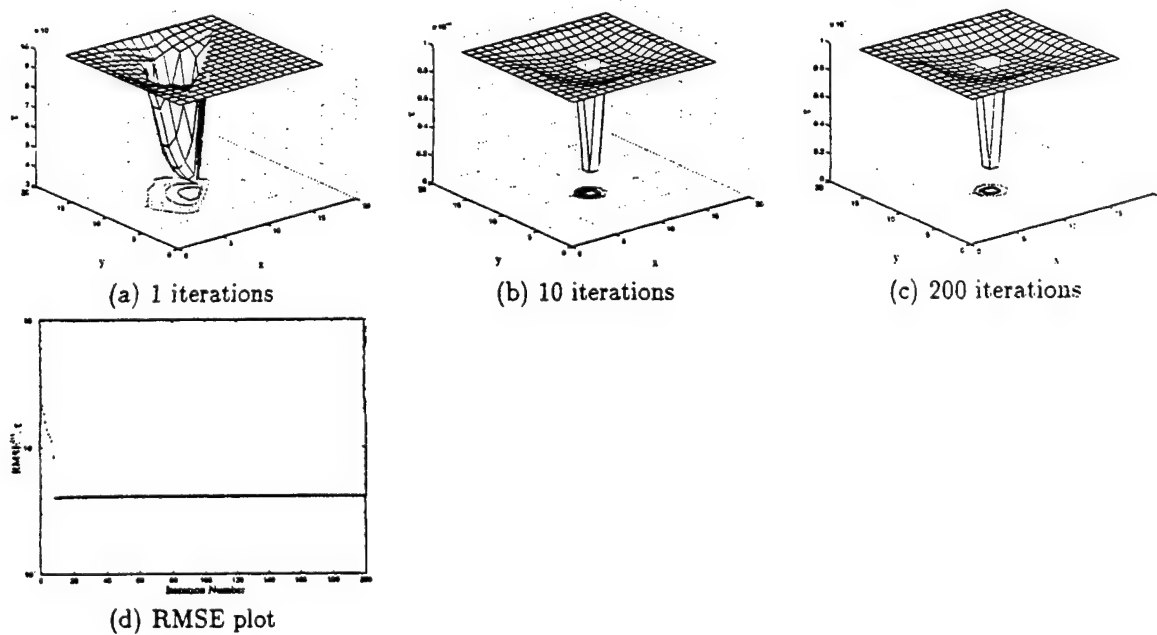
Figure 3. τ reconstruction results. τ^{h}=1ns, τ^{b}=10ns, λ=0.001, frequency=100MHz.
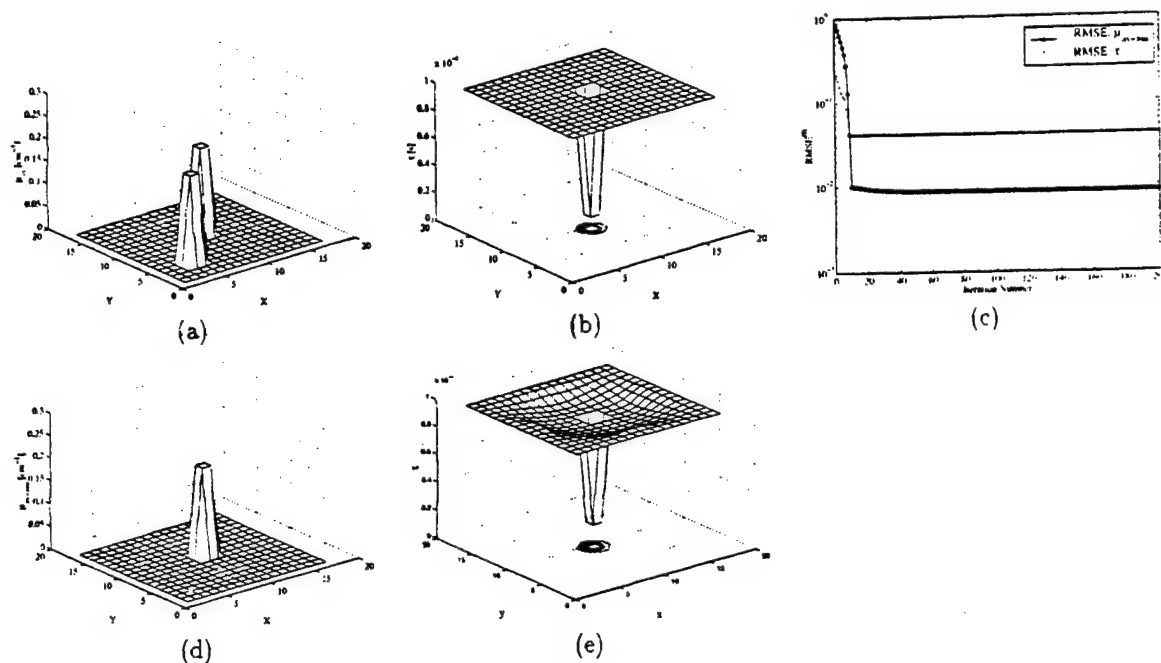
(a)   (b)   (c)

(d)   (e)

Figure 4. Reconstruction of $\mu_{ax \to m}$ and τ in the presence of strong absorption region at (4.4). Heterogeneity is located at (9,9). 100:1 uptake ratio, the reconstruction results were achieved after 200 iterations.

imaging algorithm was able to reconstruct both lifetime and absorption coefficient maps due to the preferential uptake of fluorescent dyes between normal and diseased tissue volumes despite the unaccounted non-fluorescing regions of strong absorption.

6. CONCLUSIONS

In this paper, we demonstrated the novel image reconstruction algorithm using additional phase and amplitude contrast originating from fluorescent contrast agents. The fluorescence-enhanced absorption imaging is robust against the phase and amplitude errors, and using this robustness of the algorithm against noise, we were able to accurately reconstruct absorption coefficient and lifetime map due to the preferential uptake of fluorescent dyes. The simultaneous reconstruction scheme converged to the original values of $\mu_{ax \to m}$ and τ faster due to the additional phase and amplitude information in the emission wave. Moreover, the presence of the strong absorption regions did not affect the reconstruction of lifetime, which, in turn, indicates the robustness of this algorithm. We propose that the development and use of the fluorescent agents which change lifetime upon preferential uptake into diseased tissue volumes will improve discrimination of diseased tissue volumes.

ACKNOWLEDGMENTS

REFERENCES

1. B. C. Wilson amd E. M. Sevick, M. S. Patterson, and B. Chance. Time-dependent optical spectroscopy and imaging for biomedical applications. In *Proceedings of the IEEE*, volume 80, pages 918–930. IEEE, June 1992.
2. W. Cheong, S. A. Prahl, and A. J. Welch. A review of the optical properties of biological tissues. *IEEE Journal of Quantum Electronics*, 26(12):2166–2185, December 1990.

3. D. A. Boas, M. A. O'Leary, B. Chance, and A. G. Yodh. Scattering of diffuse photon density waves by a spherical inhomogeneities within turbid media: Analytic solution and applications. *Proc. Natl. Acad. Sci. USA. Medical Sciences*, 91:4887–4891, 1994.

4. M. A. O'Leary, D. A. Boas, B. Chance, and A. G. Yodh. Images of inhomogeneous turbid media using diffuse photon density waves. In *OSA Proceedings on Advances in Optical Imaging and Photon Migration*, volume 21, pages 106–115. Optical Society of America, 1994.

5. M. A. O'Leary, D. A. Boas, B. Chance, and A. G. Yodh. Experimental images of heterogeneous turbid media by frequency-domain diffusing-photon tomography. *Optics Letters*, 20(5):426–428, March 1995.

6. Y. Yao, Y. Wang, Y. Pei, W. Zhu, and R. Barbour. Frequency-domain optical imaging of absorption and scattering distributions by a born iterative method. *J. Opt. Soc. Am. A.*, 14(1):325–342, January 1997.

7. Y. Yao, Y. Wang, Y. Pei, W. Zhu, and R. Barbour. Simultaneous reconstuction of absorption and scattering distributions in turbid media using a born iterative method. In *SPIE*, volume 2570, pages 96–107, 1996.

8. J. Chang, H. L. Graber, R. L. Barbour, and R. Aronson. Recovery of optical cross-section perturbations in dense- scattering. *Applied Optics*, 35(20):3963–3978, July 1996.

9. T. L. Troy, D. L. Page, and E. M. Sevick-Muraca. Optical properties of normal and diseased breast tissues: Prognosis for optical mammography. *Journal of Biomedical Optics*, 1(3):342–355, July 1996.

10. M. A. O'Leary, D. A. Boas, B. Chance, and A. G. Yodh. Fluorescence lifetime imaging in turbid media. *Optics Letters*, 21(2):158–160, January 1996.

11. J. Chang, H. L. Graber, and R. L. Barbour. Improved reconstruction algorithm for luminescence optical tomography when background lumiphore is present. *Applied Optics*, 37(16):3547–3552, June 1998.

12. J. Chang, H. L. Graber, and R. L. Barbour. Luminescence optical tomography of dense scattering media. *J. Opt. Sci. Am. A*, 14(1):288–299, Januaary 1997.

13. E. M. Sevick-Muraca, G. Lopez, J. S. Reynolds, T. L. Troy, and C. L. Hutchinson. Fluorescence and absorption constrast mechanisms for biomedical optical imaging using frequency-domain techniques. *Photochemistry and Photobiology*, 66(1):55–64, 1997.

14. J. J. Duderstadt and L. J. Hamilton. *Nuclear Reactor Anaysis*. John Wiley & Sons, Inc., New York. 1976.

15. J. C. Adams. Mudpack: Multigrid portable fortran software for the efficient solution of linear elliptical partial differential equations. *Appl. Math. Comput.*, 34:113–146, 1989.

16. A. Tikhonov and V. Arsein. *Solution of Ill-posed Problem*. V. H. Winston, Washington D. C., 1977.

Fluorescence Lifetime Imaging and Spectroscopy in Random Media

T.L. Troy, E.M. Sevick-Muraca

Abstract. With the development of near-infrared (NIR) laser diodes, the synthesis of fluorescent dyes with excitation and emission spectra in the NIR wavelength regime has accelerated in the past decade for microscopy applications. Owing to the window of low absorbance in tissues in this wavelength regime, an opportunity also exists for the deployment of fluorescent dyes as in vivo diagnostic agents. Figure 1.1 illustrates the typical absorbance spectra of tissues showing that at wavelengths less than 650 nm, hemoglobin absorbance provides the predominant attenuation of light in tissues, and above 900 nm water absorbance provides the predominant attenuation of light in tissues. In the "therapeutic window" of 650–900 nm, a window of low absorption exists in which light will be preferentially scattered over being absorbed. Consequently, it is possible to transmit multiply scattered NIR light across several centimeters of tissue. In addition, it is possible to excite NIR fluorophores deep within tissues and to collect the fluorescence re-emitted from the air-tissue interface. Since fluorescence provides a sensitive means for assessing local biochemistry via changes in quantum efficiency and lifetime, the ability to diagnose tissues based on spectroscopic evaluation of lifetime and quantum efficiency of exogenous diagnostic agents is possible. Agents whose emission characteristics vary with tissue pH [1, 2] and pO_2 [3] have been employed to detect diseased tissues by the nature of differing fluorescent properties as well as to provide diagnostic information regarding the diseased tissue volume. While typical contrast agents employed for the detection of diseased tissues depend on and are limited by the poor preferential uptake, the alteration of fluorescent properties provides a unique mechanism for inducing additional contrast [4]. For example, using time-gating to collect the long-lived fluorescence from hematoporphyrin derivative (HpD), Cubbeddu and co-workers [5, 6] were able to differentiate normal tissues from intradermally or subcutaneously implanted murine tumors in mice. More recently, it has been reported that the fluorescent decay of HpD is appreciably slower in experimental mice tumors than in their surrounding normal healthy tissues. Consequently, the use of a fluorescent dye may provide contrast owing to changes in fluorescent properties within tissue compartments.

The difficulty, however, lies in understanding the use of multiply scattered excitation light to excite a fluorophore in the tissue, and secondly, to extract information of lifetime and quantum efficiency from the multiply scattered

fluorescence detected at the air-tissue interface. If the optical properties of the tissue are spatially uniform and the fluorescent dye has constant fluorescent properties, then the problem is one of *fluorescent lifetime spectroscopy* in tissues. However, if the detection of diseased tissues is to be tackled, the problem becomes one of *fluorescent lifetime spectroscopic imaging*, since optical properties and fluorescent properties of diagnostic agents may vary with spatial location.

In this chapter, frequency domain photon migration fluorescence imaging is described as a method for generating an optical map or image of fluorescent lifetime and quantum efficiency from exterior measurements of modulation phase and modulation amplitude on tissues or highly scattering media. In Sect. 1, the theory behind the propagation of excitation light and generation of fluorescent light within scattering media such as tissues is presented. Section 2 describes experimental measurements which show that the delay in phase and decrease in amplitude of fluorescence measured in simulated tissue phantoms varies as a function of dye lifetime. Section 3 describes the general theory behind the derivation of an optical property map from measurements of modulation phase and amplitude of fluorescent light detected at the tissue surface, and Sect. 4 presents actual images generated from simulated measurements of modulation phase and amplitude. Finally, the prognosis for moving these theoretical and computational studies into an experimental demonstration is commented upon.

1
Principles of Photon Migration

1.1
Time and Frequency Domain Photon Migration

Photon migration techniques consist of measuring the time-dependent light propagation of multiply scattered light as it is transmitted through tissue. Two techniques are used to monitor the time dependence of photon migration in a scattering medium: (i) time domain, and (ii) frequency domain techniques. In the time domain technique, a picosecond impulse of light is launched into a scattering medium and the intensity of the detected light is recorded as a function of picosecond to nanosecond time. As time progresses, fewer photons are detected with longer "times-of-flight." Figure 1.2 shows the broadened pulse that is re-emitted and measured representing the distribution of photon "times-of-flight" traveled by the detected photons. In the frequency domain (Fig. 1.3), incident light whose intensity is sinusoidally modulated is continuously launched into a scattering sample. As the "photon density wave" of light propagates, it experiences a phase lag and an amplitude reduction relative to the incident light. The phase-shift and amplitude modulation are related to the optical properties of the medium. Both the modulation phase and amplitude are measured as a function of multiple frequencies. The modulation ratio is defined as the modulation amplitude divided by the average intensity.
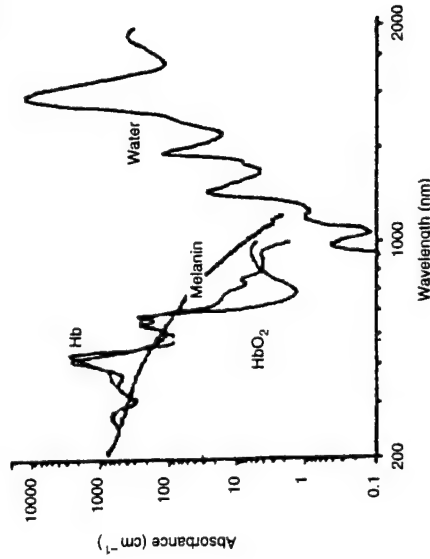
Fig. 1.1. Dependence of absorption on wavelength illustrating the "therapeutic window" in which the propagation of light through tissue is high. Reproduced from [7]
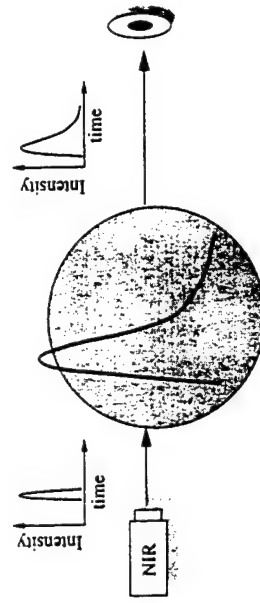

Fig. 1.2. In the time domain, an impulse of light is launched into a scattering medium. The detected pulse is broadened due to the increase in photon "times-of-flight"
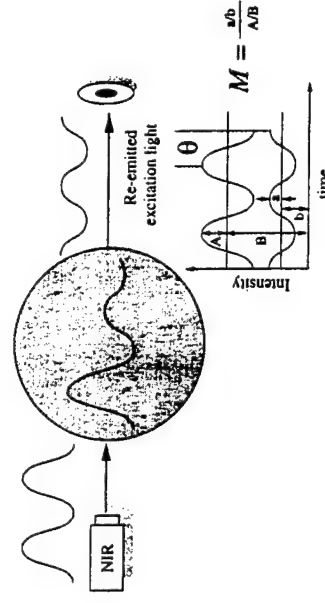

$$M = \frac{a/b}{A/B}$$

Fig. 1.3. In the frequency domain, a sinusoidally modulated source is launched into a scattering medium. The detected signal's phase is shifted and amplitude is decreased relative to the incident light

The intensity of the re-emitted light as a function of time (time domain), or the phase and amplitude of the modulated, re-emitted light as a function of the modulation frequency (frequency domain) contains identical information regarding the transport of light through the scattering medium. Time and frequency domain measurements are mathematically related to each other by the Fourier transform.

Photon migration imaging consists of (i) the forward problem of measuring the time-dependent characteristics of light propagation and (ii) the inverse problem of reconstructing an image of normal and diseased tissues based on their contrasting optical properties. In the following, the properties which impact the propagation of excitation light are reviewed.

1.2
Transport Property: Absorption Coefficient

The absorption coefficient, μ_a, is the inverse of the mean distance a photon will travel before being absorbed. In tissue, oxy- and deoxy-hemoglobin are the predominant endogenous absorbers in the therapeutic window (Fig. 1.1). In this wavelength range, most tissues have an absorption coefficient in the range of 10^{-2} to 10^{-1} cm^{-1} [8].

In the absence of scattering, the absorption coefficient can be found from the attenuation of light directly using the Beer-Lambert law:

$$\mu_a = -\frac{1}{L} \ln \frac{I}{I_0} = \varepsilon_\lambda [C] \qquad (1.1)$$

where μ_a is the absorption coefficient of the medium (cm^{-1}); L is the optical path length light travels (cm); I is the intensity of the detected light [number of photons/(cm$^2 \cdot$ s)]; I_0 is the intensity of the incident light [number of photons/(cm$^2 \cdot$ s)]; ε_λ is the extinction coefficient at wavelength λ (cm^{-1} mM^{-1}); and [C] is the concentration of the light-absorbing species (mM). Note that the number of photons per second can be converted into units of power (Watts) by multiplying by the photon's energy.

Equation 1.1 describes an absorption coefficient that is inversely related to the optical path length, L. In the presence of a scattering medium such as tissue, there is no unique path length, but rather a distribution of path lengths (Fig. 1.4). Therefore, determination of the absorption coefficient in a scattering medium is not possible from the Beer-Lambert relationship.

1.3
Transport Property: Scattering Coefficient

The scattering coefficient, μ_s, describes the distance photons travel between scattering events. Scattering in tissue occurs due to the index of refraction mismatch between fluid and cellular organelles. Mitochondria are postulated to be the predominant scatterer in tissues [9, 10].
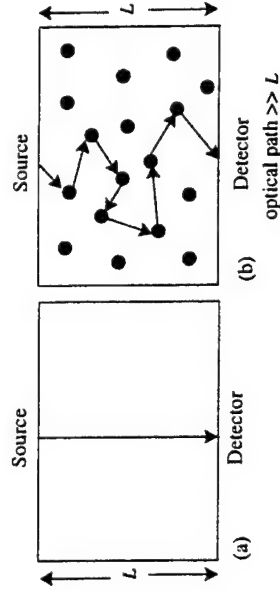
Fig. 1.4. Light propagation in a non-scattering **a** and **b** a scattering medium

When multiple scattering occurs, light no longer follows a straight path. Instead, photons travel a distribution of optical path lengths, rendering the Beer-Lambert law invalid. As shown in Fig. 1.4, the total optical path length, L, is now defined as the sum of all individual paths, ℓ_i's, between scatterers and the scattering coefficient is defined as the inverse of the mean scattering length ℓ^*:

$$\mu_s = \frac{1}{\ell^*} \qquad (1.2)$$

Since "photon migration" describes a random walk of photons between scatterers, it is often more convenient to define the scattering parameter as the isotropic scattering coefficient [$\mu_s' = \mu_s (1 - g)$] where the anisotropy coefficient, g, is defined below. In the NIR wavelength range, the values of μ_s' for tissues typically range from 10 to 50 cm^{-1} [8].

1.4
Transport Property: Anisotropy Coefficient

The anisotropy coefficient, g, is defined as the mean cosine of the scattering angle at which a photon deflects from a scatterer. Flock et al. [11] have shown that the Henyey-Greenstein phase function describes the angular scatter of light in tissue. This phase function describes the relationship between g and the collimated transmittance, T_c, at a scattering angle θ where:

$$T_c(\theta) = \frac{(1 - g^2)}{(1 + g^2 - 2g \cos \theta)^{3/2}} \qquad (1.3)$$

Collimated transmittance is a measure of the light intensity which is transmitted through the sample as a function of the scattering angle θ. Using a least-squares analysis of several measurements of T_c vs. θ, the anisotropy coefficient can be obtained from Eq. 1.3. The anisotropy coefficient varies between isotropic (g=0) and forward (g=1) scattering. In all tissues, light is known to be forward scattering and the anisotropy coefficient is reported to be around 0.9 [12]. The Henyey-Greenstein phase function is widely used in tissue optics studies not only because it provides a good representation of experimental tissue measurements but also because it is mathematically simple.

1.5
Governing Equations Describing the Transport of Light

The scattering, absorption, and anisotropy coefficients are parameters that govern the propagation of light in any medium. Analysis of light transport is analogous to that of the motion of neutrons in a reactor core where neutrons diffuse from regions of high to low density [13]. When photons rather than neutrons are employed, the one-speed radiative transport equation describes light propagation in a scattering medium. The radiative transport equation is written in terms of the integro-differential equation governing the local number of photons, $n(\bar{r}, E, \hat{\Omega}, t)$, at position $\bar{r}$ and time t, and traveling with energy E and angular direction $\hat{\Omega}$ [14]:

$$\frac{\partial n(\bar{r}, E, \hat{\Omega}, t)}{\partial t} = -c\hat{\Omega} \cdot \nabla n - c\mu_t n(\bar{r}, E, \hat{\Omega}, t) + s(\bar{r}, E, \hat{\Omega}, t) +$$

$$\int_{4\pi} d\hat{\Omega}' \int_0^\infty dE' c \, \mu_s'(E' \rightarrow E, \hat{\Omega}' \rightarrow \hat{\Omega}) \, n(\bar{r}, E', \hat{\Omega}', t) \quad (1.4)$$

The term on the left-hand side (LHS) represents the local accumulation of photons, while the first term on the right-hand side (RHS) represents the flux of photons into the system. The second term on the RHS represents the loss of photons traveling with energy E in direction $\hat{\Omega}$ due to absorption and scattering events. The total cross section for these extinction processes, μ_t, is given by the sum of the absorption and scattering cross sections, $\mu_t = \mu_a + \mu_s'$ (cm^{-1}). The third term on the RHS represents the source, and along with the second term accounts for the rate of addition of photons traveling in direction $\hat{\Omega}$ with energy E which have been scattered from direction $\hat{\Omega}'$ and energy E'. To account for scattering from photons traveling in all directions and energies, that last term on the RHS is integrated over all solid angles, $\int_{4\pi} = \int_0^{2\pi} \int_0^\pi \sin\theta \, d\theta \, d\phi$, and energies. The symbol c represents the speed of photons (cm/s).

1.5.1
One-Speed Approximation to the Transport Equation

When all the neutrons or photons travel at the same speed, the neutron transport equation can be reduced to the one-speed approximation by eliminating the dependence on energy, E. By writing the local concentration of photons in terms of an angular flux, φ [number of photons/(cm^2 · steradians · s)], where φ $(\bar{r}, \hat{\Omega}, t) = cn(\bar{r}, \hat{\Omega}, t)$, the one-speed equation is given in Eq.1.5 [13]:

$$\frac{1}{c} \frac{\partial \varphi}{\partial t} = -\hat{\Omega} \cdot \nabla \varphi - \mu_t(\bar{r}) \, \varphi(\bar{r}, \hat{\Omega}, t) + s(\bar{r}, \hat{\Omega}, t)$$

$$+ \int_{4\pi} d\hat{\Omega}' \mu_s'(\hat{\Omega}' \rightarrow \hat{\Omega}) \, \varphi(\bar{r}, \hat{\Omega}', t) \quad (1.5)$$

The term $\hat{\Omega} \cdot \nabla \varphi$ represents the negative rate of addition of photons traveling in an angular direction $\hat{\Omega}$. The term $\mu_t(\bar{r}) \varphi(\bar{r}, \hat{\Omega}, t)$ accounts for the loss of photons traveling in direction $\hat{\Omega}$ due to scatter and absorption. The integral term $s(\bar{r}, \hat{\Omega}, t)$ represents photons scattering from direction $\hat{\Omega}'$ into the direction $\hat{\Omega}$. The term $s(\bar{r}, \hat{\Omega}, t)$ represents a source of photons [number of photons/(cm^3 · steradians · s)] traveling in a direction $\hat{\Omega}$ at a position $\bar{r}$ and time t [13].

1.5.2
Diffusion Equation Describing Light Propagation in Tissues

Following the derivation of Duderstadt and Hamilton [13], the one-speed equation can be reduced to the diffusion equation describing light propagation in tissues:

$$\frac{1}{c} \frac{\partial \Phi}{\partial t} = \nabla \cdot D(\bar{r}) \nabla \Phi - \mu_a(\bar{r}) \, \Phi(\bar{r}, t) + S(\bar{r}, t) \quad (1.6)$$

Equation 1.6 represents the time domain diffusion equation which can analogously be written in the frequency domain [14, 15] as:

$$\frac{i\omega}{c} \Phi^{AC}(\bar{r}, \omega) - \nabla \cdot D\nabla \Phi^{AC}(\bar{r}, \omega) + \mu_a \Phi^{AC} = M\delta(\bar{r}_s - \bar{r}) \quad (1.7)$$

where Φ^{AC} is the AC component of the fluence at position $\bar{r}$ and frequency ω; M is the modulation of the point source; and $\bar{r}_s$ denotes the source position.

1.5.3
Source Location and Boundary Conditions

A collimated light source incident on a scattering medium is slowly transformed into a diffuse source as it encounters scatterers. Patterson et al. [16] have analytically shown that in order to accurately represent an incident laser light source at the surface, the simulated source location has to be set to:

$$z_0 = \frac{1}{\mu_s'} \quad (1.8)$$

Therefore, in order to accurately simulate a laser source located on the surface, the placement of the simulated source needs to be one isotropic scattering length inside the physical boundary. A sinusoidally modulated light source can be represented by a complex number [17]:

$$S = S_0[\cos(\theta) + i\sin(\theta)] \quad (1.9)$$

where θ and S_0 are the phase and the amplitude of the source, respectively.

The three most common boundary conditions used to solve the diffusion equation at the air-scatterer interface of a random medium are the (i) zero fluence boundary condition, (ii) the partial current boundary condition, and

(iii) the extrapolated boundary condition. The zero fluence boundary condition defines $\Phi = 0$ on and outside the boundary. Although the zero fluence condition is physically inaccurate, it is mathematically simple and gives solutions to the diffusion equation which agree well with experimental data for biological systems [8].

1.6
Non-Radiative Mechanisms for Exogenous Contrast

As discussed above, the diffusion equation (Eqs. 1.6 and 1.7) describes the propagation of light in a highly scattering medium. This equation depends on the propagation of light in a highly scattering medium. This equation depends on three parameters: (i) the speed of light c, (ii) the isotropic scattering coefficient, μ'_s, and (iii) the absorption coefficient μ_a. Since all these parameters govern the migration of photons in tissue, an exogenous compound which alters the characteristics of any of these parameters can be used to induce contrast for imaging and provide information for diagnostic information.

1.6.1
Contrast Due to Absorption

The propagation of a photon density wave through a medium containing a region of light absorbing dye is different from the propagation of a wave in a medium with uniform optical properties as illustrated in Fig. 1.5. The "homogeneous" propagation is similar to a wave formed by a pebble being dropped in a shallow pond. The propagating wave dampens as it travels across the surface but the wave maintains coherence. When the wave encounters an optical heterogeneity (or diseased tissue with different optical properties), it will reflect, diffract, and be absorbed [18]. The "heterogeneous" situation is similar to a pebble being dropped in the shallow pond with a solid obstruction in the wave's path. The solid obstruction will absorb and partially reflect a re-scattered wave. At any position, the diffusing wave will be the sum of the incident wave and the scattered wave.

Since these differences in light propagation enable contrast, photon migration measurements are conducted relative to an absence (homogeneous) condition. The phase contrast, $\Delta\theta$, and modulation contrast, ΔM, are defined as:

$$\Delta \theta = \theta_{presence} - \theta_{absence}$$

(1.10)

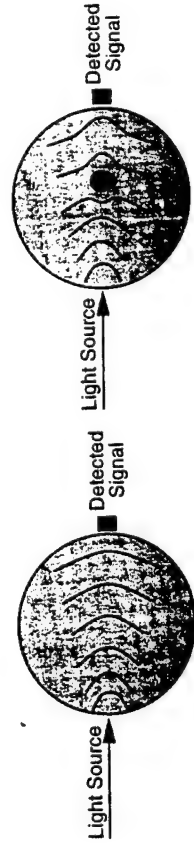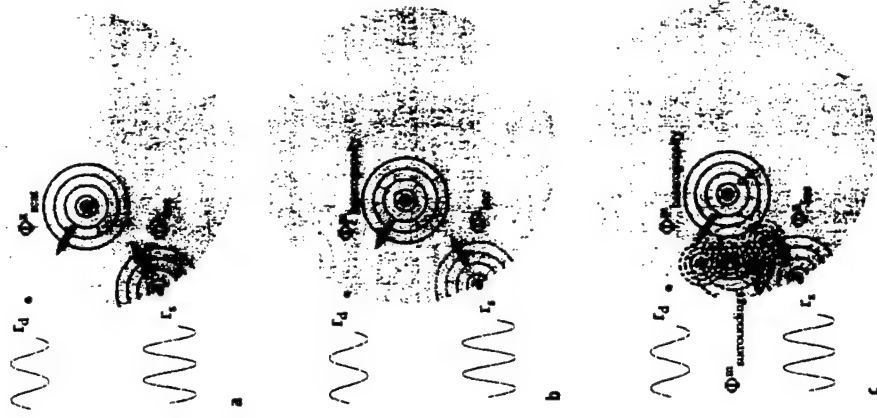Light Source   Detected Signal   Light Source   Detected Signal

Fig. 1.5. Schematic describing the propagation of a photon density wave across a medium in the absence and presence of a heterogeneity with optical contrast

$$\Delta M = \frac{M_{presence}}{M_{absence}}$$

(1.11)

where $\theta_{presence}$ and $M_{presence}$ are, respectively, the measured modulation phase and modulation ratio in the presence of a heterogeneity. Likewise, $\theta_{absence}$ and $M_{absence}$ are, respectively, the measured modulation phase and modulation ratio in the absence of a heterogeneity. If the optical contrast relative to an absence condition is significant enough to cause $\Delta\theta \neq 0$ and $\Delta M \neq 1.0$, then it may be possible to reconstruct an interior optical property map from exterior measurements of modulation phase and amplitude as described in Sect. 3.

Since phase and amplitude contrast depend on differences caused by an absorbing heterogeneity, the physics which change the detected wave need to be examined. Figure 1.6a describes frequency domain photon migration imaging

Fig. 1.6. Schematic illustrating frequency domain photon migration measurements of a sinusoidally modulated excitation light source at position $\bar{r}_s$ and the detected excitation and emission (fluorescent) signals at position $\bar{r}_d$ when contrast is due to a absorption, b perfect uptake of a fluorescent dye, and c imperfect uptake of fluorescent dye

which consists of launching a sinusoidally modulated light source at position $\vec{r}_s$ and measuring the detected signal at position $\vec{r}_d$. The propagation of the wave through the medium causes a decrease in modulation and an increase in phase at position $\vec{r}$ relative to the incident wave. The magnitude of a scattered wave depends on the heterogeneity's distance from the source, its dimensions, and the absorption difference between it and the surroundings. The magnitude of a scattered wave will be greatest closest to the source. The greatest magnitude possible will occur when there is no loss mechanism (no absorption) in the surroundings and the heterogeneity is a perfect absorber (a black body, or μ_a is infinity). Nonetheless, even for a perfect absorber, the incident propagated wave will constitute the predominant signal measured at the detector. Consequently, the scattered wave from an absorber will be small in comparison to the incident propagated wave and the contrast offered by absorption should be low. In other words, absorption contrast consists of the ability to detect a small scattered wave within a very large signal.

1.6.2
Contrast Due to Dye with Fluorescent Characteristics

Another means of inducing contrast is through fluorescence. Imagine an optical heterogeneity which contains a contrast agent that not only absorbs, but also fluoresces light (Fig. 1.6b). In essence, if an interference filter is placed at the detector so that only fluorescence light is seen, the heterogeneity would act like a beacon. Since there is no small signal to identify from a large background signal, the contrast should be significantly greater than that offered by absorption. Usually perfect uptake is not possible and one would imagine that while there is 10-fold or at most 20-fold more dye in a tissue volume of interest than in the surrounding tissues, the problem becomes one of picking the brightest beacon from a number of beacons uniformly distributed in the tissue (Fig. 1.6c). Under these conditions, the fluorescent properties (such as lifetime and quantum efficiency) of the compound may be used to impart additional contrast to that offered simply by a fluorophore concentration difference between the heterogeneity and its surroundings.

1.6.2.1
Physics of Photoluminence

Fluorescence is the emission of a photon which results when a molecule in an excited state relaxes to its original ground state (Fig. 1.7). The excited molecules can either, relax non-radiatively to the ground state (without emitting fluorescence) or stay in the excited state for a period of time before returning to the ground state and emitting a fluorescent photon. Often when π-orbitals are close, an electron in the electronically activated level will experience a change in its spin state. Since relaxation to the ground state populated with same spin state is forbidden, the activated molecule will remain in the excited state for a longer period of time. In this case the emission is termed phosphorescence. Due to the loss of energy associated when the fluorescent or phosphorescent
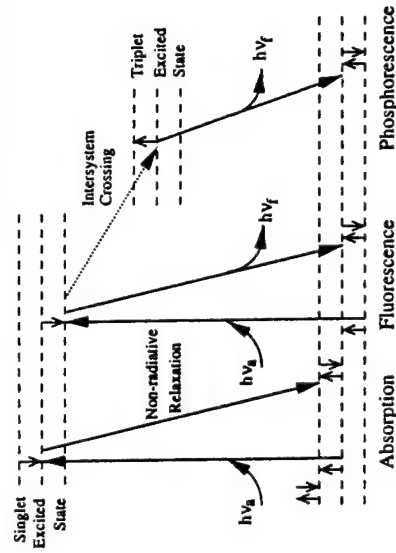
Fig. 1.7. Jablonski diagram illustrating the electronic transitions associated with absorption, fluorescence and phosphorescence

molecules return to the ground state, the emission light occurs at a longer wavelength than the excitation light [19].

The fluorescent properties of a compound are characterized by the quantum efficiency, φ, and the lifetime, τ, of the molecule. The quantum efficiency is the ratio of the number of fluorescent photons emitted to the number of excitation photons absorbed by the fluorophore. The lifetime of the molecule is the average time that the molecule stays in the activated state and is measured as the average time between absorption of an excitation photon and emission of a fluorescent photon. Both lifetime and quantum efficiency are sensitive to the local biochemical environment. For example, porphyrin fluorescence is quenched by oxygen enabling quantitative detection of oxygen from the shortening of its lifetime and reduction of its quantum efficiency [19].

1.6.2.2
Measurrement of Photolumination Properties in Dilute, Non-scattering Suspensions

The lifetime, τ, and quantum efficiency, φ, of a molecule can be determined using both a time and frequency domain analysis. In the time domain, a pulse of light excites a dilute non-scattering solution of fluorophores and the decay of the generated fluorescent intensity is recorded as a function of time after the initial impulse. The amount of fluorescent light, I_m, is defined by the absorption coefficient of the fluorophores, μ_{axf}, the quantum efficiency, φ, and the lifetime, τ, of the molecule [19]:

$$I^m(t) = \frac{\phi \mu_{a_{xf}}}{\tau} e^{-1/\tau} = I_0 e^{-1/\tau} \qquad (1.12)$$

where I_0 is the maximum fluorescent intensity. The lifetime of a fluorophore is equal to the time required for the intensity to decay to $1/e$ of its initial value.

Frequency domain measurements of lifetime, τ, and quantum efficiency, ϕ, are made by exciting a dilute, non-scattering solution of the fluorophore with a sinusoidally modulated source and measuring either the emitted modulation phase or modulation ratio of the fluorescent signal relative to the incident excitation light. The modulation phase of the fluorescent light is independent of the fluorophore concentration and the quantum efficiency:

$$\theta^m(\omega) = \tan^{-1}(\omega\tau) \tag{1.13}$$

where ω is the modulation frequency of the light source. The modulation ratio, however, is dependent on quantum efficiency, ϕ, and $\mu_{a_{x \to f}}$:

$$M^m(\omega) = \frac{\mu_{a_{x \to f}}}{\sqrt{1+(\omega\tau)^2}} \tag{1.14}$$

and can therefore be used to determine both lifetime, τ, and quantum efficiency, ϕ, of a sample. If the modulation ratio is referenced to the modulation ratio obtained under continuous wave or constant illumination ($\omega=0$), the resulting ratio is a function of modulation frequency and lifetime τ:

$$\frac{M^m(\omega)}{M^m(0)} = \frac{1}{\sqrt{1+(\omega\tau)^2}} \tag{1.15}$$

Equations 1.13–1.15 are obtained from the Fourier transform of Eq. 1.12.

The measurement of the emission properties of τ and ϕ are determined in a dilute, non-scattering medium. Since the fluorescent lifetime, τ, is in the same order as photon "times-of-flight," the above equations are not valid in a scattering medium due to the additional time delay and amplitude decrease associated with photon migration. In order to accurately determine the emission properties in a scattering medium, photon migration times need to be deconvolved from time-dependent measurements.

As an alternative, long-lived (phosphorescent) probes have been suggested for photon migration measurements of the re-emission properties in a highly scattering medium since the phosphorescent lifetimes are longer than photon "times-of-flight". However, Hutchinson et al. [20, 21] found that the signal originating from a medium containing phosphorescent agents is confined to surface or sub-surface regions. Since phosphorescent agents cannot be used to determine the lifetime deep within scattering media, fluorescent contrast agents are suggested.

1.6.2.3
Collisional Quenching Mechanisms

Collisional quenching is the mechanism in which the fluorescent intensity decreases due to collisional encounters between a fluorophore and a quencher. For this process to happen, the quencher must diffuse to the fluorophore while the fluorophore is in the excited state. Some examples of collisional quenchers are oxygen, chloride, chlorinated hydrocarbons, xenon, hydrogen peroxide,

bromate, and iodide [19]. The lifetime of a fluorophore can be related to the concentration of a quencher using the Stern–Volmer equation [19]:

$$\frac{\tau_0}{\tau} = 1 + K_{SV}[Q] \tag{1.16}$$

where τ_0 is the lifetime of the probe in the absence of a quencher, τ is the lifetime of the probe in the presence of a quencher, K_{SV} is the Stern–Volmer constant and [Q] is the quencher concentration. As the concentration of the quencher increases, the excited state of the probe is quenched causing a reduction in the lifetime. Since the (bio)chemical environment (amount of quencher present) impacts the fluorescence lifetime, τ, fluorescent lifetime imaging may be used for metabolite sensing. It is important to note that Eq. 1.16 does not depend on the concentration of the fluorophore.

A class of lifetime sensitive fluorophores, called multiplex dyes [22] involve "tuning" cyanine dyes to exhibit different spectra lifetimes depending on local environments and binding characteristics. This ability to change the emission characteristics between normal and diseased tissue using dyes whose characteristics change by varying pH [1, 2] and O_2 [3] may not only enhance detection but may also contain diagnostic information regarding the disease.

1.6.3
Diffusion Equations Describing Excitation and Emission Photon Migration

To use fluorescent contrast agents in forward and inverse imaging problems, fluorescent generation and propagation must be accurately modeled. The light propagation due to fluorescence in a scattering medium can be described by the coupled diffusion equations for light propagation [20, 23, 24]:

$$-\nabla \cdot D_x(\vec{r}) \, \nabla\Phi^x(\vec{r},\omega) + \left[\frac{i\omega}{c_x} + \mu_{a_x}(\vec{r}) + \mu_{a_{x \to f}}(\vec{r}) \right] \Phi^x(\vec{r},\omega) = S(\vec{r},\omega) \tag{1.17}$$

$$-\nabla \cdot D_m(\vec{r}) \, \nabla\Phi^m(\vec{r},\omega) + \left[\frac{i\omega}{c_m} + \mu_{a_m}(\vec{r}) \right] \Phi^m(\vec{r},\omega) = \phi\mu_{a_{x \to f}} \frac{1-i\omega\tau}{1+(\omega\tau)^2} \Phi^x(\vec{r},\omega) \tag{1.18}$$

In the above equations, Φ^x and Φ^m are the AC components of fluence for excitation (superscript x) and emission (superscript m) light (photons/cm^2); $\mu_{a_{x,i}}$ is the absorption due to chromophores (cm^{-1}); $\mu_{a_{x \to f}}$ is the absorption due to fluorophores (cm^{-1}); μ_{a_m} represents the absorption of the emission light due to chromophores (cm^{-1}); μ_{s_x} and μ_{s_m} are the scattering coefficients of excitation and emission light (cm^{-1}), respectively; ϕ and τ are the quantum efficiency and lifetime (ns) of the fluorophore, respectively; and D_x and D_m are the optical diffusion coefficients for the excitation and emission light (cm) where

$$D_x = \frac{1}{3[\mu_{a_x} + (1-g)\,\mu_{s_x}]} \tag{1.19}$$

and

$$D_m = \frac{1}{3[\mu_{a_m} + (1-g)\,\mu_{s_m}]} \qquad (1.20)$$

Equations 1.17 and 1.18 are coupled by the excitation fluence, Φ^x, and the absorption due to fluorescence, μ_{a_f}. The solutions for these equations, Φ^x and Φ^m, are complex. It is important to note that fluorescence is assumed linear with the excitation fluence (e.g. photo-bleaching invalidates the model). The modulation phase, θ, and modulation amplitude, I_{AC}, of the excitation and emission light are represented by the real and imaginary components of the emission and excitation fluence:

$$\theta^{x,m} = \tan^{-1}\left[\frac{\operatorname{Im}\Phi^{x,m}}{\operatorname{Re}\Phi^{x,m}}\right] \qquad (1.21)$$

$$I_{AC}^{x,m} = \sqrt{[\operatorname{Re}\Phi^{x,m}]^2 + [\operatorname{Im}\Phi^{x,m}]^2} \qquad (1.22)$$

and the modulation ratio is obtained by dividing I_{AC} by the average intensity (or I_{DC}):

$$M^{x,m} = \frac{\sqrt{[\operatorname{Re}\Phi^{x,m}]^2 + [\operatorname{Im}\Phi^{x,m}]^2}}{I_{DC}} = \frac{I_{AC}}{I_{DC}}. \qquad (1.23)$$

The mathematical framework for predicting modulation phase and modulation amplitude at emission wavelengths assumes an angle exponential decay kinetics, but can be easily modified for other kinetics.

1.6.4
Potential Fluorescent Contrast Agents for Photon Migration Imaging

An example of a class of potential contrast agents are porphyrin derivatives. Porphyrin molecules have characteristic ring structures derived from four pyrrole rings joined together by four methene bridges as shown in Fig. 1.8.
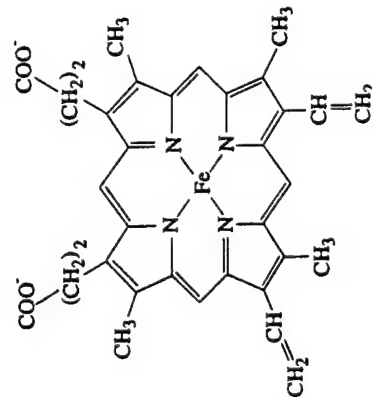
Fig. 1.8. Molecular structure of heme showing the characteristic heterocyclic rings that are common to porphyrin compounds
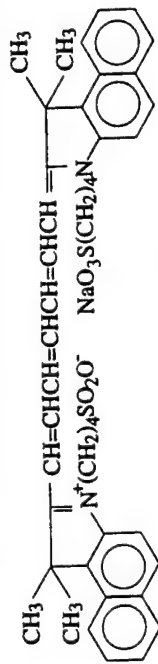
Fig. 1.9. Molecular structure of Indocyanine Green (ICG)

Porphyrin derivatives are typically employed in photodynamic therapy (PDT). PDT is a method in which a hematoporphyrin derivative drug is administered for photo-therapeutic destruction of cancer [25]. In this therapy, a photosensitizing drug, which has a high affinity for tumor tissue, is systematically administered to the patient. The tumor area is then irradiated with red light which photoactivates the dye to a triplet state to produce cytotoxic byproducts causing irreversible cellular damage. Many problems limit the efficacy of photodynamic therapy, such as damage to skin exposed to sunlight. Nonetheless, while PDT agents depend on triplet states for their therapeutic action, the singlet state may enable contrast for diagnostic imaging.

Indocyanine Green (ICG) (Fig. 1.9) is another optically active contrast agent that is approved by the Food and Drug Administration (FDA) for diagnostic studies. It is currently used to diagnose retinal and chorodial diseases by enhancing the images of the retinal vasculature of the eye [26]. In burn diagnostics, ICG is administered to the blood stream after which the burn area is illuminated to monitor the amount of blood flow to the area. Because blood flow is proportional to the depth of the burn, ICG is used to measure the severity of the wound [27]. ICG is also used to determine hepatic function by monitoring the amount of dye that clears the circulatory system of the liver as a function of time. Sevick et al. [4] measured the extinction coefficient, ε_λ, of ICG to be 1300 (M cm)$^{-1}$ at 780 nm and 22.000 (M cm)$^{-1}$ at 830 nm. They also report the quantum efficiency, ϕ, and lifetime, τ, of ICG to be 0.016 and 0.56 ns, respectively. Although their measurements were conducted with ICG diluted in water, the properties are assumed to be reflective of those in 0.5% Intralipid.

2
## Contrast for Photon Migration Imaging: Fluorescence Lifetime

2.1
Single Pixel Measurements for Photon Migration Imaging

To experimentally assess the feasibility of external contrast agents, the impact of absorbing and fluorescing heterogeneities on light propagation in a tissue simulating phantom was examined. The influence of lifetime on photon migration measurements was also investigated. Single pixel measurements of modulation phase, θ, and modulation ratio, M, were measured as a function of modulation frequency, ω, in the presence and absence of: (i) light-absorbing, and (ii) fluorescing objects.

Fig. 2.1. Schematic of the cylindrical tank used in the single pixel measurements of modulation phase and modulation ratio for absorbing and fluorescing heterogeneities

30.5 cm

6–11 mm

20 cm

Source

Detector
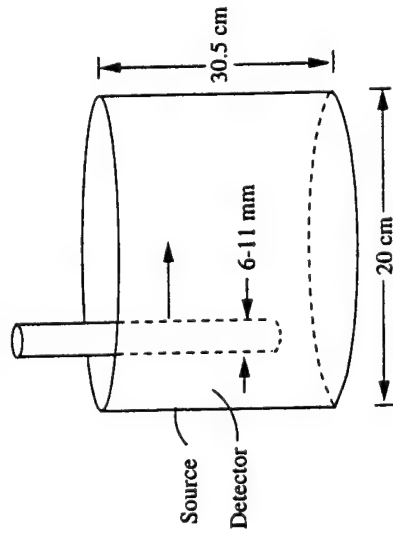
2.2
Phantom Apparatus

The tissue phantom, illustrated in Fig. 2.1, consisted of a Plexiglas cylindrical tank, 20 cm in diameter and 30.5 cm in height, filled with 8 l of 0.5% by volume Intralipid solution (Kabi Pharmacia, Clayton, NC). This concentration of Intralipid mimics the scattering properties of tissue ($\mu_s' \approx 10 \text{ cm}^{-1}$) [28]. Two small holes, an arc distance of 2.0 cm apart, were drilled half way up the side of the tank in order to couple the 1000 micron fiber optic (HCP-M1000T-08, Spectron Specialty Optics Co, Avon, CT) source and detector directly to the phantom. The fiber optics were placed approximately 1 mm inside the medium to avoid boundary effects caused by the wall of the tank. On the outside of the tank, silicon gel (Dow Corning Co., high vacuum grease, Midland, MI) was placed around the fibers to prevent leakage of Intralipid.

The perfect absorbing heterogeneity was a 6-mm diameter glass rod painted black. The fluorescent body consisted of a 9-mm inner diameter cylindrical glass container filled with micromolar solutions of either 3,3′-diethylthiatricar-bocyanine iodide (DTTCI) (ACROS Organics, Fairlawn, NJ), a common laser dye, or ICG (Sigma Chemical Company, St. Louis, MO) diluted in 0.5% Intralipid solution. Dilution in Intralipid maintained a scattering coefficient inside the heterogeneity identical to the surrounding medium. Measurements of θ and M were conducted as the heterogeneity was moved various distances away from the wall midpoint between the source and detector. The object position was measured from the leading edge of the heterogeneity where a position of zero denotes contact between the heterogeneity and the wall of the tank.

2.3
Frequency Domain Instrumentation and Setup

The light propagation at both the excitation and emission wavelengths was measured using frequency domain measurements. The measurements were conducted at modulation frequencies between 80 and 240 MHz using a pulsed

titanium/sapphire laser coupled to the detection system consisting of an ISS K2 phase fluorometer (ISS, Champaign, IL).

2.3.1
Heterodyne Detection Approach with Modulated Laser Source

To use simple electronics to detect the signal, a heterodyne technique was used. This detection method involves modulating the detectors at a frequency plus a small offset from the modulation frequency of the source. For example, the sinusoidal source is described by the expression:

$$A \cos(\omega t + \theta) \tag{2.1}$$

where A is the amplitude; ω is the modulation frequency; and θ is the phase of the source. The gain of the detector is modulated by $\omega + \Delta\omega$ so that the detector response is represented by:

$$\cos[(\omega + \Delta\omega)\, t] \tag{2.2}$$

where $\Delta\omega$ is the small offset frequency of the detector. The signal obtained by the detector is then:

$$A \cos(\omega t + \theta) \times \cos[(\omega + \Delta\omega)\, t] = \frac{A}{2}\cos(\Delta\omega t + \theta) +$$
$$+ \frac{A}{2}\cos[(2\omega + \Delta\omega)\, t + \theta] \tag{2.3}$$

A low pass filter is used to filter out frequencies above $\Delta\omega$, the signal received by the detector is:

$$\frac{A}{2}\cos(\Delta\omega t + \theta) \tag{2.4}$$

It is important to note that the phase and amplitude information of the high frequency signal is preserved.

2.3.2
Heterodyne Detection Approach with Pulsed Laser Source

When the light source is a mode locked pulsed laser, the signal can no longer be described by Eq. 2.1. Instead, the source is represented by:

$$\sum_{n=1}^{\infty} A_n \cos(n\omega t + \theta_n) \tag{2.5}$$

where the above equation is the frequency domain representation of a mode locked pulsed laser [29]. Again the detector is modulated at a frequen-

cy plus a small offset as described by Eq. 2.2, the signal obtained by the detector is:

$$\cos[(\omega + \Delta\omega) t] \times [A_1\cos(\omega t + \theta_1) + A_2\cos(2\omega t + \theta_2) + \ldots] =$$

$$+ \frac{A_1}{2} \{\cos(\Delta\omega t + \theta_1) + \cos[(2\omega + \Delta\omega) t + \theta_1]\}$$

$$+ \frac{A_2}{2} \{\cos[(\omega + \Delta\omega) t + \theta_2] + \cos[(3\omega + \Delta\omega) t + \theta_2]\} + \ldots \qquad (2.6)$$

Filtering out frequencies above $\Delta\omega$, the signal received by the detector is:

$$\frac{A_1}{2} \cos(\Delta\omega t + \theta_1) \qquad (2.7)$$

which is completely analogous to Eq. 2.4.

2.3.3
Instrumentation

The excitation light source consists of a titanium/sapphire laser pumped by a 10-W argon ion laser (Spectra Physics, CA), to produce a pulse train of 2 ps at a repetition rate of 80 MHz (Fig. 2.2). The output wavelength of the titanium/sapphire laser is set to 780 nm. To establish a phase lock with the detection equipment, an 80 MHz signal origination from the titanium/sapphire laser is sent to a divide-by-8 circuit resulting in a 10-MHz signal. This 10-MHz signal is sent to a frequency synthesizer (Model 2022D, Marconi, Allendale, NJ) which
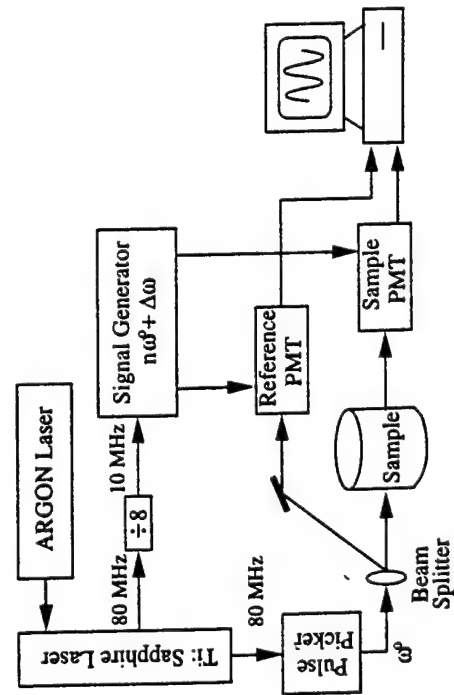

Fig. 2.2. Frequency domain system for single pixel measurements using a titanium/sapphire laser as the light source

controls the modulation of the detectors. The detectors are modulated at frequencies of 80, 160 and 240 MHz. The ligh from the laser has 1.3 W of average power.

The pulse train is focused onto a beam splitter. The unreflected portion of the pulse train (approximately 90% of the signal) serves as the light source and is focused onto a fiber optic coupled to the side of the cylindrical tank. The reflected portion of the signal is focused onto another fiber optic cable which delivers the signal to a reference photomultiplier tube (PMT). This light serves as the reference signal. The scattered excitation and emission light detected at the periphery of the phantom is delivered to a sample PMT also using a fiber optic cable. An 830-nm interference filter (10-830-4-1.00, CVI Laser Co, Albuquerque, NM) is placed in front of the sample PMT and is used to make frequency domain measurements at the emission wavelengths.

The gain of the PMTs is modulated at a harmonic of the source frequency but offset by 100 Hz in order to produce a heterodyne signal. The output from both PMTs is sent to an ISS board for data acquisition. The modulated phase and amplitude are extracted from the signal at the 100-Hz cross correlation frequency through simple electronics and software (ISS, Champaign, IL).

2.4
Contrast Due to Perfect Absorption and Perfect Uptake of Fluorescence

The modulation phase and modulation ratio were measured to evaluate the contrast offered by, (i) a perfect absorber, and (ii) a fluorescent volume in a lossless scattering medium (no absorption in the surrounding). Since the fluorescent object had perfect uptake of dye and since the absorber was a black rod, they represent the best possible contrast owing to absorption and fluorescence. For this experiment DTTCI served as the fluorescent contrast agent.

Measurements of modulation phase, θ, and modulation ratio, M, were conducted as the heterogeneities were moved from the peripheral location towards the center of the phantom. Figure 2.3 shows the phase contrast, $\Delta\theta$ ($\theta_{presence} - \theta_{absence}$), due to the presence of both an absorbing and a fluorescing heterogeneity at 80-, 160-, and 240-MHz modulation frequencies. The largest phase contrast is measured at 240 MHz and the signal is only altered by approximately 20° for absorption; however, for fluorescence, an alteration of approximately 60° is observed. Therefore, these results show that the best contrast available from absorption (i.e., a perfect absorber) causes a smaller measurable disturbance in photon migration than a micromolar concentration of fluorescent dye. In addition, the fluorescent signal is detected approximately 1 cm deeper than the absorbance signal.

Measurements of modulation ratio, M, for the perfect absorber and the fluorescent volume were not performed. However, a similar experiment conducted by Lopez [30] using a 9-mm diameter perfect absorbing fluorescent object shows that the modulation contrast ($M_{presence}/M_{absence}$) of the fluorescent object at 240 MHz is approximately 0.1 while the absorber only offers 0.6 contrast. These results are consistent with those that would be expected.
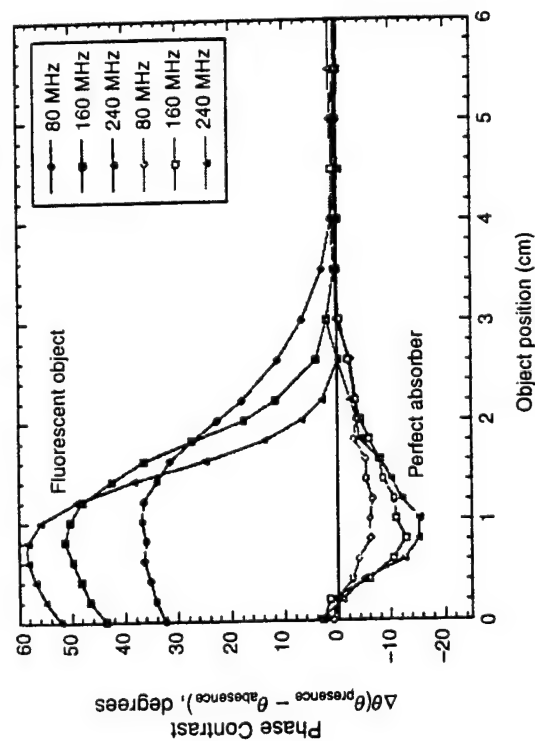
Fig. 2.3. Phase contrast, $\Delta\theta(\theta_{presence} - \theta_{absence})$, as a function of object position for both a perfect absorbing object (open symbols) and a fluorescent object (closed symbols) measured at 80, 160 and 240 MHz

In a realistic situation, the administration of contrast agents results in the imperfect uptake of dye into tissue regions of interest. Recently, Lopez et al. [4, 30] have conducted measurements of phase and modulation contrast with imperfect uptake ratios of 1:100 and 1:10 with a similar experimental apparatus as that described above. They found the resulting phase contrast to be dramatically smaller than the situation of perfect uptake. However, the magnitude of contrast offered by fluorescence phase contrast and modulation contrast still exceeds absorption contrast, which is in agreement with the above work. As discussed in Sect. 1, the additional time-delay associated with the lifetime of a fluorescent molecule during the emission process causes a greater phase and modulation contrast over that of absorption.

2.5 Contrast Due to the Influence of Lifetime

The next experiment assessed the influence of lifetime on contrast. In an analogous single pixel experiment to the one described above, Intralipid solutions with micromolar concentrations of DTTCI and ICG were investigated and compared with each other since DTTCI and ICG have different lifetimes of 1.18 and 0.56 ns, respectively [4].

Dilute non-scattering solutions of both DTTCI and ICG were separately analyzed in a small glass cuvette. Using the instrumentation discussed above, measurements of modulation phase and modulation ratio were conducted with
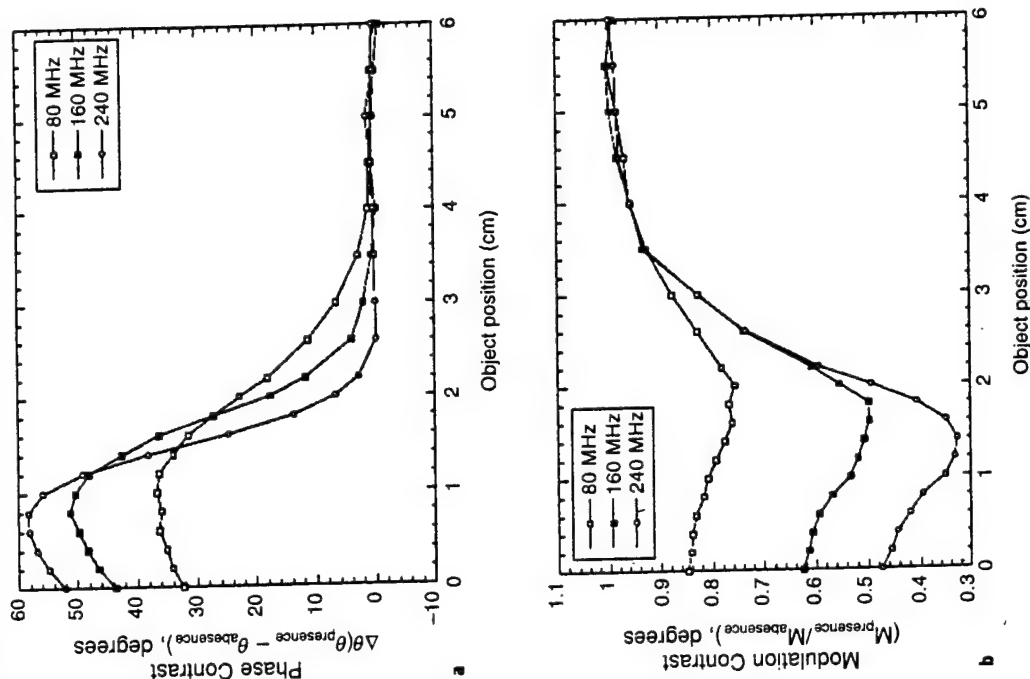
Fig. 2.4. Experimental measurements of **a** phase contrast, $\Delta\theta(\theta_{presence} - \theta_{absence})$, and **b** modulation contrast, ΔM ($M_{presence}/M_{absence}$) vs. object position for a micromolar solution of DTTCI at modulation frequencies of 80, 160 and 240 MHz. A 9.5-mm diameter heterogeneity was used to hold the dye solution inside the 20-cm diameter tank

the source at a right angle to the detector. Using a third dye, IR-140 (ACROS Organics, Fairlawn, NJ), as a standard, the lifetimes of DTTCI and ICG were obtained by evaluating the equations discussed in Sect. 1.6.2.1.

Both the modulation phase and modulation ratio were measured as a function of frequency as DTTCI and ICG scattering solutions were moved from

the periphery to the center of the phantom. Figures 2.4 and 2.5 illustrate the phase contrast for DTTCI and ICG, respectively. As the lifetime of the dye increases, the phase contrast should also increase and the modulation ratio should decrease (see Sect. 1). Since the lifetimes of DTTCI and ICG are 1.05 and 0.58 ns, respectively, the phase contrast for DTTCI should be larger and the modulation contrast should be smaller. This is indeed the case since DTTCI
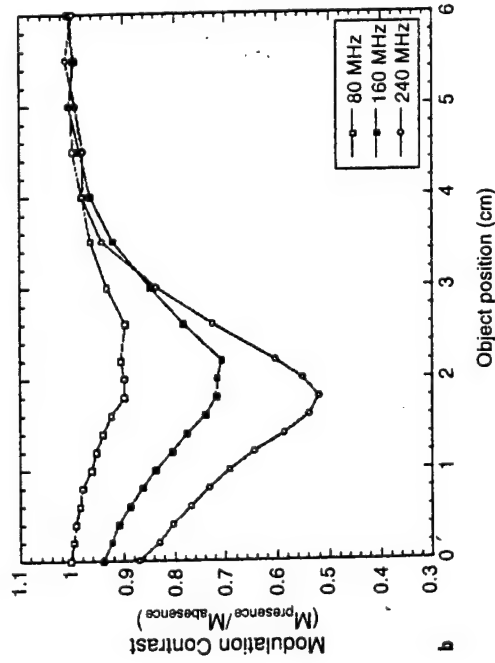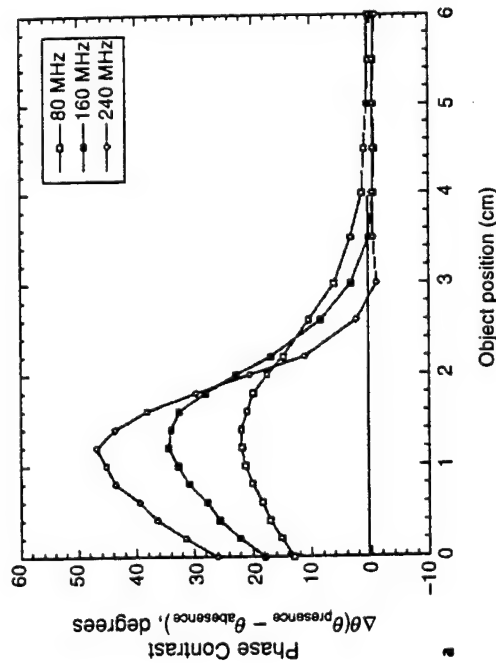

Fig. 2.5. Experimental measurements of a phase contrast, $\Delta\theta(\theta_{presence} - \theta_{absence})$, and **b** modulation contrast, ΔM ($M_{presence}/M_{absence}$) vs. object position for a micromolar solution of ICG at modulation frequencies of 80, 160 and 240 MHz. A 9.5-mm diameter heterogeneity was used to hold the dye solution inside the 20-cm diameter tank

exhibits values of $\Delta\theta = 60°$ and $\Delta M = 0.3$ and ICG shows values of $\Delta\theta = 46°$ and $\Delta M = 0.5$. These results confirm that frequency domain measurements contain information of fluorescent lifetime.

2.6 Discussion

The results in this section show that fluorescence offers improved contrast over absorption. Since measurements were conducted on a perfect absorber, the findings suggest that the endogenous contrast due to absorption from increased hemoglobin associated with angiogenesis may be too small for realistic measurements for optical tomography (Fig. 1.6). The second study shows that frequency domain measurements contain lifetime information which can provide diagnostic information about the local biochemical environment (see Eq. 1.16). However, these measurements need to be coupled to an inversion algorithm in order to extract the lifetime from the scattered signal (see Sect. 3 for more details). The single pixel measurements presented here show great promise for the detection of diseased tissues laden with contrast agents using photon migration measurements. But single pixel measurements only provide one dimensional information and therefore cannot be used to resolve an interior image of optical properties. To obtain enough information to locate a heterogeneity, measurements at multiple locations need to be obtained.

3 Reconstruction of Fluorescence Quantum Efficiency and Lifetime

3.1 Inverse Imaging Problem

Recently, we have developed multi-pixel measurements for rapid data acquisition of modulation phase and amplitude of re-emitted optical signals [31]. Using a gain-modulated image intensifier coupled to a CCD camera, acquisition of 128×128 measurements of modulation phase and amplitude has been possible in approximately 10 ms at excitation wavelengths and 1 s at emission wavelengths. In order to employ these measurements to reconstruct interior maps of lifetime and quantum efficiency from exterior frequency domain measurements made at the periphery, an inverse algorithm needs to be employed. Currently, two approaches for solving the inverse imaging problem have been demonstrated. Both approaches involve solutions to the diffusion equation where the first method uses perturbation expansions of the photon diffusion equation [32–35] and the second solves the diffusion equation directly using a finite difference or a finite element approach [36–40].

In this work, we employ the latter approach to reconstruct optical property maps of absorption, fluorescent quantum efficiency, and fluorescent lifetime of an optical heterogeneity without a priori information of position or volume. Specifically, the tissue volume of interest is mathematically represented by discretized volume elements in which the optical properties of absorption,

fluorescence quantum efficiency and lifetime are constructed. The inversion schemes incorporate an iterative Newton-Raphson technique to update values of the optical properties at every volume element in order to minimize the least-squares difference between the experimental and calculated detector responses at the periphery. The method is similar to that used by Yorkey et al. [41] for electrical impedance tomography, Pogue et al. [37] for absorption and scattering reconstructions, and Paithankar et al. [40] who performed reconstructions on both fluorescent lifetime, τ, and fluorescent yield (the product of the absorption coefficient due to fluorophores and quantum efficiency, $\phi\mu_{a_{xf}}$). In this section, interested readers will find the numerical technique used in solving the forward problem along with the approach to solving the inverse imaging problem. Finally, applications of the inversion to simulated data are presented in Sect. 4 illustrating the feasibility of fluorescent quantum efficiency and lifetime imaging in tissues and other scattering media. Section 3 may be ignored by those readers not interested in the mathematics of solving the forward and inverse imaging problems.

3.1.1
Forward Problem

The coupled diffusion equations for excitation and emission light propagation (Eqs. 1.17 and 1.18) are complex linear elliptic equations which can be analytically solved as boundary value problems when the optical properties are independent of spatial position. The complex fluence can be used to predict modulation phase and amplitude from the real and imaginary components. However, when there is a spatial variation in optical properties (such is the case when an optical heterogeneity is present) numerical solutions are necessary. In this work, the finite difference method was used to solve both the excitation fluence, $\Phi^x(\vec{r}, \omega)$, and the emission fluence, $\Phi^m(\vec{r}, \omega)$. The method of finite differences involves discretizing the area of interest into a grid and a linear system is obtained by approximating derivatives in the diffusion equation by differences.

In this study, a two-dimensional simulated tissue phantom, as shown in Fig. 3.1, was employed. The phantom is modeled as a $4 \times 4\,\mathrm{cm}^2$ square surface with a 17×17 grid representing the area of potentially differing optical properties. The source and the detector locations were placed one pixel in from the edge of the phantom to overcome the effects of the zero fluence boundary condition. A source is centered on each side of the phantom for a total of 4 sources. The grid contains 56 detectors per source evenly spaced around the phantom. The placement of the 56 detectors are source measurements. In all the simulated experiments, the sources are source represents an isotropic excitation source located 0.25 cm or 2.5 scattering lengths from the surface. Since all the experiments discussed here are performed using simulated data, the placement of the source will not affect the solution to the inversion. However, when this algorithm is coupled to experimental measurements, the placement of the source needs to be correctly represented.

For solutions of the forward problem, the known optical properties of the background and the object are input as parameters into the program and then the fluence at each grid point is calculated. The fluence values are used at the detector positions and the modulation phase, $\theta^{x,m}$, and the log of the modula-
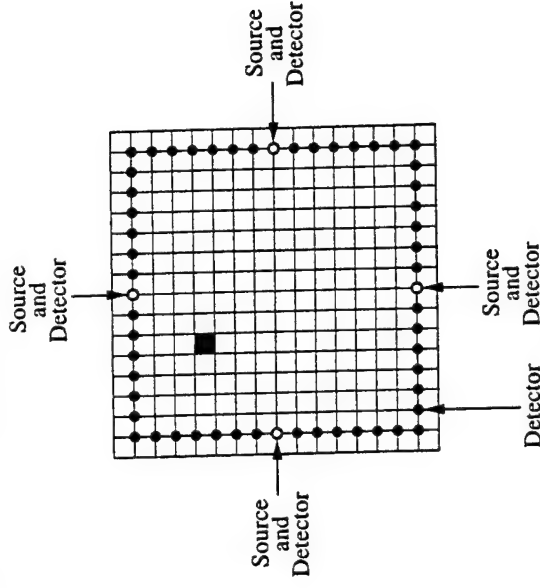
Fig. 3.1. Schematic of the two-dimensional simulated tissue phantom showing the location of the 4 sources and 56 detectors around the perimeter for the 17×17 mesh on a 16-cm² area. The small square object inside the phantom represents a simulated diseased tissue volume

tion amplitude, $I_{AC}^{x,m}$, are calculated from both the real and imaginary components of the excitation or emission fluence, $\Phi^{x,m}$, where:

$$\theta^{x,m} = \tan^{-1}\left[\frac{\mathrm{Im}\,\Phi^{x,m}}{\mathrm{Re}\,\Phi^{x,m}}\right] \times \frac{360}{2\pi} \qquad (3.1)$$

$$I_{AC}^{x,m} = \log_{10}\sqrt{[\mathrm{Im}\,\Phi^{x,m}]^2 + [\mathrm{Re}\,\Phi^{x,m}]^2} \qquad (3.2)$$

To run a single simulated experiment, only one source is active. For each forward solution, values of $\theta^{x,m}$ and $I_{AC}^{x,m}$ are calculated at all the detector positions. Once these detector values are obtained, the forward solution is repeated for the next source location. This procedure continues until all four sources have been investigated. A total of four simulated experiments constitute the data to be acquired experimentally. Consequently, the simulations will yield a total of 224 detector measurements. In all the simulated experiments, the sources are modulated at a frequency of 100 MHz. Typical forward calculations on a Ultra 2 Sun workstation took approximately 1.3 s.

After detector data have been evaluated for $\theta^{x,m}$ and $I_{AC}^{x,m}$ simulated Gaussian noise with standard deviations of 0.1° for phase and 1% for modulation amplitude are added using a MATLAB routine. The Gaussian noise is added to account for the noise which would be encountered in a real experiment. The simulated forward results with added noise are then input to the inversion algorithm.

3.1.2
Solution to the Inverse Problem

The solution to the inverse problem requires reconstructing images of the interior volume from exterior measurements of $\theta^{x,m}$ and $I_{AC}^{x,m}$. Since more information from exterior measurements enable better image reconstruction, more detectors and multiple modulation frequencies should improve image reconstructions. The inversion algorithm is conducted in two parts on the basis of, (i) absorption at the excitation wavelength due to fluorophores, $\mu_{a_{xf}}$, and (ii) quantum efficiency, ϕ, or lifetime, τ, at the emission wavelength. The two parts are similar except that the reconstruction based on $\mu_{a_{xf}}$ uses detector data at the excitation wavelength while the other part uses data at the emission wavelength.

Figure 3.2 depicts the flow diagram for these inversion algorithms. To begin the inverse calculation based on $\mu_{a_{xf}}$, an initial homogeneous guess for the
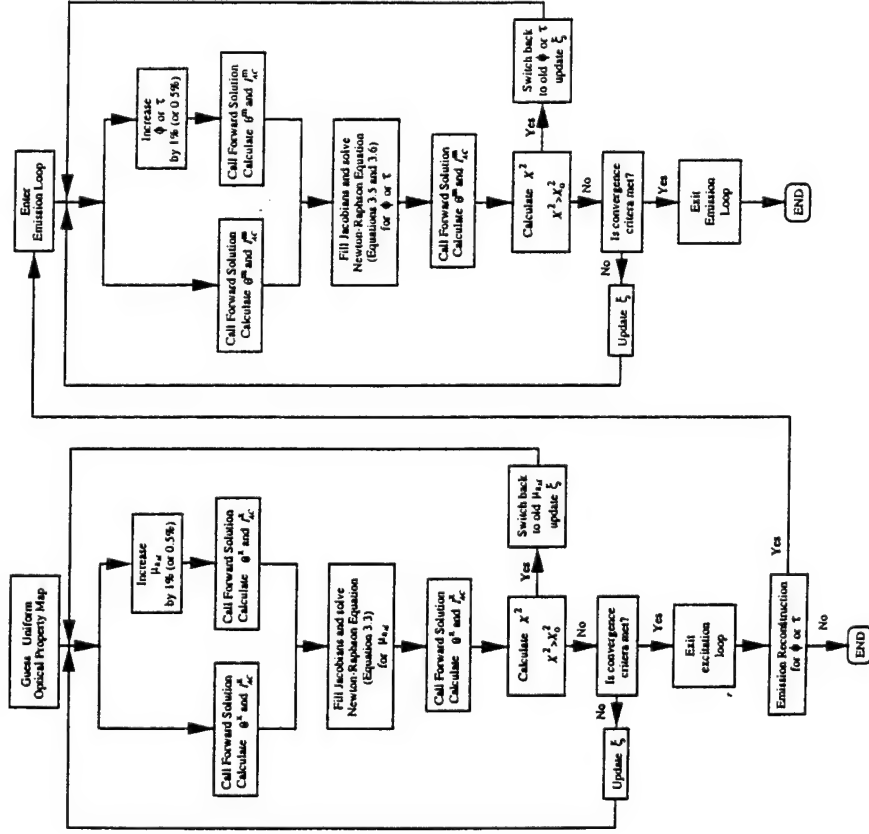
optical property map is given. Typical values are those found in normal tissues. From these values the forward solution is calculated to obtain θ^x and I^x_{AC} measurements at the detector positions for the excitation light. Next, two Jacobian matrices, $J(\theta^x, \mu_{a_{xf}})$ and $J(I^x_{AC}, \mu_{a_{xf}})$, are constructed where an entry of each matrix is defined as $j_{ij} = \partial\theta^x/\partial\mu_{a_{xf},i}$ and $j_{ij} = \partial I^x_{AC}/\partial\mu_{a_{xf},i}$, respectively. Each element of the matrix describes the response of the source-detector pair at position i to changes in $\mu_{a_{xf}}$ at each pixel. The partial derivatives are numerically approximated by calling the forward solution (Cud2) a second time for a 1% increase of the original pixel value or $\mu_{a_{xf}}$ and subtracting the difference (i.e. $\partial\theta^x/\partial\mu_{a_{xf}} \approx \Delta\theta^x/\Delta\mu_{a_{xf}}$ and $\partial I^x_{AC}/\partial\mu_{a_{xf}} \approx \Delta I^x_{AC}/\Delta\mu_{a_{xf}}$).

To update $\mu_{a_{xf}}$, an iterative Newton-Raphson technique involving the Jacobians was used:

$$\left[\frac{J^T(\theta^x, \mu_{a_{xf}})\, J(\theta^x, \mu_{a_{xf}})}{\sigma_\theta^2} + \frac{J^T(I^x_{AC}, \mu_{a_{xf}})\, J(I^x_{AC}, \mu_{a_{xf}})}{\sigma_{I_{AC}}^2} + \xi I \right] [\Delta\vec{\mu}_{a_{xf}}] =$$

$$= \left[\frac{J^T(\theta^x, \mu_{a_{xf}})}{\sigma_\theta^2}(\vec{\theta}_{obs} - \vec{\theta}_{cal}) + \frac{J^T(I^x_{AC}, \mu_{a_{xf}})}{\sigma_{I_{AC}}^2}(\vec{I}_{AC_{obs}} - \vec{I}_{AC_{cal}}) \right] \quad (3.3)$$

where $\Delta\vec{\mu}_{a_{xf}}$ provides an increment change for updating $\mu_{a_{xf}}$, and ξ is a regularization parameter multiplied by the identity matrix I. Because the Jacobian matrices are ill conditioned due to the small sensitivity of $\mu_{a_{xf}}$ far away from the source and detector, the regularization parameter compensates by making the matrices more diagonally dominant. The parameter ξ is then adjusted by a Marquardt-Levenberg algorithm at every iteration [37]. In order to solve the linear algebraic equations (Eq. 3.3) for $\Delta\vec{\mu}_{a_{xf}}$, a LU decomposition back substitution method is used. The updated optical property map is then found by adding $\Delta\vec{\mu}_{a_{xf}}$ to the values from the previous iteration.

The forward solution is re-calculated using the new updated values in order to determine the reconstruction error:

$$\chi_x^2 = \frac{1}{4nd} \sum_{k=1}^{4} \sum_{i=1}^{nd} \left[\left(\frac{\theta^x_{cal,i} - \theta^x_{obs,i}}{\sigma_\theta} \right)^2 + \left(\frac{I^x_{AC_{cal,i}} - I^x_{AC_{obs,i}}}{\sigma_{I_{AC}}} \right)^2 \right] \quad (3.4)$$

where nd is the total number of detectors (56); θ^x_{cal} and $I^x_{AC_{cal}}$ are the predicted detector data; and θ^x_{obs} and $I^x_{AC_{obs}}$ are the simulated experimental detector data for the excitation light. Again, σ_θ and $\sigma_{I_{AC}}$ are the typical standard deviations of noise in the measurements taken to be 0.1° and 1%, respectively. For comparison, our multi-pixel measurements have errors in the order of 0.2° and 1.8%. The values of σ_θ and $\sigma_{I_{AC}}$ are scale factors that describe the confidence in the measurement. Every node on the grid will yield an equation and the only known variables are at the detector positions. Since there are many more nodes than detectors, the inversion scheme is underconstrained and not guaranteed to converge on the actual optical property map.

The entire procedure of iteratively adjusting $\mu_{a_{xf}}$ to minimize the χ^2_x error continues until a predetermined convergence criterion is met. The criterion is

Fig. 3.2. Flow diagramm of the reconstruction algorithm. The excitation loop reconstructs $\mu_{a_{xf}}$ and the emission loop either reconstructs ϕ or τ

met if any of the following quantities: (i) the value of χ_x^2; (ii) the absolute change in χ_x^2, or (iii) the relative change in χ_x^2 becomes lower than 1.0×10^{-5} or a maximum of 50 iterations is reached. Typical times to complete the inverse solution are approximately 45 min on a Ultra 2 Sun workstation.

If only a map of μ_{a_xf} is desired, the program stops. Otherwise, the map of μ_{a_xf} is used in order to compute a second map of either ϕ or τ. Currently, the computation of the maps of ϕ and τ are conducted in two separate programs in order to evaluate their individual performances.

After the loop in which the map μ_{a_xf} is calculated, the forward solution is now calculated to obtain θ^m and I_{AC}^m measurements at the detector positions for the emission light using the homogeneous map described above except with the updated values of μ_{a_xf}. Next, two Jacobian matrices are constructed: $J(\theta^m, \phi)$ and $J(I_{AC}^m, \phi)$ for the reconstruction of ϕ, or $J(\theta^m, \tau)$ and $J(I_{AC}^m, \tau)$ for the reconstruction of τ. Each element of these Jacobian matrices is defined as $j_{ij} = \partial\theta_i^m/\partial\phi_j$, $j_{ij} = \partial I_{AC_i}^m/\partial\phi_j$, $j_{ij} = \partial\theta_i^m/\partial\tau_j$, and $j_{ij} = \partial I_{AC_i}^m/\partial\tau_j$, respectively. Again, each element of the Jacobian matrix describes the response of the source-detector pair at position i to changes in ϕ or τ at each pixel j. The partial derivatives are approximated as described above where $\partial\theta^m/\partial\phi \approx \Delta\theta^m/\Delta\phi$, $\partial I_{AC}^m/\partial\phi \approx \Delta I_{AC}^m/\Delta\phi$, $\partial\theta^m/\partial\tau \approx \Delta\theta^m/\Delta\tau$, and $\partial I_{AC}^m/\partial\tau \approx \Delta I_{AC}^m/\Delta\tau$.

Equations 3.5 and 3.6 provide updates of ϕ and τ by adding $\Delta\vec{\phi}$ and $\Delta\vec{\tau}$, respectively, to the values of ϕ and τ from the previous iteration:

$$\left[\frac{J^T(\theta^m,\phi)\, J(\theta^m,\phi)}{\sigma_\theta^2} + \frac{J^T(I_{AC}^m,\phi)\, J(I_{AC}^m,\phi)}{\sigma_{I_{AC}}^2} + \varsigma I \right] [\Delta\vec{\phi}] =$$
$$= \left[\frac{J^T(\theta^m,\phi)}{\sigma_\theta^2}\, (\theta_{obs}^m - \theta_{cal}^m) + \frac{J^T(I_{AC}^m,\phi)}{\sigma_{I_{AC}}^2}\, (\bar{I}_{AC_{obs}}^m - \bar{I}_{AC_{cal}}^m) \right]$$

(3.5)

and

$$\left[\frac{J^T(\theta^m,\tau)\, J(\theta^m,\tau)}{\sigma_\theta^2} + \frac{J^T(I_{AC}^m,\tau)\, J(I_{AC}^m,\tau)}{\sigma_{I_{AC}}^2} + \varsigma I \right] [\Delta\vec{\tau}] =$$
$$= \left[\frac{J^T(\theta^m,\tau)}{\sigma_\theta^2}\, (\theta_{obs}^m - \theta_{cal}^m) + \frac{J^T(I_{AC}^m,\tau)}{\sigma_{I_{AC}}^2}\, (\bar{I}_{AC_{obs}}^m - \bar{I}_{AC_{cal}}^m) \right]$$

(3.6)

Again, the forward solution is re-calculated using the updated values in order to determine the reconstruction error:

$$\chi_m^2 = \frac{1}{4\,nd} \sum_{k=1}^{4} \sum_{i=1}^{nd} \left[\left(\frac{\theta_{cal,i}^m - \theta_{obs,i}^m}{\sigma_\theta} \right)^2 + \left(\frac{I_{AC_{cal,i}}^m - I_{AC_{obs,i}}^m}{\sigma_{I_{AC}}} \right)^2 \right]$$

(3.7)

where θ_{cal}^m, $I_{AC_{cal}}^m$ are the predicted detector data and θ_{obs}^m and $I_{AC_{obs}}^m$ are the simulated experimental detector data for the emission light. The values for σ_θ and $\sigma_{I_{AC}}$ are the same as in the absorption reconstruction, 0.1° and 1.0%, respectively. The entire procedure of iteratively adjusting ϕ or τ to minimize the χ_m^2 error continues until the same convergence criterion as above is met or 50 iterations have passed.

4
Reconstruction of Absorption and Fluorescence Quantum Efficiency and Lifetime in a Scattering Medium

4.1
Results for the Reconstruction Algorithm

Three different types of simulations were separately performed. They included reconstructions on the basis of either absorption, μ_{a_x}, quantum efficiency, ϕ, or lifetime, τ. In all three classes of simulated experiments, an optical heterogeneity was 0.063 cm² which constituted 0.39% of the total area. During the reconstructions of both ϕ and τ unphysically high optical property values around the periphery and especially near the source locations were obtained. These values were replaced with the average background value with a constraint statement inside the program.

For all the reconstructions, values of μ_{a_xf} ranged from 0.010 to 0.200 cm⁻¹. These values of absorption correspond to an ICG concentration of approximately 0.076 to 1.53 µM [4]. These ICG concentrations are well below lethal levels and are approximately 5 to 60 times lower than the therapeutic concentrations currently administered with many photodynamic agents [42, 43].

4.2
Reconstruction of the Absorption Coefficient from Excitation Light

This section describes the simulations performed on the basis of absorption due to fluorophores, μ_{a_xf}, at the excitation wavelength. Figure 4.1 illustrates both simulated and reconstructed data as an optical tissue heterogeneity is moved diagonally towards the detectors at three different object locations. The heterogeneity contains 20-fold more absorbing dye than its surroundings (see Table 4.1). The experiment shows that the heterogeneity location is successfully reconstructed. However, since the program preserves the average pixel value, a smoothing of the reconstructed image is observed causing the magnitude of μ_{a_xf} for both the object and the surroundings to be incorrect as shown in Table 4.1. As the object moves closer to the detectors, less error in the reconstruction

Table 4.1. Optical Properties and Experimental Parameters Used as Inputs for the Forward Problem Along with Values of μ_{a_xf} Obtained from the Reconstructions for Three Different Object Locations

Case	Actual				Reconstructed		
	Background		Object		Background	Object	
	μ_{a_xi}, μ_{a_xf} (cm⁻¹)	μ_{s_x} (cm⁻¹)	μ_{a_xf} (cm⁻¹)	Position	μ_{a_xf} (cm⁻¹)	μ_{a_xf} (cm⁻¹)	Position
a	0.010	10.0	0.200	(11,7)	0.011	0.034	(11,7)
b	0.010	10.0	0.200	(13,5)	0.011	0.042	(13,5)
c	0.010	10.0	0.200	(15,3)	0.011	0.068	(15,3)

Fig. 4.1. Reconstructed spatial maps of an absorbing heterogeneity as a function of position for a 20:1 uptake ratio of dye inside the object. Figures a, b and c are actual spatial maps and Figures d, e and f are their corresponding reconstructions. The actual values of $\mu_{a_{xf}}$ in the object and the surroundings are 0.200 cm^{-1} and 0.010 cm^{-1}, respectively

is obtained since, the value of $\mu_{a_{xf}}$ inside the object increases while the value in the background decreases. In fact, the value of $\mu_{a_{xf}}$ at the closest object position is 0.068 cm^{-1} (case c) is twice the value of the farthest position (0.034 cm^{-1}, case a). This reduction of error is expected since there is more signal yielding a larger disturbance to be measured at the detectors. In other words, a heterogeneity present close to the source and detector will have more influence on the inversion problem since the pixels closer to the source and detectors have more

influence on the measured signal making the solution better defined. Successful reconstructions have also been performed for a more realistic uptake of 10:1 as well as higher resolutions (33 × 33 grid) [44].

4.3
Reconstruction of Quantum Efficiency from Emission Light

The performance of the inverse algorithm for reconstructing maps of quantum efficiency, φ, using detector data at the emission wavelength is discussed in this section. For all the inversions discussed here, the exact value of $\mu_{a_{xf}}$ inside the object was input into the initial homogeneous guess. This procedure causes the inversion algorithm to converge after one iteration in the excitation loop and the exact value of $\mu_{a_{xf}}$ to be used in the emission loop in order to only investigate the reconstruction on φ. Table 4.2 lists all the optical properties and experimental parameters used in the forward solutions to generate the simulated detector data and compares the values from the forward solution to those obtained by the inversion solution.

Figure 4.2 shows a the actual solution, b the reconstruction, and c the value of φ inside the object as a function of iteration number. The experiment ended
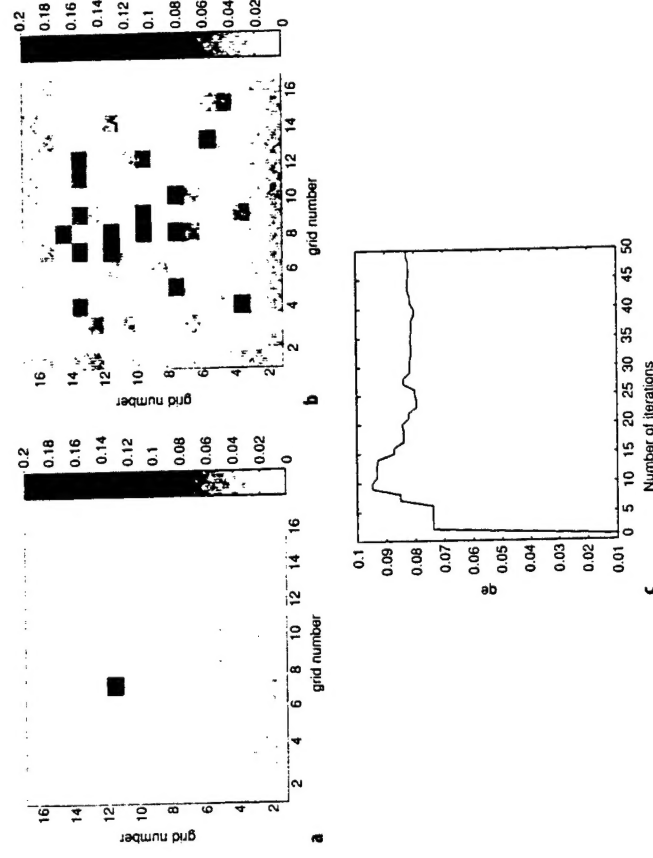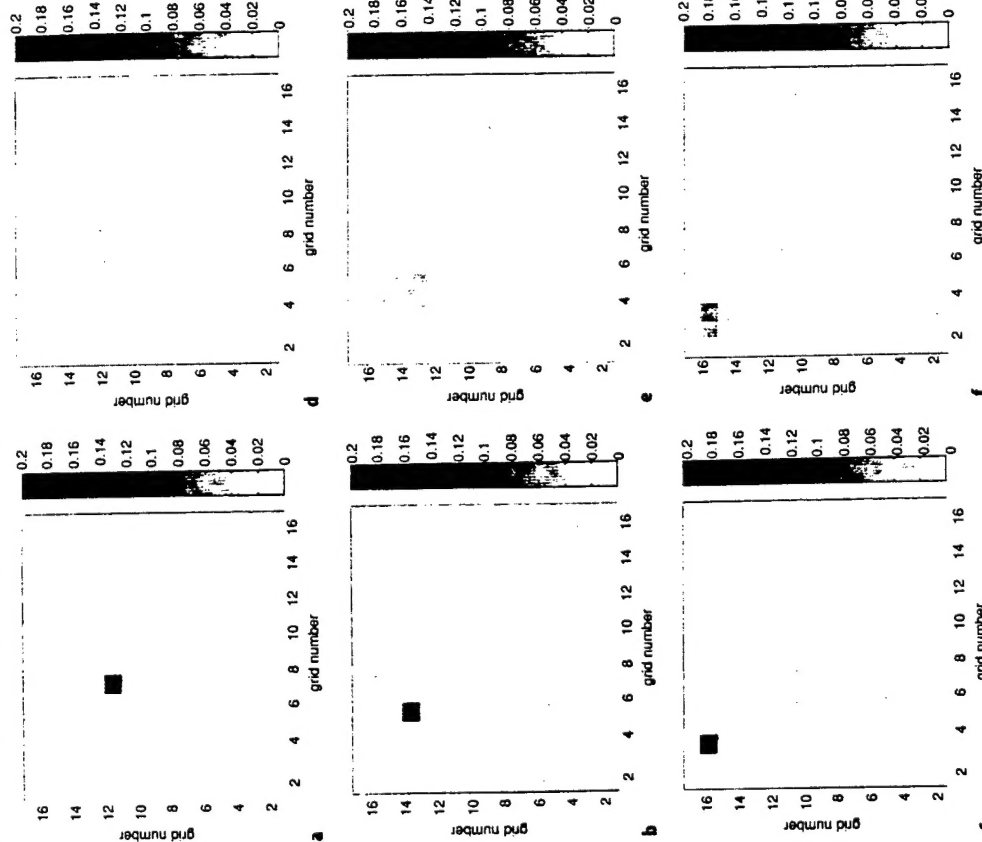

Fig. 4.2. Reconstructed spatial maps of fluorescent quantum efficiency, φ, for 10:1 uptake of dye inside the heterogeneity. Figure a represents the actual image, b shows the corresponding reconstruction and c shows the value of φ inside the object as a function of iteration number. The actual values of φ in the object and the surroundings were 0.100 cm^{-1} and 0.010 cm^{-1}, respectively, and the reconstructions yielded values of 0.082 cm^{-1} and 0.012 cm^{-1}, respectively

Table 4.2. Optical Properties and Experimental Parameters Used as Inputs for the Forward Problem Along with Values of φ Obtained from the Reconstructions

									Reconstructed	
	Actual									
	Background						Object		Background	Object
$\mu_{a_i},\mu_{a_{mi}}$ (cm^{-1})	$\mu_{a_{xf}}$ (cm^{-1})	μ_{s_i},μ_{s_m} (cm^{-1})	$\mu_{a_{mi}}$ (cm^{-1})	τ (ns)	ϕ	$\mu_{a_{xf}}$ (cm^{-1})	τ (ns)	ϕ	ϕ	ϕ
0.000	0.020	10.0	0.002	1.00	0.010	0.200		0.100	0.012	0.082

after 50 iterations without meeting any of the convergence criteria. The optical property map of the reconstruction shows that the location of the object is successfully located but that the value of ϕ inside the object only reaches 0.082 (18% smaller than the actual value of 0.100). Also, the background pixel values are noisy with an average value of 0.012 which is 20% larger than the actual value of 0.010.
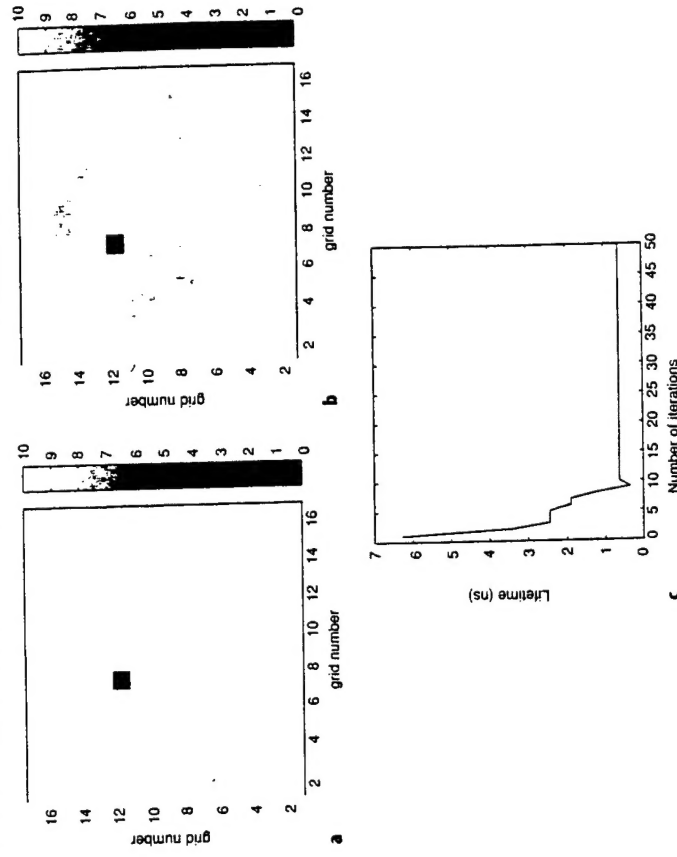
4.4
Reconstruction of Lifetime from Emission Light

The performance of the inversion algorithm for reconstructing lifetime, τ, using detector data at the emission wavelength is discussed in this section. Similar to the reconstructions of ϕ, all the inversions in this section use the exact value of $\mu_{a_{xf}}$ inside both the object and background for the initial optical property map. This procedure causes the inversion algorithm to converge after one iteration in the excitation loop and the exact value of $\mu_{a_{xf}}$ to be used in the emission loop to investigate the reconstruction of τ only.

The lifetime reconstruction for a 10:1 uptake of dye, the current uptake ratio for available contrast agents, was investigated. Table 4.3 lists all the optical properties and experimental parameters used in the forward solution to generate the detector data and compares the values from the forward solution to those obtained by the inverse solution. This particular simulation had an arbitrary lifetime value of 1.00 ns inside the object and 10.0 ns everywhere else. Figure 4.3

Table 4.3. Optical Properties and Experimental Parameters Used as Inputs for the Forward Problem Along with Values of Lifetime Obtained from the Reconstructions

									Reconstructed	
	Actual									
	Background						Object		Background	Object
μ_{a_i},μ_{a_m} (cm^{-1})	$\mu_{a_{xf}}$ (cm^{-1})	μ_{s_x},μ_{s_m} (cm^{-1})	$\mu_{a_{mi}}$ (cm^{-1})	ϕ	τ (ns)	$\mu_{a_{xf}}$ (cm^{-1})	ϕ	τ (ns)	τ (ns)	τ (ns)
0.000	0.020	10.0	0.002	0.034	10.0	0.200	0.100	10.0	10.1	0.996

Fig. 4.3 panels: (a) actual spatial map (grid number vs grid number), (b) reconstructed spatial map (grid number vs grid number), (c) Lifetime (ns) vs Number of iterations.

Fig. 4.3. Reconstructed spatial maps of fluorescent lifetime, τ, for 10:1 uptake of dye inside the heterogeneity. Figure a represents the actual image, b shows the corresponding reconstruction and c depicts the convergence of τ in the object as a function of iteration number. The actual lifetimes for the object and background are 1 and 10 ns, respectively. The reconstruction converges correctly to 1 ns in the object. The background converges to 10.067 ns which is 0.67% larger than the actual value of 10 ns

shows a the actual spatial map, b the reconstructed spatial map, and c the average value of τ as a function of the iteration number inside the object. Because τ inside the object is lower than in the background, the object location is defined as the pixel with the lowest value of τ. Both the location and magnitude of τ inside the object are correctly found since the reconstructed value for pixel (11,7) is 0.996 ns, only 0.04% lower than the actual value. The reconstruction for the background gives a good convergence of 10.1 ns even though the background contains a small amount of noise which is symmetric about the object. This noise is most likely an artifact from the large fluence that emerges from the four source locations.

4.5
Discussion

Numerical simulations were conducted in order to examine the resolution and accuracy of the reconstruction method. These results show the potential of

photon migration for the optical detection of a heterogeneity inside a scattering medium. The simulated experiments based on $\mu_{a,i}$ can locate an absorbing heterogeneity inside a tissue-simulating phantom; however, the magnitude of $\mu_{a,i}$ inside the heterogeneity is smaller than the actual solution. The simulated experiments also show the ability to reconstruct the interior optical property maps for both quantum efficiency and lifetime using detector information at the emission wavelength. Reconstructing maps of lifetime not only provides object location but also may provide information regarding the environment (see Sect. 1.16 for discussion on the Stern-Volmer equation). This information about the local biochemistry can help to differentiate normal from diseased tissue.

To couple these inversion algorithms with experimental measurements, all the optical coefficients of the background need to be scaled by a factor of $(3/2)^{1/2}$ to account for the two-dimensional nature of the algorithm and the three-dimensional nature of the experiment [45]. The noise for the fluorescent measurements needs to be determined since it is unlikely to be the same as the excitation data (0.1° for θ^x and 1% for I_{AC}). Also, both inversions assume that the noise is uniform over the entire region which may not be the actual situation, and updates to the inversion scheme, which take the noise as a function of position into account, need to be implemented.

To further improve the reconstructions, detector information at multiple modulation frequency needs to be incorporated into the algorithm. Multiple frequency information will provide more detector information helping with the underconstrained nature of the inversion problem.

4.6 Conclusion

Absorption and fluorescent methods of inducing contrast were examined using single pixel measurements. The results in this study show that fluorescence has improved contrast over absorption due to the additional mechanism from the kinetics of the fluorescence decay process. It has also been demonstrated that lifetime differences alter the propagation of the detected signal. Since targeted delivery of a contrast agent may not always be feasible, lifetime sensitive dyes which are specific to different environmental conditions found in normal and diseased tissue may enhance detection.

References

1. Mordon S, Devoisselle JM, Maunoury V (1994) In vivo pH measurements and imaging of tumor tissue using pH sensitive fluorescent probe (5,6-carboxyfluorescein): instrumental and experimental studies. Photochem Photobiol 60:274–279
2. Russell DA, Pottier RH, Valenzeno DP (1994) Continuous noninvasive measurement of in vivo pH in conscious mice. Photochem Photobiol 59:309–313

3. Vinogradov SA, Lo LW, Jenkins WT, Evans SM, Koch C, Wilson DF (1996) Noninvasive imaging of the distribution in oxygen in tissue in vivo using near-infrared phosphors. Biophys 70:1609–1617
4. Sevick-Muraca E, Lopez G, Reynolds J, Troy T, Hutchinson C (1997) Fluorescence and absorption contrast mechanisms for biomedical optical imaging using frequency-domain techniques. J Photochem Photobiol 66:55–64
5. Cubeddu R, Canti G, Taroni P,Valentini G (1993) Time-gated fluorescence imaging for the diagnosis of tumors in murine model. Photochemistry and Photobiology 57:480–485
6. Cubeddu R, Canti G, Pifferi A, Taroni P, Valentini G (1997) Fluorescence lifetime imaging of experimental tumors in hematoporphyrin derivative sensitized mice. Photochemistry and Photobiology 66:229–236
7. Lim HW, Soter NA (1993) Clinical Photomedicine, Marcel Dekker, New York
8. Haskell RC, Svaasand LO, Tsay TT, Feng T, McAdams MS, Tromberg BJ (1994) Boundary conditions for the diffusion equation in radiative transfer. J Opt Soc Am A 11:2727–2741
9. Beauvoit B, Evans SM, Jenkins TW, Miller EE, Chance B (1995) Correlation between the light scattering and the mitochondrial content of normal tissues and transplantable rodent tumors. Analytical Biochemistry 226:167–174
10. Chance B, Liu H, Kitai T, Zhang Y (1995) Effects of solutions on optical properties of biological materials: models, cells and tissues. Analytical Biochemistry 227:351–362
11. Flock ST, Wilson BC, Patterson MS (1988) Hybrid Monte Carlo diffusion theory modeling of light distribution in tissue. Proc SPIE 908:20–28
12. Peters VG, Wyman DR, Patterson MS, Frank GL (1990) Optical properties of normal and diseased human breast tissues in the visible and near infrared. Phys Med Biol 35:1317–1334
13. Duderstadt JJ, Hamilton LJ (1976) Nuclear Reactor Analysis, Wiley, New York
14. Chandrasekhar S (1958) Radiative Transfer, Dover, New York
15. Ishimaru A (1973) Wave propagation and scattering in random media. Academic Press, New York, Vol. 1
16. Patterson MS, Chance B, Wilson B (1989) Time resolved reflectance and transmittance for the noninvasive measurement of tissue optical properties. Appl Opt 28:2331–2336
17. Reynolds J, Przadka A, Yeung S, Webb K (1996) Optical diffusion imaging: a comparative numerical and experimental study. Appl Opt 35:3671–3679
18. O'Leary M, Boas D, Chance B, Yodh A (1992) Refraction of diffuse photon density waves. Physical Review Letters 69:2658–2661
19. Lakowicz J (1983) Principles of Fluorescence Spectroscopy. Plenum Press, New York
20. Sevick EM, Burch CL (1994) Origin of phosphorescence signals reemitted from tissues. Opt Lett 19:1928–1930
21. Sevick-Muraca EM, Hutchinson C (1995) Probability description of fluorescent and phosphorescent signal generation in tissues and other random media. SPIE 2387: 274–283 (1995)
22. Batchteler G, Drexhage KH, Arden-Jacob J, Han KT, Kollner M, Muller R, Sauer M, Seeger S, Wolfrum J (1994) Sensitive fluorescence using laser diodes and multiplex dyes. J Luminescence 60:511–514
23. Patterson MS, Pogue BW (1994) Mathematical model for time-resolved and frequency-domain fluorescence spectroscopy in biological tissues. Appl Opt 33:1963–1974
24. Hutchinson CL, Lakowicz JR, Sevick-Muraca EM (1995) Fluorescence life-time based sensing in tissues: A computational study. Biophys J 68:1574–1582
25. Wilson BC, Patterson MS (1986) The physics of photodynamic therapy. Phys Med Biol 31: 327–360
26. Lee WW, Wilson D, Singerman L (1994) Correction of spatial distortion and registration in ophthalmic fluorescein angiography. IEEE 16:508–509
27. May SA (1994) Photonic approaches to burn diagnostics. Biophotonics International, pp 44–50
28. van Staveren HJ, Moes CJM, van Marle J, Prahl SA, van Gemert MJC (1991) Light scattering in Intralipid-10% in the wavelength range of 400–1100 nm. Appl Opt 30:4507–4514

Single-Molecule Detection in Biology with Multiplex Dyes and Pulsed Semiconductor Lasers

M. Sauer, J. Wolfrum

1
Single-Molecule Detection with Far-Field Fluorescence Microscopy Techniques

In recent times, researchers have made considerable efforts to achieve the detection of individual atoms and molecules in solids [1–6], on surfaces [7–10], and in liquids [11–20] using laser-induced fluorescence techniques. In particular, single-molecule detection in condensed phases has many important biological applications, including rapid DNA sequencing, medical diagnosis, and forensic analysis [21–23]. For the detection of single dye molecules it is essential to minimize the background from scattering and luminescent impurities in the solvent, i.e. the ability to detect fluorescence bursts emitted by individual dye molecules is not as much an issue of sensitive detection as it is of background reduction. The predominant source of background is Rayleigh scattering, as well as reflected light, which can be efficiently suppressed by suited optical filters. Since Raman scattering is directly proportional to the detection volume, this background signal can be greatly reduced if a confocal setup in combination with a detection volume of only a few femto liters or even less is employed [24–27]. The detection volume is usually defined by the intersection of the focused excitation laser and the image of a spatial filter. The reduction of the detection volume improves the signal-to-background ratio by many orders of magnitude without measurable photodestruction of the dye molecules under study. Poisson statistics predicts, for a concentration of less than 10^{-10} M, that the number of molecules fluctuates predominantly between 0 and 1 in an applied detection volume in the femto liter region. Hence, the probability of two or more molecules being present in the detection volume simultaneously is negligible at concentrations below 10^{-10} M. On the other hand, a small detection volume reduces the transition time, i.e. the measurement time. During the transition through the detection volume, the dye molecule is excited by the laser light from the ground state S_0 into high-lying vibrational levels of the first excited state S_1, which undergoes rapid nonradiative internal conversion to low-lying S_1 levels. The optical saturation limit is the maximum rate that a dye molecule can be cycled between S_0 and S_1, and is dependent on the fluorescence lifetime of the dye τ_f. Besides irreversible photodestruction several depopulation pathways such as intersystem crossing into the triplet state compete with the fluorescence emission thus reducing the number of emitted photons. Since

29. Yariv A (1985) Introduction to Optical Electronics, 3rd ed, Holt-Saunders International Editions, New York

30. Lopez G (1997) Absorption and fluorescent contrast mechanisms for the detection and diagnosis of breast cancer using single pixel frequency-domain photon migration techniques. Masters thesis, Purdue University, West Lafayette, IN

31. Reynolds JS, Troy T, Sevick-Muraca EM (1997) Multi-pixel techniques for frequency-domain photon migration imaging. Biotechnology Progress 13:669–680

32. O'Leary M, Boas D, Chance B, Yodh A (1994) Reradiation and imaging of diffuse photon density waves using fluorescent inhomogeneities. J Lumin 60 & 61:281–286

33. Boas DA, O'Leary MA, Chance B, Yodh AG (1994) Scattering of diffuse photon density waves by spherical inhomogeneities with turbid media: analytic solution and applications. Proc Natl Acad Sci USA 91:4887–91

34. O'Leary M, Boas D, Chance B, Yodh A (1995) Experimental images of heterogeneous turbid media by frequency-domain diffusion-photon tomography. Optics Letters 20:426–428

35. Yao Y, Wang Y, Pei Y, Zhu W, Barbour RL (1997) Frequency-domain optical imaging of absorption and scattering distributions by a Born iterative method. J Opt Soc Am A 14:325–342

36. Arridge SR, Schweiger M, Hiraoka M, Delpy DT (1993) Performance of an iterative reconstruction algorithm for near infrared absorption and scatter imaging. SPIE 1888:360–371

37. Pogue BW, Patterson MS, Jiang H, Paulsen KD (1995) Initial assessment of a simple system for frequency domain diffuse optical tomography. Phys Med Biol 40:1709–1729

38. Jiang H, Paulsen KD, Osterberg UL, Pogue BW, Patterson MS (1995) Simultaneous reconstruction of absorption and scattering maps in turbid media from near-infrared frequency-domain data. Opt Lett 20:2128–2130

39. Jiang H, Paulsen KD, Osterberg UL, Pogue BW, Patterson MS (1996) Optical image reconstruction using frequency domain data: simulations and experiments. J Opt Soc Am A 13:253–266

40. Paithankar DY, Chen AU, Pogue BW, Patterson MS, Sevick-Muraca EM (1997) Imaging of fluorescent yield and lifetime from multiply scattered light reemitted from random media. Appl Opt 36:2260–2272

41. Yorkey TJ, Webster JG, Tompkins WJ (1987) Comparing reconstruction algorithms for electrical impedance tomography. IEEE Trans Biomed Eng BME-34:843–852

42. Photodynamic Therapy: Basic Principles and Clinical Application, BW Henderson and TJ Dougherty, Eds, Marcel Dekker, Inc 1992

43. Marcus SL (1992) Photodynamic Therapy of Human Cancer. IEEE 80:869–889

44. Troy TL (1997) Biomedical Optical Imaging with Frequency Domain Photon Migration Measurements: Experiments and Numerical Image Reconstructions. PhD. Thesis, Purdue University, West Lafayette, IN, 1997

45. Burch CL (1993) Monte Carlo simulations of photon migration in highly scattering media. Masters Thesis, Vanderbilt University, Nashville, TN